Galaxy Evolution in a z∼3 Protocluster

Author:
Nancy Hine

Supervised by:
Dr James Geach

Centre for Astrophysics Research
School of Physics, Astronomy and Mathematics
University of Hertfordshire

Submitted to the University of Hertfordshire in partial fulfilment of the requirements of the degree of Doctor of Philosophy.

May 2017

Abstract

Environment is known to have a significant impact on the evolution of galaxies. This is most evident in the local Universe, where the oldest and most massive galaxies are found at the centre of massive galaxy clusters. Current theory predicts that galaxies will form earlier and evolve more rapidly in the densest regions of the Universe. What is not clear is how rapidly the affects of environment start to have an impact on galaxies, at what stage can we detect physical differences between galaxies in dense regions and those in the field? By the time galaxies are assembled in virialised clusters the effects are clear, but at higher redshift ($z \gtrsim 2$), in the unvirialised progenitors of clusters (protoclusters) the effects are harder to detect.

In this thesis I study the impact of environment in a $z = 3.1$ protocluster in the SSA22 field. I first consider the fraction of mergers in the protocluster, comparing it to the fraction of mergers in the field at a similar redshift. My classification is based on the morphology of Lyman break galaxies (LBGs), using HST ACS/$F814W$ imaging, which probes the rest frame UV. I find a marginal enhancement of the merger fraction, 48 ± 10 per cent for LBGs in the protocluster compared to 30 ± 6 per cent in the field, suggesting that galaxy-galaxy mergers are one of the key channels driving accelerated star formation and AGN growth in protocluster environments.

Having considered the fraction of mergers in the protocluster I then turn my attention to the physical properties of LBGs. I use multiwavelength data and spectral energy distribution fitting to determine the mass of LBGs in the protocluster and in the field. I find no statistical evidence for an enhancement of mass in the protocluster, suggesting that the protocluster environment has not impacted the average mass of LBGs at this redshift. It is possible that the protocluster LBG population may become more massive than LBGs in the field at lower redshift, or the galaxies may cease to be detectable by the Lyman break method before a mass difference between the protocluster galaxies and field is observable.

Finally I consider the Lyman-α blobs (LABs) within the protocluster. These are large ($\sim$10-100kpc) scale regions of diffuse Lyman-α emission, thought to be associated with overdense regions. 35 LABs have been detected in the SSA22 protocluster, indicating the presence of large clouds of gas in the circumgalactic medium. A debate has arisen regarding the powering mechanism of the LABs, particularly between star forming processes (e.g. Lyman-α escaping from a star forming galaxy or photoionizing radiation escaping from a star forming galaxy or active galactic nuclei) and a cold accretion model. The latter involves gas gravitationally cooling as it falls into the centre of a dark matter halo to feed a central galaxy. Some of this energy heats the cold gas, which then emits Lyman-α as it cools. The cold gas accretion theory gained

popularity because some LABs appear not to contain a luminous galaxy or AGN which could explain the observed emission. One suggestion is that the central galaxy could be hidden by dust and that this could explain the lack of a detection in UV or optical. I therefore use SCUBA2 850μm imaging to search for submm sources (dusty star forming galaxies) in the LABs. I detect submm sources in only two of the LABs at 3.5σ, however, stacking all the LABs gives an average flux density of $S_{850} = 0.6 \pm 0.2$mJy. This suggests that on average the LABs do contain a submm source which could be a dusty galaxy. However, stacking the LABs by size indicates that only the largest third (area $\gtrsim 1800$ kpc^2) have a mean detection, at 4.5σ, with $S_{850} = 1.4 \pm 0.3$mJy, suggesting that different mechanisms may dominate the larger and smaller LAB populations. I explore two possible mechanisms for powering the LABs, cold accretion and central star forming galaxies. I find that central star formation is more likely to be the dominant source of emission, with cold accretion playing a secondary role.

Declaration

I declare that no part of this work is being submitted concurrently for another award of the University or any other awarding body or institution. This thesis contains a substantial body of work that has not previously been submitted successfully for an award of the University or any other awarding body or institution.

The following parts of this submission have been published previously and/or undertaken as part of a previous degree or research programme:

1. Chapter 2: 'An enhanced merger fraction within the galaxy population of the SSA22 protocluster at $z = 3.1$', this has been published as Hine et al., 2016, *Monthly Notices of the Royal Astronomical Society*, **460**, 4075.

2. Chapter 4: 'The average submillimetre properties of Lyman-α Blobs at $z = 3$', this has been published as Hine et al., 2016, *Monthly Notices of the Royal Astronomical Society*, **455**, 2363.b

The text of these papers has been modified to better fit with the rest of the thesis.

Except where indicated otherwise in the submission, the submission is my own work and has not previously been submitted successfully for any award.

Acknowledgements

My journey into astronomy has taken many twists and turns, from my initial false start at an astrophysics degree back in 1986, through a completely different career or two, before getting back on track with the Open University and finally progressing to a PhD at the University of Hertfordshire. There are many people who have helped and encouraged me along the way and I take this opportunity to thank a few of them.

Firstly I would like to thank my principle supervisor Jim Geach for his invaluable guidance, without which I would never have achieved as much as I have during my PhD. He has encouraged me to publish papers, write many proposals, get involved in collaborations and generally take full advantage of my time as a student. I particularly thank him for giving me the opportunity to observe at Mauna Kea in Hawaii, not once, but six times during the last three years. An amazing place that I would never otherwise have visited. I would also like to thank my other PhD supervisors Kristen Coppin and Jason Stevens for their help and encouragement. A big thank you goes to my Masters supervisor Dan Smith, who, having got me through my Masters, has continued to give me encouragement during my PhD. Also thank you to Maciej Koprowski for his help with CIGALE; Derek McLeod for helping me to tame TPHOT and everyone in the Hertfordshire Extragalactic Group for helpful feedback.

I give a special thank you to Neil Cook who has been my Python guru throughout my time at Hertfordshire as well as providing the invaluable support of a good friend. Also a particular thank you to my current office mates Emma Lofthouse, Giulio Vestialbuio and Jonathan Westcott for the countless whiteboarding sessions that have helped me to make sense of astronomy. I also want to mention all those who've been involved with the infamous Horsa Gardens parties, including Geert Barentsen, Neil Cook, Julie Djordjevic, Hywel Farnhill, Chris Haynes, Ged Kitchener, Federico Marocco, Carla Natario, Gulay Gurkan Uygun, Nick Wright and all the friends I've made here, who have helped to make student life so enjoyable, Pete Beck, Ryan Cheale, John Collins, Tim Davis, Gaius Manser, Vijay Mahatma, Gareth Martin, Beatriz Mingo, Maria Monguio, Shaun Read, Leigh Smith, Mike Smith, Joanna Ramasawmy, Graham Thompson, and Wendy Williams. Also a thank you to all those I've worked with at Bayfordbury Observatory, for the many fun filled evenings at the telescope domes, in particular Mark Galloway, David Campbell, Lord Dover, Jess Schonhut-Stasik, Jess Martin-Smith and Dewi Wingar.

My biggest thank you must go to my family who have supported me throughout my journey, long before I actually arrived at Hertfordshire. To my parents Liz and Tony Hine for their endless support and patience as I changed subjects at University, changed careers more than once and generally ploughed my unpredictable course. Finally I owe a massive debt to my husband Alex Hocking, without whose emotional and practical support I could not have pursued my dream.

Contents

List of Figures

List of Tables

Chapter 1

Introduction

1.1 Galaxies over cosmic time

Understanding how galaxies formed and evolved over cosmic time is one of the key questions in astrophysics today. Galaxies in our local Universe were originally classified into two main types based on their morphology, spirals and ellipticals, although there was also a smaller population of galaxies with irregular morphology (Hubble, 1926). It was later discovered that the spirals were star forming galaxies and the ellipticals non star forming, or quiescent galaxies (e.g. Roberts, 1963; Kennicutt, 1998). However, improvements in technology (both telescopes and the instruments used to obtain images and spectroscopy) have expanded our view of the Universe to include increasingly distant galaxies and an ever expanding diversity of colour, size and morphology. With observations providing an increasingly complex picture of the Universe theorists have produced simulations with the aim of providing a framework to make sense of what we see. Such simulations (e.g. Springel et al., 2005; Keres et al., 2005; Croton et al., 2006; Baugh, 2006) provide us with a generally accepted overview of galaxy formation and evolution based on a hierarchical model and the Λ cold dark matter cosmology (ΛCDM, see Section 1.1.1), in which primordial density fluctuations grow through the gravitational attraction of collisionless cold dark matter and baryons to form the large scale structure of the Universe (Peebles, 1982).

1.1.1 The Universe before the first galaxies

The most widely accepted model of the Universe is based on the ΛCDM cosmology. According to this scenario, in addition to the baryonic matter and radiation with which we are all familiar, there exists cold dark matter (CDM, making up $\sim$85% of all matter) and dark energy. CDM is described as cold because it moves slowly compared to the speed of light, in contrast to the alternative scenario of hot dark matter which is fast (Primack and Blumenthal, 1984). CDM

does not scatter or emit electromagnetic radiation, making it impossible to detect directly with telescopes, but its gravitational effects on baryonic matter can be observed. Λ refers to dark energy, which is thought to be responsible for the accelerating expansion of the Universe. This is required to explain observations, but we do not yet know what it is or how to detect it directly. The ΛCDM model allows much of the history and large scale structure of the Universe to be described using a small number of parameters. The European Space Agency's recent Planck survey provides the most up to date parameter values (Planck Collaboration et al., 2016b).

The very early Universe is not well understood, but the currently favoured model includes an inflationary period $10^{-36}-10^{-32}$s after the Big Bang, when the Universe expanded by a factor of at least 10^{26} (e.g. Liddle and Lyth, 1993). Inflation smoothed out most of the matter in the Universe, leaving it largely homogeneous and isotropic, however it also effectively 'froze in' tiny quantum fluctuations. This pattern of large scale smoothness, with tiny density perturbations can be seen in the cosmic microwave background (CMB, explained below).

A few minutes after the Big Bang the Universe had cooled to the extent that atomic nuclei could start to form, protons and neutrons combining to produce deuterium, which then underwent further reactions to form Helium-4. After about 20 minutes all the neutrons in the Universe had been incorporated into Helium ions, fixing the mix of Hydrogen and Helium in the Universe at 3:1 by mass (with only trace amounts of heavier elements). At this time the Universe was still too hot for neutral atoms to form and the photons, electrons and baryons coexisted as a plasma. The mean free path that a photon travelled within the plasma before encountering an electron was so short that the plasma was effectively opaque to electromagnetic radiation. The tiny density perturbations left over from inflation gravitationally attracted the surrounding matter, but because the baryonic matter was coupled to photons this resulted in an outward pressure, working against gravitational collapse. The inward and outward pressures resulted in oscillations in the fluid, which can be seen as baryon acoustic oscillations (BAO) in the CMB (e.g. Peebles and Yu, 1970; Anderson et al., 2012). However, cold dark matter only interacts via gravity and without the outward pressure of radiation it was able to collapse onto the density perturbations and start to form a complex network of dark matter halos (DMHs). Eventually the dark matter would form a network of filaments and nodes throughout the Universe .

The Universe continued to expand and cool until about 370,000 years after the Big Bang when it reached a temperature of 3000-4000K and neutral atoms began to form (e.g. Peebles, 1968). This is referred to as recombination for historic reasons, although the particles had not previously been combined. The mean free path of photons now increased as there were fewer free electrons and eventually the photons decoupled from matter and were free to travel across the Universe. These photons are detected today as the CMB (first detected Dicke et al., 1965; Penzias and Wilson, 1965), which is effectively the redshifted black body radiation from when the Universe was $\sim$3000K (e.g. Planck Collaboration et al., 2016a). It was at this point that the oscillations in

the photon-baryon fluid became imprinted on the CMB as BAOs. Without the outward pressure from radiation the baryonic matter was now free to collapse under gravity. Eventually hydrogen gas would become concentrated into dense clouds from which the first stars would form.

1.1.2 How we see the distant Universe

Before moving on to consider the formation of galaxies we need to understand how the light from distant galaxies is effected by its journey across the Universe. As light travels towards us from distant galaxies the ongoing expansion of the Universe increases its wavelength as space-time itself is effectively stretched. This is called cosmological redshift and it is in addition to any redshift due to the local motion of galaxies caused by gravitational effects (peculiar velocities). When referring to objects in the distant Universe we express distance in terms of cosmic redshift, z, which we define by reference to a scale factor R(t), which describes the expansion of the Universe. R(t) is time dependent because the rate of expansion of the Universe varies over time.

$$1+z=\frac{R_0}{R_1} \tag{1.1}$$

R_0 is the scale factor of the Universe today and R_1 is the scale factor of the Universe when the observed light was emitted. z can also be expressed in terms of wavelength (λ):

$$1+z=\frac{\lambda_{observed}}{\lambda_{emitted}} \tag{1.2}$$

Because the light from distant objects travels at a given speed in a vacuum, z is also an indication of the time that the light has taken to reach us. For example, if a galaxy is at $z \sim 3$ we are seeing the light that left the galaxy approximately 12 billion years ago and the wavelength of the light we observe will be four times the length of the emitted wavelength. I will discuss further in section 1.4 how redshift impacts the techniques used to observe distant galaxies.

1.1.3 Galaxy formation and the role of gas

The first galaxies are thought to have formed through the accretion of gas onto dark matter filaments and nodes in the early Universe (e.g. White and Rees, 1978; White and Frenk, 1991; Katz and Gunn, 1991). The largest density peaks in the cosmic web accumulated gas most rapidly, forming galaxies more efficiently than other regions (e.g. Gunn and Gott, 1972; White et al., 1987; White and Frenk, 1991). Early theories predicted that gas would be shock heated to the virial temperature as it fell into DMHs and would then condense to form a central galaxy (e.g. White and Rees, 1978; White and Frenk, 1991; Katz and Gunn, 1991). This assumes that

galaxies are stable, self gravitating, virialised systems (in which the kinetic energy of the system is equal to minus half the gravitational potential energy of the system). Such a system will have an average temperature, T, as shown below.

$$\frac{1}{4}\frac{GM}{R} = \frac{1}{2}v^2 = \frac{3}{2}\frac{k_B T}{m_p} \tag{1.3}$$

Here symbols represent the virial mass, M, virial radius, R, virial velocity, v and virial temperature T. Constants are the gravitational constant, G, the Boltzmann constant, k_B, and the proton mass, m_p.

Later simulations suggest that in high mass DMHs (2-3$\times10^{11}$M$_\odot$ (Keres et al., 2009), 10^{12}M$_\odot$ (Dekel and Birnboim, 2006)), cold ($\sim10^{4-5}$K), pristine gas can penetrate the virialised halo to feed a central galaxy at high redshift ($z>2$), but the cold gas streams do not survive to reach the central galaxy at low redshift (Katz et al., 2003; Dekel and Birnboim, 2006; Keres et al., 2009; Nelson et al., 2015). The gas in low mass DMHs is not shock heated to the virial temperature until it reaches the galactic disc (Dekel and Birnboim, 2006) and so cold streams feed the galaxy at all redshifts.

Changes in the nature of cold gas flows from multiple, small, irregular flows at high redshift to a single flow feeding each galaxy at a low redshift may explain the formation of the Hubble sequence (Cen, 2014a). In this scenario the high redshift multiple flows create clumpy high redshift star forming galaxies and single flows at low redshift create the grand design spirals of the Hubble Sequence. Passive ellipticals at low redshift exist where there are no remaining cold flows.

1.1.4 Mergers

In addition to growing through the accretion of gas galaxies grow via mergers in accordance with the hierarchical model (e.g. White and Frenk, 1991; Conselice, 2007, 2014; Lotz et al., 2008). Mergers naturally lead to more massive galaxies simply by combining existing stellar mass. However, the gravitational disruption caused by mergers can also trigger new star formation and lead to starbursts (see section 1.1.5). By convention mergers with a mass ratio <4:1 are often referred to as major mergers and those with mass ratios between 4:1 and 10:1 as minor mergers (e.g. Kaviraj et al., 2015; Man et al., 2016), although other, similar, ratios are also used.

The impact of major mergers on star formation and morphology in individual galaxies, especially in low redshift irregulars, can clearly be seen (e.g. M82, The Antennae galaxies) . However, there is still debate as to the importance of mergers in contributing to the total stellar mass

of the Universe, especially at high redshift. Historically mergers had been thought to be responsible for triggering significantly enhanced star formation, morphological transformation (from spirals to ellipticals and the creation of bulges) and the growth of supermassive black holes (e.g. Springel et al., 2005; De Lucia et al., 2006; Avila-Reese et al., 2014). However, recent studies have found that mergers do not make a significant contribution to the overall star formation budget at $z > 1$, which is instead dominated by gas accretion (Dekel et al., 2009; Conselice et al., 2013; Rodighiero et al., 2011; Kaviraj et al., 2015; Lofthouse et al., 2017). Huertas-Company et al. (2015) also suggest that the growth of bulges may be largely due to secular processes rather than mergers. By contrast, in the local Universe, minor mergers are an important driver of star formation, accounting for half of all star formation in the Universe (Kaviraj, 2014). This difference in impact is related to the variation in average SFRs at different redshifts, discussed in the next section.

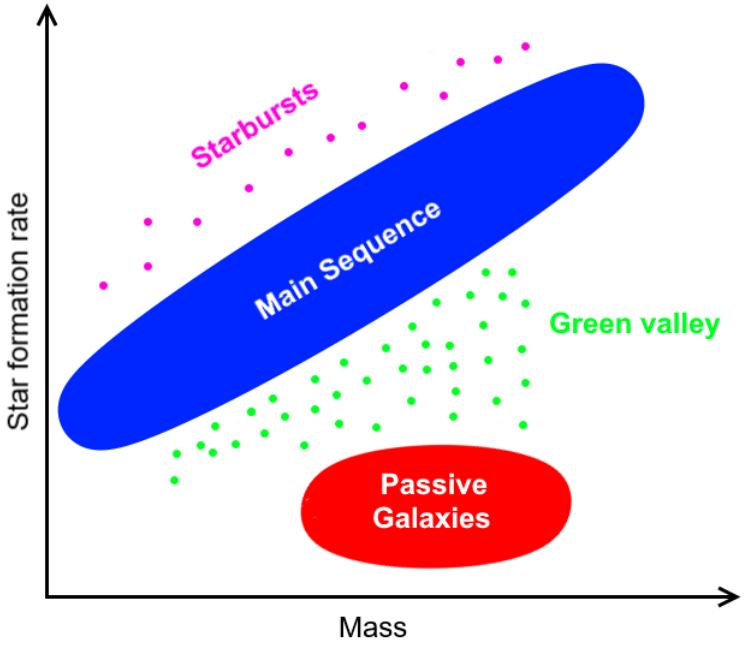

FIGURE 1.1: Cartoon of SFR against stellar mass indicating the position of the main sequence and passive galaxies. Starbursting galaxies and the green valley are also indicated.

1.1.5 Star Formation

Star forming galaxies at all redshifts show a fairly constant relationship between stellar mass and SFR, forming the so called, galaxy main sequence as SFR increases with stellar mass (see Fig. 1.1, e.g. Strateva et al., 2001; Baldry et al., 2004; Brinchmann et al., 2004; Daddi et al., 2007; Noeske et al., 2007). A small number of galaxies at all redshifts have a SFR above this relationship and are referred to as starbursting. These enhanced SFRs are short-lived and represent

a phase in galaxy evolution rather than a different type of galaxy (e.g. Karl et al., 2010). Most starbursts were originally thought to be the result of galaxy mergers or interactions (e.g. Sanders and Mirabel, 1996; Hopkins et al., 2006; Cox et al., 2008; Karl et al., 2010; Renaud et al., 2014). However, it has also been suggested that starbursts can be caused by secular processes, such as disk instabilities (e.g. Kennicutt, 1998; Kormendy and Kennicutt, 2004; Romeo and Fathi, 2016; Hinojosa-Goñi et al., 2016). Despite the high SFRs of starbursts, most of the stellar mass in the Universe is thought to be the result of main sequence star formation rather than starbursts (e.g. Rodighiero et al., 2011; Sargent et al., 2012).

Fig. 1.1 also highlights a second concentration of galaxies, which lies below the main sequence at lower SFRs and becomes increasingly important at low redshift. This region consists of galaxies with very low SFRs and it includes the giant ellipticals found in massive clusters ($> 10^{14}\mathrm{M}_{\odot}$) today. These have been the focus of much study, both because they include the most massive galaxies in the Universe ($> 10^{11}\mathrm{M}_{\odot}$) and because they contain most of the stellar mass in the local Universe (e.g. De Lucia et al., 2006). At $z = 0$ they have negligible star formation and are made up mostly of old stars, but they are thought to have evolved from progenitor star forming galaxies that formed most of their stars at $z > 3$ (De Lucia et al., 2006; Cen, 2014b).

A smaller population of galaxies lie between the main sequence and passive galaxies with intermediate SFRs, this is sometimes referred to as the green valley (Baldry et al., 2004; Martin et al., 2007; Gonçalves et al., 2012). There has been much speculation as to the nature of these galaxies, which may be in transition between the main sequence and passives. It has been suggested that these galaxies are in the process of being quenched via a number of mechanisms which impact their transition time. These include major mergers, active galactic nuclei (AGN) and supernovae (fast), minor mergers and interactions (intermediate) and secular evolution (slow) (Martin et al., 2007; Salim et al., 2007; Gonçalves et al., 2012; Cimatti et al., 2013; Schawinski et al., 2014; Smethurst et al., 2015). However, there is still much debate about the relative importance of these mechanisms.

The ($z > 3$) progenitors of the elliptical galaxies grew through the birth of new stars and mergers and at the same time the super massive black holes at their centre also grew through accretion, producing AGN (e.g. Gebhardt et al., 2000; Ferrarese and Merritt, 2000; Marconi and Hunt, 2003; Croton et al., 2006; McConnell and Ma, 2013; Madau and Dickinson, 2014). These AGN are thought to have caused quenching by heating and ejecting gas from galaxies, although supernovae may also have played a key role (e.g. White and Frenk, 1991; Croton et al., 2006; Dekel and Birnboim, 2006; Madau and Dickinson, 2014; Nelson et al., 2015). AGN feedback is considered to be particularly important in massive galaxies at low redshift, where a large force is required to expel material from the deep gravitational well (Benson, 2010; Dekel and Birnboim, 2006; Keres et al., 2009). Supernova feedback is considered to be the dominant process in less massive galaxies at all redshifts and in higher mass galaxies at high redshift, which are more

compact than their low redshift counterparts (Benson, 2010; Dekel and Birnboim, 2006; Keres et al., 2009). Smethurst et al. (2015) suggest that the fast processes were more common at high redshift and galaxies now mostly pass through the green valley at intermediate speeds (i.e. via minor mergers and interactions).

Quenching is also caused by environmental factors. Gas in the intra-cluster medium (ICM) of low redshift clusters is gravitationally shock heated as infalling flows of pristine cold gas collide. Some galaxies falling into cluster halos will undergo ram pressure stripping in these hot gas environments, which removes their reservoir of cold gas and quenches star formation in all but the inner few kiloparsecs (Gunn and Gott, 1972; Quilis et al., 2000; Cen, 2014c). The gas in the inner part of the galaxy will be used up on scales of 100s Myr. The hot ICM provides an inefficient environment for gas to cool, thus the galaxy is starved of the raw materials to form new stars (Larson et al., 1980; Cen, 2014c). Gas may also be removed via tidal processes, sometimes referred to as 'strangulation' (Larson et al., 1980).

Some galaxies in the green valley appear to be moving in the opposite direction, from the passive region towards the main sequence, as their SFR increases (e.g. Thilker et al., 2010). It is possible that galaxies may move back and forward between the two sequences several times before becoming completely quenched, or linger for long periods within the valley. Massive galaxies may have passed through multiple stages of AGN activity and quiescence as gas was blown out of galaxies and then re-accreted (baryon recycling). Whatever the quenching process may be, eventually, the massive progenitors of the local ellipticals became largely quiescent and continued to grow only though minor and dry mergers (van Dokkum, 2005; Bell et al., 2006; Kaviraj et al., 2009; Kaviraj, 2014).

To better compare the SFR of galaxies of different masses at different redshifts we use the specific star formation rate (sSFR $\equiv$ SFR/stellar mass). The cosmic sSFR of star forming galaxies has been found to increase steeply between $0 < z < 2$ and then more gradually to $z = 7$ (see Fig. 1.2, González et al., 2014; Madau and Dickinson, 2014). This indicates that the sSFR of main sequence galaxies was higher at high redshift, thus the progenitors of giant ellipticals are likely to have had high SFRs. Passive galaxies have sSFR below those of the main sequence star forming galaxies. There is no single definition of a passive galaxy and, the passive sSFR will vary with redshift, however a typical value used in the literature is sSFR $\leq 10^{-11}\mathrm{yr}^{-1}$ (Cassata et al., 2011; Tamburri et al., 2014). The average sSFR of main sequence galaxies declines gradually with mass (e.g. Karim et al., 2011), indicating that the most massive galaxies, such as the giant ellipticals, built their stellar mass at earlier times than lower mass galaxies (Brinchmann and Ellis, 2000; Juneau et al., 2005). Such a scenario is described as downsizing and was first proposed by Cowie et al. (1996).

Fig. 1.2 indicates that SFRs in individual galaxies (of a given mass) were highest in the early Universe, but the number of galaxies was also increasing in the early Universe, so when did

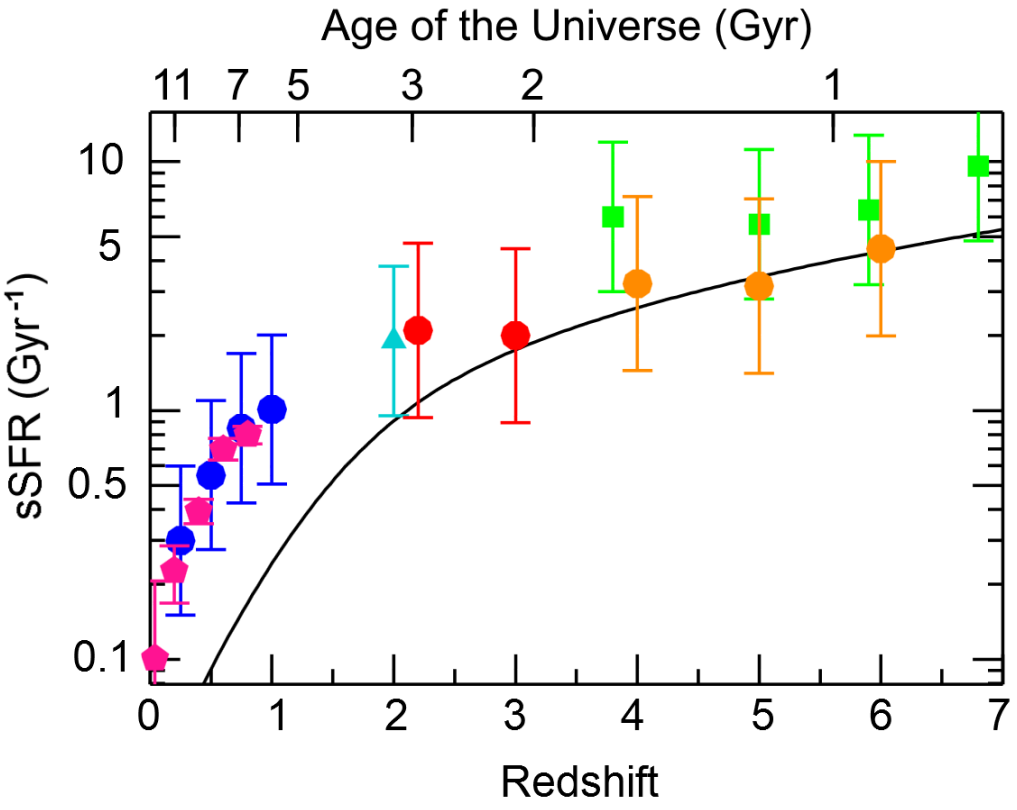

FIGURE 1.2: Mean sSFR (galaxies with estimated masses $10^{9.4}$ - 10^{10}M$\odot$) against redshift from Madau and Dickinson (2014) showing an increase in sSFR with increasing redshift. Data points are from Daddi et al. (2007) (cyan triangle), Noeske et al. (2007) (blue dots), Damen et al. (2009) (magenta pentagons), Reddy and Steidel (2009) (red dots), Stark et al. (2013) (green squares), González et al. (2014) (orange dots). The curve indicates the predicted trend from the Madau and Dickinson (2014) best fit star formation history, which includes passive galaxies.

the bulk of stars form? Fig. 1.3 shows the cosmic star formation rate density (SFRD) increasing steadily from $8 < z < 3$, before slowing and peaking at $3 < z < 2$ then declining again to $z = 0$ (Barger et al., 1998; Madau et al., 1998; Daddi et al., 2005; Madau and Dickinson, 2014; Bouwens et al., 2016). The peak represents an era of maximum star formation when most of the stellar mass in the Universe was generated. This peak shifts towards lower redshift if bright IR sources are included, suggesting that the bulk of stellar mass may have been produced at a slightly lower redshift than was previously thought, i.e. $1 < z < 2.5$. The SFRD continues to decline beyond $z = 8$, but photometry beyond this point is less reliable (see the large error bars in Fig. 1.2) and so the slope less constrained (Bouwens et al., 2016).

1.1.6 Simulating the Universe

Attempts have been made to model the evolution of large scale structure and individual galaxies using computer simulations. N-body simulations model the changing distribution of dark matter under gravity, from earliest times to the current day structure of filaments and nodes, as

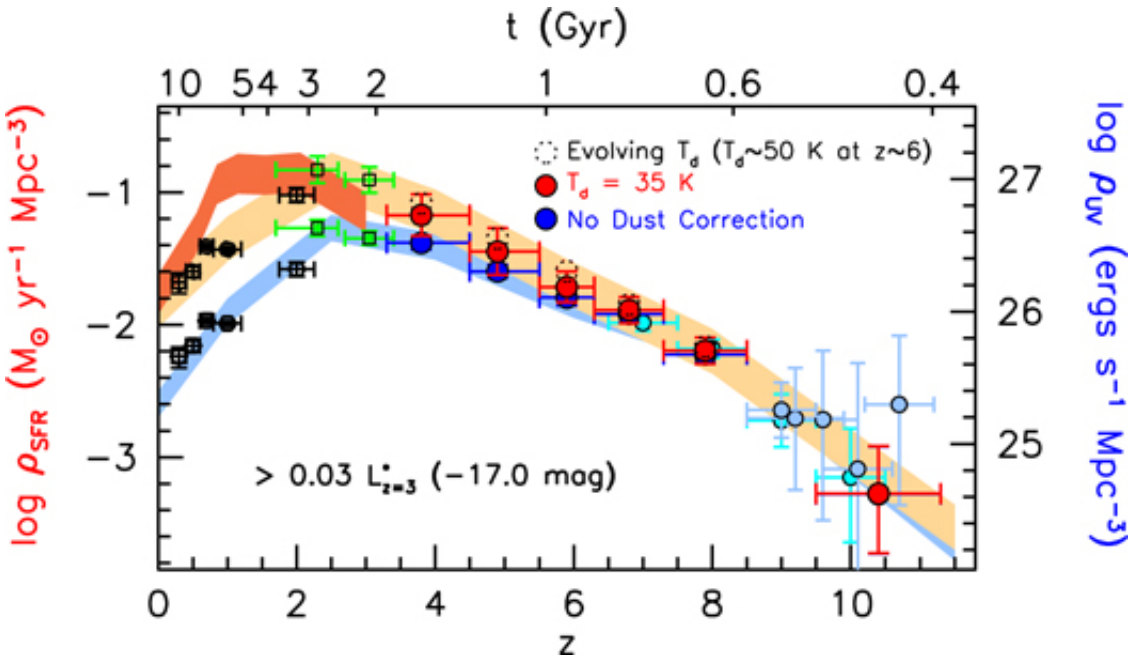

FIGURE 1.3: SFRD plot from Bouwens et al. (2016), with SFRD on the left axis and UV luminosity density on the right. Time is expressed in redshift on the bottom axis and Gyr on the top axis. The light orange and blue shaded regions indicate the SFRD with and without adjustments for dust extinction. Also shown are observations from Bouwens et al. (2016), [red circles (dust corrected, assuming a dust temperature of 35K), blue circles (no dust correction) and open dotted circles (dust corrected using a model that assumes dust temperature increases monotonically to high redshift)], plus observations from earlier work indicated as green crosses (Reddy and Steidel, 2009), black shapes (Schiminovich et al., 2005), cyan circles (McLure et al., 2013; Ellis et al., 2013), light blue circles (Bouwens et al., 2014; Coe et al., 2013; Zheng et al., 2012; Oesch et al., 2013). The dark orange shaded region indicates the SFRD if bright IR sources are included (Magnelli et al., 2009, 2011, 2013).

illustrated in Fig. 1.4a taken from the Millennium Simulation (Springel et al., 2005). The filamentary structure and a large central node are clearly visible. Such simulations of dark matter are then used to predict the evolving distribution of baryons and the formation and evolution of galaxies, either using hydrodynamic, or semi analytic simulations (e.g. Springel et al., 2005; Keres et al., 2005; Croton et al., 2006; Baugh, 2006). Fig. 1.4b shows the simulated distribution of galaxies using the Millennium Simulation dark matter distribution and a semi analytic model (Croton et al., 2006). Galactic light is shown using colours chosen to represent the stellar rest-frame B-V colour index (B = 449nm (blue light) and V = 551nm (visual light)). The difference in magnitude at these two wavelengths is referred to as a colour and represents the degree of star formation taking place. Blue light indicates highly star forming and red light indicates older stars in passive galaxies. The distribution of galaxies clearly follows the dark matter structure, with galaxies forming preferentially along the filaments and a large galaxy cluster visible in the central dark matter node. This is in line with theoretical predictions and with the distribution of galaxies observed in large surveys (e.g. Colless et al., 2001). Both these figures were taken from the website of the Millennium Simulation Project [1].

[1] https://wwwmpa.mpa-garching.mpg.de/galform/virgo/millennium/

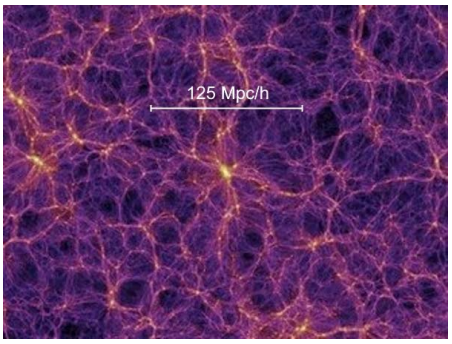

(A) Simulated distribution of dark matter at $z = 0$.

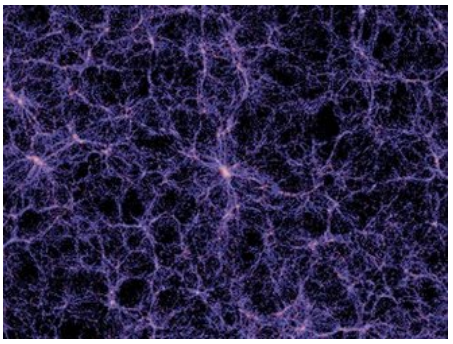

(B) Simulated distribution of light at $z = 0$.

FIGURE 1.4: These simulation snapshots (from the Millennium Simulation Project website[1]) show the distribution of dark matter (A) and galactic light (B) in the Universe today. In B the colours were chosen to represent the stellar restframe $B-V$ colour index. The large scale structure of filaments and nodes is clearly visible in both images.

Fig. 1.5 presents a close up view of the central rich $z = 0$ cluster from Fig. 1.4. The individual galaxies are visible in Fig. 1.5b and the corresponding dark matter distribution is shown in Fig. 1.5a. In such a rich, mature galaxy cluster, individual dark matter halos have merged to form a single large central halo containing many galaxies bound together in a gravitationally stable virialised system. Many of the galaxies have been quenched (appearing red in Fig. 1.5b). Close to the center of the cluster lies the brightest cluster galaxy (BCG), usually a giant elliptical galaxy, which has been fed both by streams of gas and satellite galaxies falling into the deepest point of the gravitational potential well (e.g. Dubinski, 1998; Zhao et al., 2017).

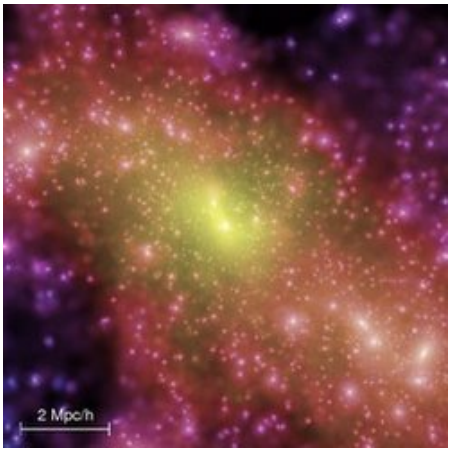

(A) Simulated dark matter within a rich cluster.

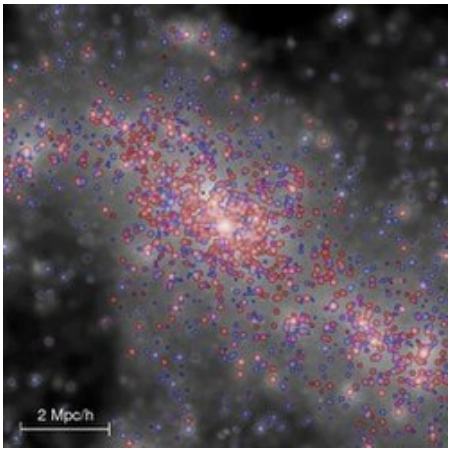

(B) Simulated galaxies within a rich cluster.

FIGURE 1.5: The distribution of dark matter (A) and galaxies (B) in a rich local cluster. These snapshots were taken from the Millennium Simulation Project website[1].

Simulations not only predict that galaxies form preferentially in the most dense regions of the Universe (Governato et al., 1998; Kauffmann et al., 1999; Cen and Ostriker, 2000; Benson et al., 2001), but also that they evolve more quickly than galaxies that form in regions of average density (Kauffmann, 1996; De Lucia et al., 2006; Gottlöber et al., 2001; Fakhouri and Ma, 2009). Such galaxies are predicted to have higher star formation rates and build up stellar mass

more quickly, both because of the large rate of infall of gas (accretion rate $\propto$ Mass$_{DMH}$ $\times$ (1 + z)$^{2.25}$, (Dekel et al., 2009)) and the increased chance of mergers taking place (the higher density of DMHs increases the likelihood of interaction and mergers). These dense regions, which will eventually become giant virialised clusters similar to that shown in Figure 1.5, provide an opportunity to study samples of co-evolving and interacting galaxies, acting as a laboratory for the study of galaxy evolution. Prior to virialisation such regions are called protoclusters and they are discussed in more detail in the next section.

1.2 Protoclusters

The formation history of giant ($>10^{14}$M$_{\odot}$), local galaxy clusters is revealed in state of the art simulations. These show individual DMHs, containing single or multiple galaxies, gradually merging together over billions of years to create a virialised system (e.g. Boylan-Kolchin et al., 2009; Chiang et al., 2013; Muldrew et al., 2015). Protoclusters first become detectable in such simulations at $z \sim$6 (Overzier, 2016), but a dominant central DMH may not emerge until $z <$2 (Overzier, 2016). In their simulation of $\sim$3000 M$>10^{14}$M$_{\odot}$ clusters Chiang et al. (2013) found that even the most massive clusters did not build up sufficient mass to be classified as clusters until $z \sim$2. By $z \sim$1 the protocluster may consist of several large halos of similar mass, some of which may be quite elongated. At $z = 0$ these halos will have merged into a single, spherical, massive halo. Although the merger history of clusters can easily be traced in simulations, it can difficult to predict from very high redshift observations ($z \sim$6) which galaxies will end up forming part of the final $z = 0$ cluster (Angulo et al., 2012).

DMHs containing multiple galaxies are by convention referred to as clusters if their mass is greater than 10^{14}M$_{\odot}$ and as groups if their mass lies between 10^{13}M$_{\odot}$ and 10^{14}M$_{\odot}$ (Bower and Balogh, 2004; Muldrew et al., 2015; Overzier, 2016). Using this definition of a cluster we can define protoclusters as a structure that will collapse to form a single, virialised DMH with mass $>10^{14}$M$_{\odot}$ by $z = 0$. Although other definitions appear in the literature this simple definition has become the preferred convention (Overzier, 2016) and will be used throughout this work. By this definition we would expect most protoclusters to pass through a stage where their most massive halo would be classified as a group before they build up sufficient mass to be defined as clusters.

Identifying a protocluster is problematic as we have to infer from observations that galaxies and their DMHs will actually collapse over time to form a single halo and that this halo will have the required mass. A first step is to identify an overdensity of galaxies and then obtain spectroscopic redshifts to confirm that they really are part of the same physically overdensity. However, there may be other galaxies that are not yet part of the overdensity at the era we are observing, but which will later come to form part of the cluster. In practice protoclusters are often identified as

overdensities of galaxies, with an assumption that all the galaxies within the overdense region will form part of the final structure.

Early searches for protoclusters focused on high redshift radio galaxies which are thought to trace the most dense regions of the Universe (Le Fevre et al., 1996; Venemans et al., 2002, 2004, 2005, 2007; Stern et al., 2003; Hatch et al., 2009; Matsuda et al., 2009). More recently many protoclusters have been identified as overdensities of Lyman break galaxies (LBGs, see section 1.4.1.1) and Lyman-α emitters (LAEs, see section 1.4.2) in large galaxy surveys (Steidel et al., 1998, 2000; Ouchi et al., 2005; Matsuda et al., 2010). A recent review (Overzier, 2016) found that $\sim$40 protoclusters have been confirmed to date, with approximately half lying at $2 < z < 3$ and the rest at $3 < z < 8$. The concentration of protoclusters at $2 < z < 3$ is partly due to the technological problems associated with detecting high redshift galaxies. However, the number density of dark matter halos of $10^{12}-10^{14}$M$_{\odot}$ falls rapidly between $3 < z < 8$ (Mo and White, 2002; Guo et al., 2013). Thus, whilst there are no doubt many protoclusters still to be discovered, the bias towards lower redshift is likely to persist.

Currently confirmed protoclusters have a median predicted $z = 0$ mass of log(M/M$_{\odot}$)$_{z=0}$ = 14.6 and include several with log(M/M$_{\odot}$)$_{z=0}$ $\geq$15 (Venemans et al., 2002; Steidel et al., 2005; Cucciati et al., 2014; Lemaux et al., 2014). The $z = 0$ cluster mass can be predicted using the spherical collapse model which sets $M_{z=0} = \bar{\rho} V_{true}(1 + \delta_m)$, where $M_{z=0}$ is the mass of the DMH at $z = 0$, $\bar{\rho}$ is the $z = 0$ mean density of the Universe, V_{true} is the comoving volume of the protocluster in real space and δ_m is the dark matter mass overdensity (Steidel et al., 1998). Difficulties in measuring V_{true} arise due to redshift space distortions (Kaiser, 1987). These are caused by the peculiar motions of the galaxies, causing the overdensities to be slightly compressed in redshift space and therefore the measured overdensity to be overstated. Another complexity is that we can only directly measure the overdensity of galaxies, δ_{gal}, and so δ_m must be inferred. A value for the galaxy bias, $b = \delta_{gal}/\delta_m$, is obtained from simulations and a value for δ_m can then be obtained.

Alternatively observations can be compared to simulations, which allow for non spherical collapse and are hence closer to the actual behaviour of protoclusters (Governato et al., 1998; Suwa et al., 2006; De Lucia and Blaizot, 2007; Venemans et al., 2007; Chiang et al., 2013, 2014, 2015; Muldrew et al., 2015; Hatch et al., 2016). Simulations can also be fine tuned to take account of observational effects, such as distance, dust extinction and instrument limitations (e.g. resolution), allowing a better match to actual observations at a given redshift. Chiang et al. (2013) found evidence for a strong correlation between high-redshift overdensities of galaxies (at least up to $z \sim$5) and the mass of their corresponding $z = 0$ cluster. In their review Overzier (2016) found that the $M_{z=0}$ values predicted using these more advanced simulations, log(M/M$_{\odot}$) $\approx$14-15.5 (e.g. Governato et al., 1998; Lemaux et al., 2014; Chiang et al., 2015), are in agreement with those calculated using the spherical collapse model .

As mentioned in the previous section, galaxies in protoclusters are expected to evolve more quickly than galaxies in the average field. However, it is unclear at what stage this difference in physical properties first emerges. Kato et al. (2016) found that clusters and protoclusters form a SFRD versus redshift sequence significantly above the Madau and Dickinson (2014) relationship, with $2< z <3$ protclusters having a SFRD $10^3 - 10^4$ times higher than the global SFRD. $z = 0$ clusters are dominated by passive elliptical galaxies and a number of studies have attempted to determine when this switch from highly star forming to quiescent galaxies first becomes apparent (e.g. Zirm et al., 2008; Kuiper et al., 2010; Koyama et al., 2013; Cucciati et al., 2014; Lemaux et al., 2014). Zirm et al. (2008) found some evidence for an overdensity of red galaxies (defined as $1.1 < (J - H) < 2.1$ and $J < 26.7$ AB magnitude) in one of the best known protoclusters, that associated with the Spiderweb radio galaxy at $z = 2.2$. However, this was based on photometric redshifts and observations show that most galaxies in the Spiderweb protocluster are still star forming. A lack of spectroscopic redshifts is a common problem when studying protocluster galaxies, particularly those detected at longer wavelengths (longward of NIR). One exception is a study by Lemaux et al. (2014) which detected an overdensity of red galaxies in a protocluster at $z \sim 3$ using spectroscopic redshifts. These galaxies showed no sign of recent star formation (in the last $\sim$300Myr). A recent simulation (Contini and Kang, 2015), combining an N-body simulation and a semi analytic model, indicated that the fraction of passive galaxies in clusters and groups/protoclusters was $\leq$20% at $z \sim$3, $\sim$30% at $z \sim$2 and $\sim$60% at $z \sim$1. This is in reasonable agreement with observations (Overzier, 2016).

Observational evidence for accelerated galaxy growth due to a higher merger rate has been found both in the form of an enhanced merger fraction in protoclusters at $z = 1.62$ and ~ 2.5 (Lotz et al., 2013; Casey et al., 2015) and an enhanced AGN fraction in a $z = 3.1$ protocluster (Lehmer et al., 2009; Kubo et al., 2013). Studies at $2 < z <$2.5 have found indications that protocluster galaxies are more massive than those in the field (Steidel et al., 2005; Hatch et al., 2011; Koyama et al., 2013; Cooke et al., 2014), whereas studies at $z \sim 3$ show mixed results (Lehmer et al., 2009; Kuiper et al., 2010; Lemaux et al., 2014; Cucciati et al., 2014; Alexander et al., 2016) and at $z > 3.5$ no difference is detected (Overzier et al., 2008, 2009).

It remains unclear when protocluster galaxies first start to show the effects of their environment, but, based on current observations, it seems likely that differences become detectable at $2.5< z <3.5$. This is one of the key questions addressed in this work which focuses on the most widely studied protocluster at $z = 3.1$, which I introduce in the next section.

1.3 The SSA22 Protocluster

A $z = 3.1$ protocluster was first detected in the SSA22 field (R.A. = 22h,17m, Dec. = +00deg 15′) by Steidel et al. (1998) as an overdensity of LBGs six times the average field density at this redshift. Narrow band Lyman-α (Lyα) imaging has identified additional $z = 3.1$ galaxies, LAEs, in a larger region around the original overdensity, extending for more than 60 comoving Mpc (Steidel et al., 2000; Hayashino et al., 2004; Yamada et al., 2012) and thought to trace several dark matter filaments intersecting to form a density peak (Matsuda et al., 2005). It is thought to be a rare high-density peak that will evolve to form a massive (10^{15}M$_{\odot}$) cluster or supercluster by $z = 0$ (Steidel et al., 1998; Yamada et al., 2012). A recent spectroscopic survey identified two redshift peaks at z =3.069 (blue peak) and z =3.095 (red peak, Topping et al., 2016), $\Delta v \sim$1900 kms^{-1} and $\sim$24 comoving Mpc along the line of sight, suggesting that there are in fact two distinct physical structures. It is expected that these will merge to form a local cluster, but further observations over a larger region are needed to determine the full extent of the two structures.

Overdensities of other objects have also been detected within the protocluster:

a) Lyα blobs (LABs) are large regions of diffuse Lyα emission that are preferentially associated with overdense regions in the distant Universe (Steidel et al., 2000; Matsuda et al., 2004; Geach et al., 2014, 2016; Matsuda et al., 2011). The SSA22 protocluster is rich in LABs, containing 35 in total, indicating the presence of large reservoirs of cold gas. The processes powering the Lyα emission in these regions remains uncertain and I address this subject in more detail in Chapter 4.

b) An overdensity of AGN was detected by Lehmer et al. (2009) and has now been identified with the red peak (Topping et al., 2016).

c) Submillimetre galaxies (SMGs, see section 1.4.5) have been detected in large submillimetre (submm) surveys and followed up with more targeted observations (Chapman et al., 2001, 2004; Geach et al., 2005; Tamura et al., 2009; Geach et al., 2014, 2016, 2017; Umehata et al., 2014, 2015). Overdensities were identified at 850μm and 1.1mm wavelengths, but were not detected at shorter wavelengths (250μm, 350μm Kato et al., 2016). The 1.1mm overdensity is located within the red peak.

d) An overdensity of massive red, galaxies has also been identified within the protocluster (Uchimoto et al., 2008; Kubo et al., 2013; Uchimoto et al., 2012; Kubo et al., 2015). In their photometric study Kubo et al. (2013) found that $\sim$50% of the most massive galaxies ($\geq 10^{11}$M$_{\odot}$) have colours consistent with passive galaxies, whilst $\sim$30% are probably dusty star forming galaxies. These massive galaxies also have a higher association with AGN than similar galaxies in the field and are strongly associated with LABs (Uchimoto et al., 2012). Following up this work with a spectroscopic study to confirm protocluster membership Kubo et al. (2015) found

that five of the reddest galaxies are quiescent with stellar masses $10^{10.9} - 10^{11.5}$M$\odot$. Such high mass passive galaxies are relatively rare at this redshift ($\sim 10^{-3}$-10^{-5} Mpc^{-3} (Tomczak et al., 2014)) and they suggest that we are starting to see the build up of passive galaxies, although the protocluster is still dominated by star formation. At the centre of the protocluster Kubo et al. (2016) recently discovered a dense group of seven massive galaxies within 180kpc separation, five of which had masses greater than $10^{10.5}$M$\odot$. The total stellar mass of these galaxies was found to be $5.8^{+5.1}_{-2.0} \times 10^{11} M_{\odot}$ and they are predicted to merge and form the BCG of the future local cluster. At a redshift of z =3.09 this group lies within the red peak.

Lehmer et al. (2009) found evidence that the LBGs in SSA22 are $\geq$ 1.2 – 1.8 times as massive as those in the field, however, Alexander et al. (2016) found no difference in the mass of AGN in the SSA22 protocluster and the field. Kubo et al. (2015) have detected massive quiescent galaxies within the protocluster, but it is still unclear clear whether they are statistically more massive than those in the field. I address this question of enhanced mass further in Chapter 3.

1.4 Detecting High-redshift galaxies

High-redshift galaxies, such as those lying in the SSA22 protocluster, are hard to detect, because their extreme distance causes them to appear faint and unresolved. Specific detection techniques have therefore been developed to overcome these problems. Different methods will select galaxy populations with different physical properties and it is important to ensure that this is taken into account when comparing different samples.

1.4.1 The Lyman-Break Method

LBGs are identified by the Lyman break in their Spectral Energy Distributions (SED, e.g. Steidel and Hamilton, 1992, 1993; Madau, 1995; Steidel et al., 1996). The break is a result of neutral hydrogen absorbing photons shorter than 912Å rest frame. Such ultraviolet (UV) continuum photons are produced by luminous young stars and then absorbed by the hydrogen clouds surrounding star-forming regions. The effect may also be enhanced by further absorption in neutral hydrogen clouds along our line of sight. UV light is blocked by the Earth's atmosphere, but at high redshift ($z \sim 3$) the break is redshifted to optical wavelengths, see Fig. 1.6, making it easier to detect from ground-based telescopes.

The Lyman-break method involves observing at two or three wavebands either side of the break. The wavebands used vary depending on the redshift at which galaxies are to be detected. For example the u ($\sim$3600Å), and r ($\sim$6580Å) bands can be used to detect starburst galaxies at a redshift of $z = 3.1$, where the redshifted Lyman break lies at $\sim$3700 Å, as illustrated in Fig 1.6.

A third waveband can be used to try and eliminate potential contaminants, such as low mass stars or early-type galaxies at lower redshift. For example Steidel et al. (2003) used an initial colour selection criteria of G - R $\leq$ 1.2 and (U_n - G) $\geq$ (G-R) + 1.0, as illustrated in Fig. 1.7, where the region corresponding to the selection criteria is shown in yellow. Evolutionary tracks show how the colours of different types of galaxies with and without dust extinction evolve from $z = 4$ (top) to $z = 0$. Star forming galaxies pass through the selection area at high redshift with and without dust extinction. The elliptical galaxy only passes through this region if dust extinction is included and then only for a relatively short period. No low redshift galaxies lie in the selection region. The SSA22 LBGs are also shown in the figure as purple stars.

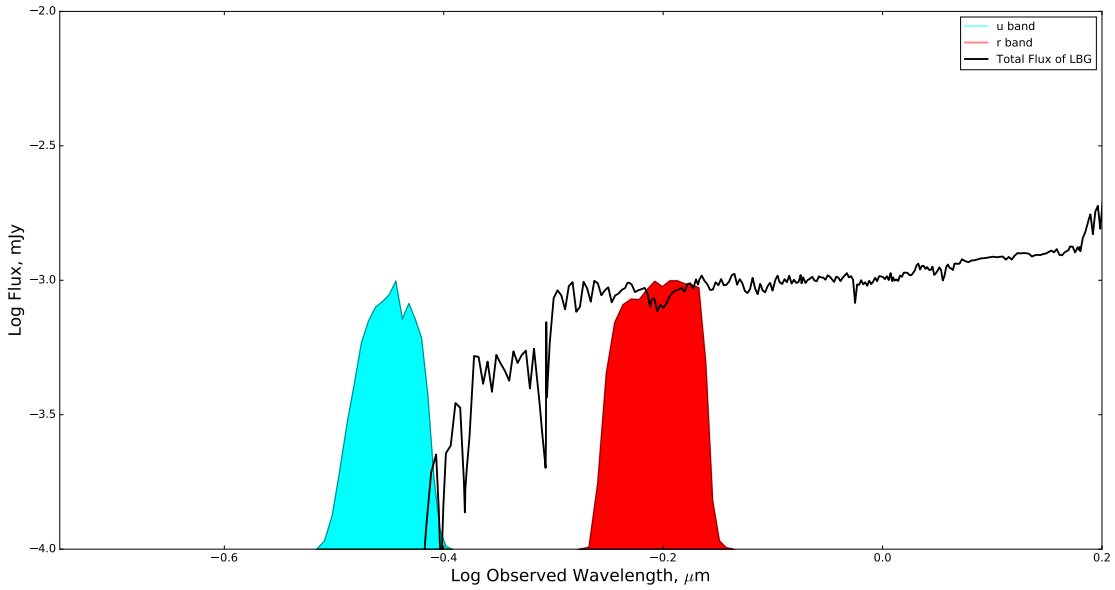

FIGURE 1.6: The Lyman break redshifted to ∼3700 Å for an LBG at $z = 3.1$. The u and r bands fall either side of the break.

1.4.1.1 Lyman-Break Galaxies

Recent studies of LBGs suggest a wide range of stellar mass, $10^{9-11}M_{\odot}$ (Shapley et al., 2005; Stark et al., 2009; Magdis et al., 2010b). LBGs detected at $z \geq 2$ have a range of SFRs, from 10s - 100s $M_{\odot}yr^{-1}$ (Shapley et al., 2005; Magdis et al., 2010b,a; Coppin et al., 2015) and UV to optical SEDs similar to local Irregulars (Papovich et al., 2001). They are generally smaller and more compact than comparable local galaxies, with half-light radii ($r_{1/2}$) of 2-3 kpc, making them closer in size to local large bulges and intermediate luminosity ellipticals (Giavalisco, 2002). Some are relatively regular, whilst others are highly irregular, fragmented with bright blobs, or multiple systems, suggesting that mergers and interactions are common (Giavalisco, 2002).

Shapley et al. (2003) studied the rest frame UV spectroscopic properties of a large sample of LBGs at $z \sim 3$. They propose a scenario with an inner HII region on scales $\sim r_{1/2}$ where massive

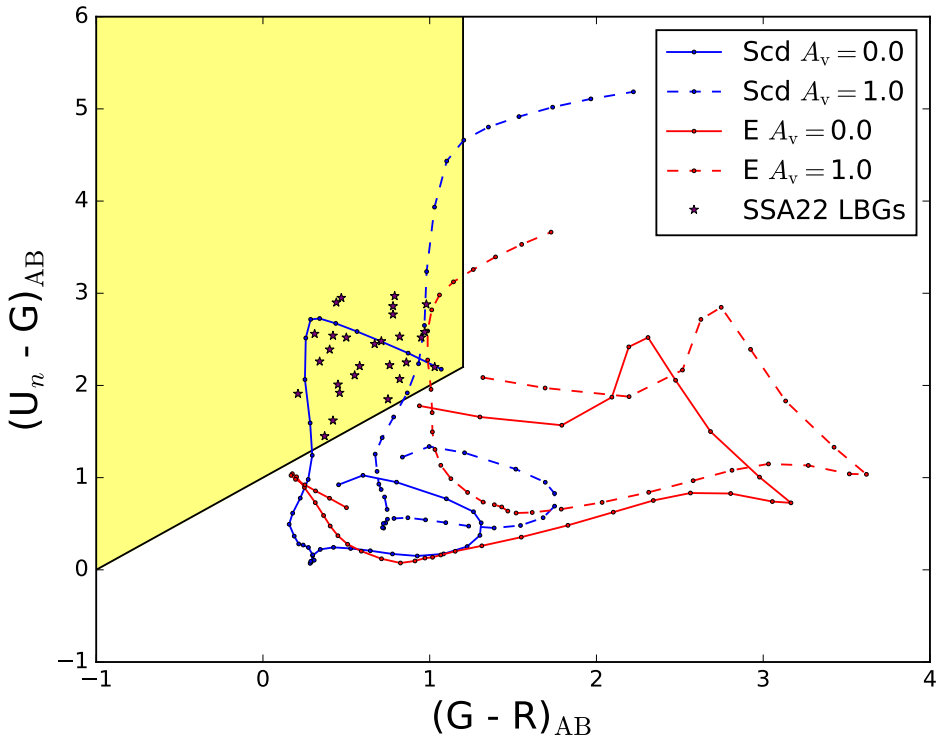

FIGURE 1.7: A colour-colour plot showing the LBG selection criteria from (Steidel et al., 2003) in yellow. The LBGs detected in the SSA22 protocluster are shown as purple stars. Evolutionary tracks (from z =4 to z =0, intervals of z =0.1 are indicated) are shown for a star forming (Scd) and elliptical (E) galaxy template (from the hyperz catalogue (Bolzonella et al., 2000), based on the Coleman, Wu and Weedman templates (Coleman et al., 1980) extended further into the UV and IR regions using Bruzual and Charlot (2003) parameters). Solid lines are with A_v =0 (no dust extinction), dashed lines with A_v =1.0.

stars are forming. This region generates the observed Lyα emission, UV stellar continuum and UV and optical emission lines. Type II supernova within the HII region generate a large bubble of hot, ionized gas which expands at several 100 kms^{-1}, taking clouds of dusty, cold gas with it. The distribution and velocity of the entrained cold gas, as well as its dust content, largely determines the apparent morphology of the LBGs. Shapley et al. (2003) also point out two important differences between LBGs and local starburst galaxies. Firstly, star formation in local starbursts is often concentrated in a region of $\leq$1kpc radius, compared to the larger 2-3kpc scale for LBGs. Secondly, local starburst galaxies often have large discs of gas which force outflows to expand perpendicularly to the plane of the disc, such gas discs have not been found in the LBGs. Kornei et al. (2010) compared two groups of LBGs with strong and weak Lyα emission (Lyα equivalent width $\geq$ 20 Å and Lyα equivalent width $<$ 20 Å). They found that strong emitters were older, had lower SFRs and were less dusty (at 3-5σ). These LBG may represent a later stage of evolution, where the supernova outflows have reduced the dust content, allowing more Lyα to escape.

Pettini et al. (2001, 2002) found LBGs ranging from 35 - 300Myr old, whilst Shapley et al. (2001, 2005), Rigopoulou et al. (2006) and Magdis et al. (2010b) detected LBGs as old as

$\sim$1Gyr. The oldest have been found to be the most massive ($\geq 1 \times 10^{11} M_{\odot}$, Magdis et al., 2010b) and to have less dust and lower SFRs according to the correlations found by Shapley et al. (2001) and now confirmed by the Kornei et al. (2010) study of strong and weak Lyα emission. Hydrodynamic cosmological simulations suggest a mean age of stars at z =3 of $\geq$ 1 Gyr (Nagamine et al., 2001). de Barros et al. (2014) studied the impact of different models on the physical properties determined for LBGs and found an even wider range of ages, 4Myr - 1.5Gyr, for their $z \sim$4 sample, with a strong dependence on whether or not nebulae lines are included in the SED fitting (see Section 1.5.2 for a description of SED fitting).

A near-infrared spectroscopic study of LBGs at z $\sim$ 3 placed constraints on their metallicities, indicating a range of 10-50% $Z_{\odot}$ based on [OII] λ3727, Hβ and [OIII] λ5007 line ratios (Mannucci et al., 2009). However, Nagamine et al. (2001) hydrodynamic cosmological simulation suggested that more massive LBGs ($> 10^{10} M_{\odot}$) may have much higher metallicities approaching solar and such high metallicities are also favoured by Erb et al. (2006) and Shapley et al. (2004).

1.4.2 Lyman-α emitters

High redshift galaxies can also be detected by searching for the redshifted prominent Lyα emission line (1216Å rest frame) using narrow-band filters. This technique was first used to search for companions to a $z \sim$3 QSO (Djorgovski et al., 1985), but modern instruments now allow large narrow-band surveys to detect 100s of Lyman-α emitters (LAEs, e.g. Hayashino et al., 2004; Ouchi et al., 2008). The Lyα emission could be due to photoionization caused by massive stars, or AGN. LAEs are star-forming galaxies, but with lower SFRs ($\sim$1-10$M_{\odot}$yr^{-1}) than the starbursting LBGs and little dust (Ouchi et al., 2008; Nilsson et al., 2007).

LAEs are generally younger (<1Gyr, age falling with increasing redshift) and less massive ($\sim 10^{8-9} M_{\odot}$ at $z \sim$3) than LBGs, with low metallicity ($\sim$0.05$Z_{\odot}$, Pirzkal et al., 2006; Nilsson et al., 2007; Gawiser et al., 2007; Finkelstein et al., 2015). However there is a degree of scatter and some overlap between the two populations, indeed the Lyα emitting LBGs in the Kornei et al. (2010) sample were found to be older and of equivalent mass to non emitting LBGs. LAEs may therefore represent more than one stage of galaxy evolution. Gawiser et al. (2007) compared the number density of LAEs and DMHs and predicted that LAEs will evolve into z =0 galaxies with a range of masses, but a median $\sim L^{\star}$ (the knee of the galaxy luminosity function), whereas the LBGs will evolve into higher mass galaxies.

1.4.3 Hydrogen-α emitters

A similar NIR narrow-band method can detect galaxies emitting strongly in Hydrogen-α (Hα, 6563Å rest frame). Hα is emitted from hydrogen gas clouds that have been ionized by young, luminous stars and therefore acts as an excellent tracer for star formation (Kennicutt, 1998; Geach et al., 2008; Oteo et al., 2015). As it lies in the optical range (for $z \lesssim 3$) it is less susceptible to dust extinction than Lyα (see section 1.4.7) and can be used to detect galaxies that are not detected by the LAE method. Oteo et al. (2015) found evidence to support this as only $\sim$4.5% of their Hα emitter (HAE) sample could be detected as LAEs. They also found that Hα was useful for detecting star-forming galaxies with a wide range of SFRs and masses from the local Universe to $z \sim 2.5$, at which point it redshifts to $\lambda_{obs} > 2\mu$m and becomes harder to detect with current ground-based telescopes. An HAE sample will be less biased than an LAE sample of galaxies, which will tend towards low mass and high SFR. Large HAE samples are therefore particularly useful for tracing the evolution of SFRD.

1.4.4 Colour Selections

Different combinations of optical and NIR broadbands may be used to select for high-redshift galaxies that may be missed by Lyman-break searches. These colour selections tend to be sensitive to older populations of stars, or more dusty star-forming galaxies than the LBG and LAE selection techniques. Some examples are given below:

- **BM/BX** selects galaxies at $1.4 \leq z \leq 2.2$ (BM) and $2.2 \leq z \leq 2.8$ (BX) using different combinations of optical broadband filters. These colours were tuned to select galaxies at a lower redshift than the optimum range of Lyman break searches at the time (i.e. $z \leq 2.5$, Adelberger et al., 2004).

BM	**BX**
$(G-R)_{AB} \geq -0.2$	$(G-R)_{AB} \geq -0.2$
$(U_n - G)_{AB} \geq (G-R)_{AB} - 0.1$	$(U_n - G)_{AB} \geq (G-R)_{AB} + 0.2$
$(G-R)_{AB} \leq 0.2(U_n - G)_{AB} + 0.4$	$(G-R)_{AB} \leq 0.2(U_n - G)_{AB} + 0.4$
$(U_n - G)_{AB} < (G-R)_{AB} + 0.2$	$(U_n - G)_{AB} < (G-R)_{AB} + 1.0$

- **BzK** uses optical and NIR broadbands to select star forming galaxies at $1.4 \leq z \leq 2.5$ (Daddi et al., 2004). Beyond $z \sim 2.5$ it is hard to differentiate between dusty starforming and lower redshift evolved galaxies using this method.

  $(z-K)_{AB} - (B-z)_{AB} \leq -0.2$
  $(z-K)_{AB} > 2.5)$

- **Distant red galaxies (DRGs)** are detected by their Balmer/4000Å break, which has redshifted to the NIR bands at $z \sim 2$ (Franx et al., 2003; van Dokkum et al., 2003). Half the galaxies detected by this method are thought to be $z \sim 2$ passives, whilst the rest are dusty galaxies with a range of redshifts.

  $(J_s - K_s)_{\text{Johnson}} > 2.3$

- **Extremely Red Objects (EROs)** and **Extremely Red Galaxies (ERG)** are selected using NIR and optical bands and cover a wide range of redshift and mass. They include both young dusty starforming, old elliptical and dusty old galaxies (Daddi et al., 2000; McCarthy et al., 2004; Caputi et al., 2004). For example:

  $(R_s - K_s)_{\text{AB}} > 5.0$ (EROs, Daddi et al., 2000)
  $(I_{775} - K_s)_{\text{AB}} > 3.92$ (ERGs, Caputi et al., 2004)

1.4.5 Far infrared and Submm

The far infrared ($\sim$30-200μm, FIR) and Submm wavelengths can be used to detect dust obscured high redshift galaxies with very high SFRs (100-1000 $M_{\odot} yr^{-1}$) which may not be detectable in UV/optical wavebands (Chapman et al., 2005; Casey et al., 2014). Dust in these galaxies is heated by radiation from young stars and then re-emits energy as a modified black body which peaks in the FIR. A perfect black body has a characteristic radiation curve which peaks at a frequency that depends on the temperature of the body ($\nu \propto$ T) and the FIR peak can therefore be used to determine dust temperature.

Increasing redshift causes the submm and millimetre bands to trace the SED at increasing frequency and hence move towards the peak of the SED (Blain and Longair, 1993), as illustrated in Fig. 1.8 . In this figure the λ =450μm and λ =1mm wavebands are indicated by two vertical lines, highlighting a range where there is little change in flux density from $1 \leq z \leq 6$. This negative K correction allows dusty star forming galaxies (DSFGs) to be be observed at almost constant flux density over a wide range of redshifts, $1 \leq z \leq 8$ (Casey et al., 2014).

DSFGs are thought to undergo a series of intense starbursts which may be the result of gas rich mergers (e.g. Wang et al., 2011; Hayward et al., 2011; Magnelli et al., 2012), or highly efficient star formation from cold streams (Targett et al., 2013; Davé et al., 2010; Hayward et al., 2011). These starbursts generate significant amounts of dust, which then obscure UV light from young stars in the same or later starbursts. DSFGs are predicted to evolve into massive current-day ellipticals found at the centre of clusters (Smail et al., 1998; Lutz et al., 2001; Ivison et al., 2000; Casey et al., 2014). These galaxies are also referred to as submm galaxies (SMGs) as they were first detected at submm wavebands (Smail et al., 1997; Hughes et al., 1998).

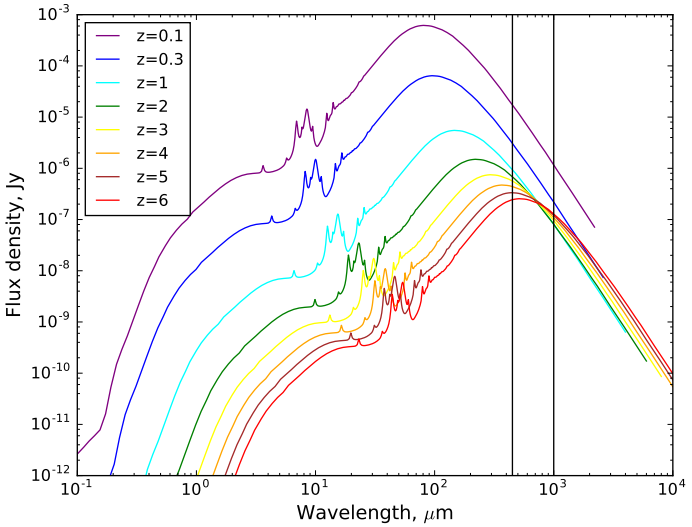

FIGURE 1.8: Model SED of a starburst galaxy (from the Siebenmorgen and Krügel (2007) catalogue) redshifted between z =0.1 and z =6. The two vertical lines indicate λ =450μm and λ =1mm. At these wavelengths the negative K correction means that the flux density of the galaxy stays fairly constant as redshift increases.

Submm telescopes such as the James Clerk Maxwell Telescope (JCMT), The Submm Array (SMA), the Atacama Pathfinder Experiment (APEX) and more recently the Atacama Large Millimeter/submillimeter Array (ALMA)can to take advantage of the negative K correction. The highest redshift confirmed detection of a DSFG so far is at $z \sim$8 (Laporte et al., 2017). Attempts to measure the stellar mass of DSFGs give a range of results (10^{10} - 10^{11} $M_{\odot}$) (Casey et al., 2014). This may be a genuine variation within the population, but there are also uncertainties involved in determining accurate mass values, such as the choice of inputs in SED modelling (see Section 1.5.2) and AGN contamination (Hainline et al., 2011; Michałowski et al., 2012a; Casey et al., 2014). Early observations with single-dish telescopes had low resolution and submm interferometers have now revealed that many single-dish objects are actually made of up of several dusty galaxies, which may or may not be physically associated (Wang et al., 2011; Hodge et al., 2013; Hayward et al., 2013; Umehata et al., 2017). This will have an impact on both number counts and the physical properties derived for these objects. Some DSFGs may have lower SFRs than was once thought.

1.4.6 Radio

Radio wavelengths (>1mm) have also proven effective at detecting high-redshift galaxies containing AGN (e.g. Lilly, 1988; Rawlings et al., 1996; van Breugel et al., 1999; De Breuck et al., 2010). The radio waves are generated by the acceleration of relativistic particles in the magnetic fields associated with the active galaxy (synchrotron radiation). The emission is from jets that can stretch for millions of light years. In the 1980s and 90s radio telescopes were used to find

high redshift galaxy candidates by searching large areas of the sky. These candidates could then be followed up with targeted observations at other wavelengths to determine their redshift. This was a relatively cheap (in terms of telescope time) way to find high-redshift galaxies and was the dominant method of detection until the introduction of the alternative methods mentioned above.

As previously described, radio-loud galaxies can provide useful signposts to identify high-density regions in the cosmic web (Venemans et al., 2003) and have been used to locate protoclusters. Radio jets are usually associated with massive elliptical galaxies (e.g. Begelman et al., 1984; Lilly, 1988), or their progenitors (some studies revealing evidence of mergers) (e.g. Heckman et al., 1986; McCarthy, 1993; Tombesi et al., 2017) . At the highest redshifts (z >4) they may be tracing an early stage in the evolution of elliptical galaxies before they build the bulk of their stellar mass (e.g. Rawlings et al., 1996; van Breugel et al., 1999), but they are still likely to be some of the most massive and evolved galaxies at a given epoch. AGN are also of interest to help us understand the role of feedback in galaxy evolution.

Radio telescopes can also detect supernova in galaxies, which can be used as a tracer for star formation. However, radio astronomy is less useful for studies aimed at understanding the properties of typical high-redshift star-forming galaxies as it can be hard to disentangle emission from the accretion disc and star formation.

The field of radio astronomy is expected to be revolutionised by the Square Kilometre Array (SKA), a radio interferometer currently under construction that will eventually have over a square kilometre of collection area. The increased sensitivity and resolution will allow the detection of radio galaxies at record breaking redshift, the detection of fainter radio galaxies at intermediate redshift ranges (reducing current potential selection bias) and the resolved study of radio galaxies at higher redshift than is currently possible.

1.4.7 The impact of Dust

Dust has a significant impact on light reaching us from distant galaxies. Dust grains in the ISM are similar in size to the wavelength of blue light and therefore blue light from distant galaxies is easily absorbed and scattered out of our line of sight. This has the effect of 'reddening' the light that reaches us. The degree of reddening is inversely proportional to the wavelength of optical light, so that short wavelengths (blue light) are more reddened than long wavelengths (red light). The degree of reddening can be expressed as:

$$E(B-V) = (B-V) - (B-V)_0 \tag{1.4}$$

Where (B-V) is the observed colour and $(B\text{-}V)_0$ is the intrinsic colour of the object. Extinction, A_v, is a measure of the absorption and scattering (out of our line of sight) by foreground dust and it is related to reddening by the relation:

$$A_v = R_v \times E(B-V) \tag{1.5}$$

R_v depends on the average size of dust grains and a typical Milky Way value is $\sim$3 (measured in V band), although it varies with line of sight (e.g. Gottlieb and Upson, 1969; Massa and Savage, 1989; Cardelli et al., 1989; Valencic et al., 2004). In addition the Milky Way extinction curve has a 'bump' at $\sim$2175Å where extinction is increased (e.g. Massa and Savage, 1989; Valencic et al., 2004). The extinction curve will vary for other galaxies if they have different dust grain properties. The Large Magallenic Cloud has a smaller 2175Å bump and the Small Magallenic Cloud no bump, whilst they both have more extreme extinction than the Milky Way in the Far UV (FUV) in particular regions (e.g. Fitzpatrick, 1986; Gordon et al., 2003).

Dust within high-redshift galaxies can also affect our observations. Here the stars are embedded in the dust and the light will be absorbed and scattered out of and into our line of sight. The net effect of the dust can be quite complex as it will depend on the geometric configuration of the dust, which may be smooth or clumpy. Observations of local starburst galaxies were used to create an attenuation curve designed to correct observations for the effects of dust both along the line of sight and in the starbursting galaxy (Calzetti et al., 2000). This is often applied to observations of high-redshift starbursting galaxies too, but such adjustments do not take account of variations in dust concentrations in different parts of a galaxy. These could lead to significant differences in attenuation depending on the angle at which a galaxy is viewed. In addition the application to high-redshift galaxies assumes that the attenuation is similar to that in local starburst galaxies, which may not be the case.

Dust could lead to confusion between very dusty galaxies at lower redshifts and high-redshift starforming galaxies, both of which would appear to be red. This could have an impact on the determination of physical properties (see next section). Sawicki and Yee (1998) found that LBGs were obscured by enough dust (E(B - V) $\sim$ 0.3) to reduce their observed UV fluxes by a factor of more than 10. More recent studies of LBGs have found E(B - V) ranging from 0 to $\sim$ 0.4 (Shapley et al., 2001, 2005) and A_v =0 to 2mag (de Barros et al., 2014).

1.5 Determining the physical properties of high-redshift galaxies

In order to understand the impact of environment on the evolution of galaxies we need to be able to determine their physical properties, such as mass, star-formation rate, age, etc. This is not a

straightforward process, but I introduce two common approaches below.

1.5.1 Luminosity calibrations

Photometry of certain individual wavelengths or limited ranges of wavelengths (e.g. R, Hα, 1.4GHz, FUV, Total IR (TIR)) is often used to calculate physical properties such as SFR and mass. FUV luminosity is related to SFR as it traces the light from young, massive OB stars. These stars have short lives and so the detection of light at these wavelengths indicates recent star formation. Optical and NIR wavelengths trace the older, less massive, but more numerous stellar population, which dominates the overall stellar mass of galaxies. They are therefore more useful for determining mass. TIR emission is also useful for calculating the SFR as it is dominated by the light from young stars that has been absorbed by dust and re-emitted. H-α is emitted from hydrogen gas clouds that have been ionized by young, luminous stars and therefore also traces star formation. 1.4GHz is thought to trace the synchrotron emission from Type II supernovae, which is in turn related to star formation.

An example of how luminosity and physical properties are related is given by the Madau et al. (1998) relationship:

$$SFR/\ M_{\odot} yr^{-1} = cL_{\nu} \tag{1.6}$$

where L_{ν} is the luminosity density and c is a constant dependent on the initial mass function (IMF) and the wavelength (values for c have since been revised in Kennicutt and Evans (2012)). The IMF describes the distribution of initial mass for a population of stars. It was originally described as a power law, the number of stars increasing with decreasing mass (Salpeter, 1955). However, this was found to overestimate the number of low-mass stars and later versions turn over at the low-mass end of the distribution (e.g. Chabrier, 2003; Kroupa and Weidner, 2003). The constant c in the above equation is IMF-dependent because the ratio of high to low mass stars will impact on how a given luminosity is related to mass or SFR. For example the 1.4GHz luminosity is linked to the SFR via supernovae, which in turn depends on the number of massive stars. The overall SFR for the galaxy will therefore be impacted by assumptions about the relative number of high and low mass stars.

The calibrations in Kennicutt and Evans (2012) are based on synthetic models of a dusty starburst galaxy and are constrained by actual observations. Telescopes, such as the Galaxy Evolution Explorer (GALEX) have helped to improve the constraints, leading to the revised calibrations presented in Kennicutt and Evans (2012). However these relationships still require a number of assumptions about IMF, dust attenuation and emission, star formation histories etc.

Bell et al. (2003) calculated mass to luminosity ratios (M/L) for a range of optical and NIR wavebands at $z = 0$. These can then be used to calculate mass from observed luminosities. The M/L have systematic errors of $\sim$30% due to uncertainties about dust and star-formation histories. Varying the amount of dust will have an impact on mass due to extinction effects (see section 1.4.7) and varying the timing of the last burst of star formation will also effect how luminosity is interpreted (a more recent burst would predict a higher luminosity at shorter wavelengths, as the younger, more massive stars would still be emitting). In a more recent paper Norris et al. (2016) investigated the uncertainties effecting M/L ratios and conclude that using the *Wide-field Infrared Survey Explorer* W1 band (3.4μm) leads to stellar masses with typical uncertainties $<$13%, whereas using R band gives uncertainties at least two to three times higher. However, these M/L ratios are for local galaxies (quiescent elliptical galaxies in the case of Norris et al. (2016)) and it is not clear that they can be reliably applied to high-redshift galaxies.

These approaches have the advantage that they can be used where multiwavelength photometry is not available, but they are considered less reliable than the mutliwavelength SED fitting approach discussed in the next section.

1.5.2 SED fitting

Physical properties can also be determined using multiple wavelengths to try to fit model SEDs to observed photometry (e.g. Conroy, 2013). This approach is often considered more reliable as it makes use of a larger data set and allows the exploration of a larger parameter space. Typically a set of population synthesis model templates will be taken as a starting point (e.g. Bruzual and Charlot (2003), Maraston (2005)) and then the photometry modified for different models/levels of dust absorption and emission, stellar formation histories and metallicities. The model templates are based on a library of stellar evolutionary tracks, showing how stars of different initial masses and metallicities will evolve, combined with a library of individual stellar spectra which describe the spectra of stars at any position on the Herzsprung-Russell diagram. Spectra can therefore be produced for each star and evolved according to the model parameters.

Assuming a series of instantaneous bursts of star formation a simple stellar population (SSP) is generated (in which all stars form at the same time and have the same metallicity) and a galaxy SED can be produced by summing the individual luminosities of stars. The IMF used will clearly have an impact as it determines the relative proportion of high and low mass stars. An alternative is to use a composite stellar population (CSP), this is more complex than an SSP as the stars may vary in age and metallicity. The most popular form of CSP is the exponential model where SFR $\propto \exp(-t/\tau)$ (t = time). Some fitting codes also allow for the effect of AGN and nebular emission lines to be taken into account.

The modified SED is then redshifted as required and compared to the observed photometry to find a best fit. (SED fitting can also be used to determine a photometric redshift, but spectroscopic redshifts will produce more reliable physical properties.) Originally SED fitting was carried out by minimising χ^2 to find the model that best fits the observed photometry, however more recent codes have applied more sophisticated approaches (e.g. CIGALE, Noll et al. (2009); AGN Fitter, Calistro Rivera et al. (2016)). SED fitting has the advantage of exploring a large parameter space, considering a wide range of possible scenarios, however, it suffers from various degeneracies. For example, dust and age both redden the galaxy SED (Papovich et al., 2001) which can be a problem where dust is not well constrained. This can be addressed either by obtaining spectra or FIR photometry. Narrow spectroscopic features are not affected by changes in the continuum shape and the 4000Å break and the Balmer Hδ absorption line can be used to constrain the mean stellar age (Kauffmann et al., 2003). FIR photometry can provide a robust measure of the dust attenuation, breaking the dust-age degeneracy (Burgarella et al., 2005; Noll et al., 2009).

1.5.3 Thesis outline

In this thesis I explore the impact of environment on the evolution of galaxies by focusing on LBGs and LABs in the SSA22 protocluster at $z \sim 3$ (see Fig. 1.9). I set out below the main scientific themes, goals and results covered in each chapter.

1.5.4 Chapter 2: An enhanced merger fraction within the galaxy population of the SSA22 protocluster at $z = 3.1$

The overdense environments of protoclusters of galaxies in the early Universe ($z > 2$) are expected to accelerate the evolution of galaxies, with an increased rate of stellar mass assembly and black hole accretion compared to co-eval galaxies in the average density 'field'. These galaxies are destined to form the passive population of massive galaxies that dominate the cores of rich clusters today. While signatures of the accelerated growth of galaxies in the SSA22 protocluster ($z = 3.1$) have been observed, the mechanism driving this remains unclear. Here I show an enhanced rate of galaxy-galaxy mergers could be responsible. I morphologically classify LBGs in the SSA22 protocluster and compare these to those of galaxies in the field at $z = 3.1$ as either active mergers or non-merging using HST ACS/$F814W$ imaging, probing the rest-frame ultraviolet stellar light. I measure a merger fraction of 48 ± 10 per cent for LBGs in the protocluster compared to 30 ± 6 per cent in the field. Although the excess is marginal, an enhanced rate of mergers in SSA22 hints that galaxy-galaxy mergers are one of the key channels driving accelerated star formation and AGN growth in protocluster environments.

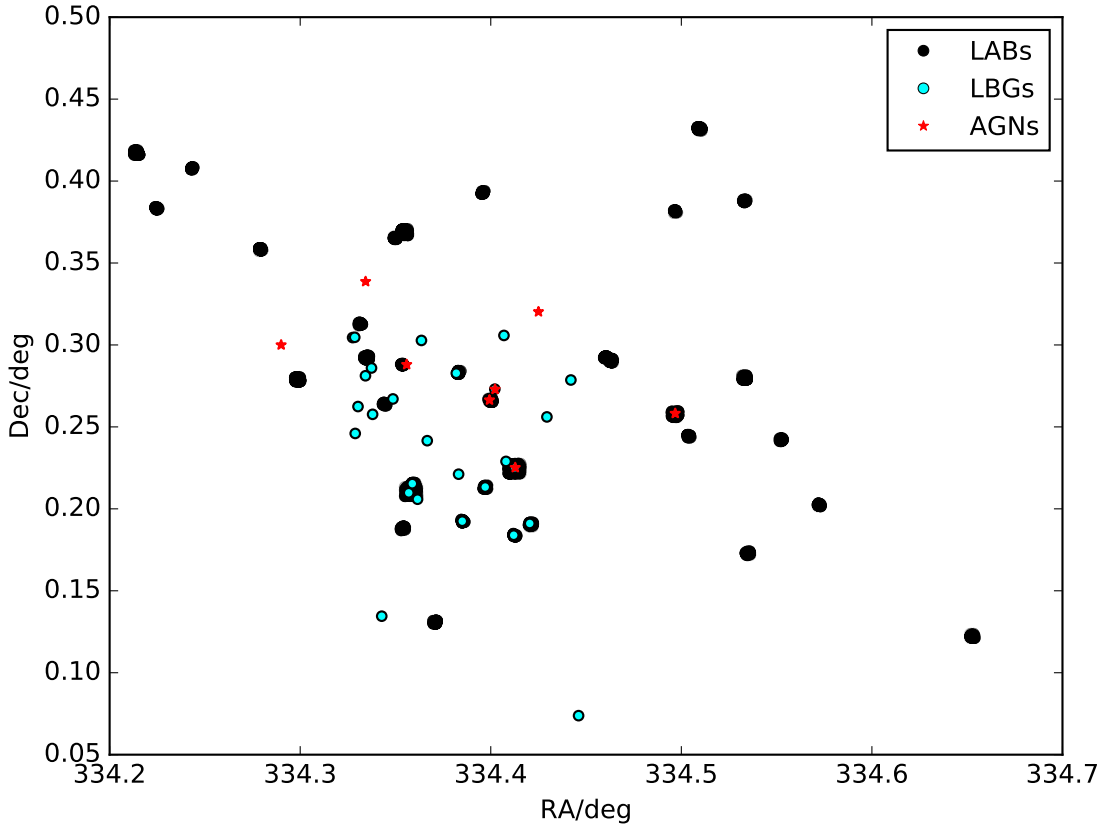

FIGURE 1.9: The distribution of the LBGs (cyan filled circles), AGN (red stars) and LABs (black blobs) in the central region of the SSA22 protocluster. The blobs give an approximate indication of size and shape, the other markers are not related to size. The LABs and LBGs shown are the focus of this thesis.

1.5.5 Chapter 3: Are Lyman-Break Galaxies more massive in dense protocluster environments?

I investigate the mass of Lyman-Break Galaxies (LBGs) in a $z \sim 3$ protocluster using multi-wavelength photometry and compare to LBGs in the field. Previous studies at $z < 2.5$ show evidence that galaxies in protoclusters are, on average, more massive than similar galaxies in the field at the same redshift, suggesting that environment has already had a significant impact on galaxy evolution at this epoch. However, it is still unclear at what stage environment starts to have a measurable impact as higher redshift studies have been inconclusive. Here I use the SED fitting code CIGALE to compare the mass of protocluster and field LBGs. I use archive images to obtain UV to MIR photometry for the protocluster LBGs and make use of an existing photometric catalogue for the HDF-N field sample. I find no statistical evidence that the protocluster LBGs are more massive than those in the field. This suggests that environment has not yet had a measurable impact on the mass of the LBG population at $z \sim 3$ and therefore differences in mass develop at lower redshift.

1.5.6 Chapter 4: The average submillimetre properties of Lyman-α Blobs at $z = 3$

LABs offer insight into the complex interface between galaxies and their circumgalactic medium. Whilst some LABs have been found to contain luminous star-forming galaxies and active galactic nuclei that could potentially power the Lyα emission, others appear not to be associated with obvious luminous galaxy counterparts. It has been speculated that LABs may be powered by cold gas streaming on to a central galaxy, providing an opportunity to directly observe the 'cold accretion' mode of galaxy growth. Star-forming galaxies in LABs could be dust obscured and therefore detectable only at longer wavelengths. I stack deep SCUBA-2 observations of the SSA22 field to determine the average 850μm flux density of 34 LABs. I measure $S_{850} = 0.6\pm0.2$mJy for all LABs, but stacking the LABs by size indicates that only the largest third (area $\geq$ 1794 kpc^2) have a mean detection, at 4.5σ, with $S_{850} = 1.4\pm0.3$mJy. Only two LABs (1 and 18) have individual SCUBA-2 $>3.5\sigma$ detections at a depth of 1.1mJy beam^{-1}. I consider two possible mechanisms for powering the LABs and find that central star formation is likely to dominate the emission of Lyα, with cold accretion playing a secondary role.

1.5.7 Chapter 5: Further discussion and conclusions

In the final chapter I summarise the results of my thesis, review progress made since completing our work in Chapters 2 to 4, and look ahead to potential future research.

Chapter 2

An enhanced merger fraction within the galaxy population of the SSA22 protocluster at $z = 3.1$

The work in this chapter has previously been published as Hine et al., 2016, *Monthly Notices of the Royal Astronomical Society*, 460, 4075.

2.1 Introduction

In the next two chapters of this thesis I address the question of whether galaxy evolution is accelerated in dense environments. I look first at galaxy mergers which naturally increase average galaxy mass by combining the existing stellar populations and can also trigger starbursts through the collapse of molecular clouds. I test the hypothesis that the merger fraction in protocluster environments is higher than that in the average density field and therefore potentially responsible for accelerated growth in these environments.

I compare the merger fraction of Lyman-break galaxies in the SSA22 protocluster at $z \sim 3$ with that in *Hubble* Deep Field North (HDF-N), considered to be a region of average density. My classification of these galaxies as mergers or non mergers is based on their morphology (using *HST* imaging) and captures a particular stage in the merger cycle. I also consider the use of two other methods of classification, close pairs and CAS parameters.

2.2 Datasets

2.2.1 Lyman-Break Galaxy sample selection

My sample is taken from the Steidel et al. (2003) LBG redshift survey using the Palomar 5.08-m telescope. The LBGs span a magnitude range of $19.0 \leq R_{AB} \leq 25.5$ mag, and spectroscopic redshifts have been obtained using the Low Resolution Imaging Spectrometer (LRIS), on Keck (Oke et al., 1995). I identify LBGs at $z = 3.06$ – 3.12 as members of the protocluster (Lehmer et al., 2009); as this is not a virialized structure, the concept of 'membership' is not well defined. For the average density field control sample I select LBGs in the HDF-N field in the range $2.5 \leq z \leq 3.5$. To expand my control sample I also classified the SSA22 LBGs at $2.5 \leq z \leq 3.5$, but excluding the $3.06 \leq z \leq 3.12$ interval, as 'field' galaxies not associated with the protocluster. The redshift distribution of both samples is shown in Fig. 2.1.

I tested the similarity of the two LBG samples using IRAC 4.5μm magnitudes ([4.5]) as a proxy for stellar mass. At $z = 3.1$ MIR bands trace the lower mass stars which make up most of the baryonic mass in galaxies. Where available I obtained IRAC data for the HDF-N sample from Ashby et al. (2013) and for the SSA22 sample from the *Spitzer* archive (originally from GO project 30328). Applying the Kolmogorov–Smirnov (K-S) test gave a p-value of 0.97 for [4.5] < 24, (where both catalogues are approximately complete), confirming that the two samples have a statistically identical stellar mass distribution.

2.2.2 *HST* observations

I obtained archival *Hubble Space Telescope* (*HST*) images for the LBGs using the Mikulski Archive for Space Telescopes (MAST)[1]. All images were acquired using the Advanced Camera for Surveys (ACS) and the *F*814*W* filter. I was able to obtain images for 23 of the 27 LBGs in the protocluster and 33 of the 55 LBGs in the SSA22 field sample given the sparse sampling strategy of the *HST* projects. There was full coverage of the HDF-N field LBGs. Exposure times for individual protocluster images varied from 2–7.3ks (with some combined to give total exposures of up to 11ks) and exposure times for the field samples were restricted to a similar range. The potential impact of the range of exposure times used is discussed further in Section 2.3.4.

[1] `http://archive.stsci.edu/`. Proposal numbers 9760, 10405, 11636, 12527, 12442, 12443, 12444, 12445, 13063 and 13420.

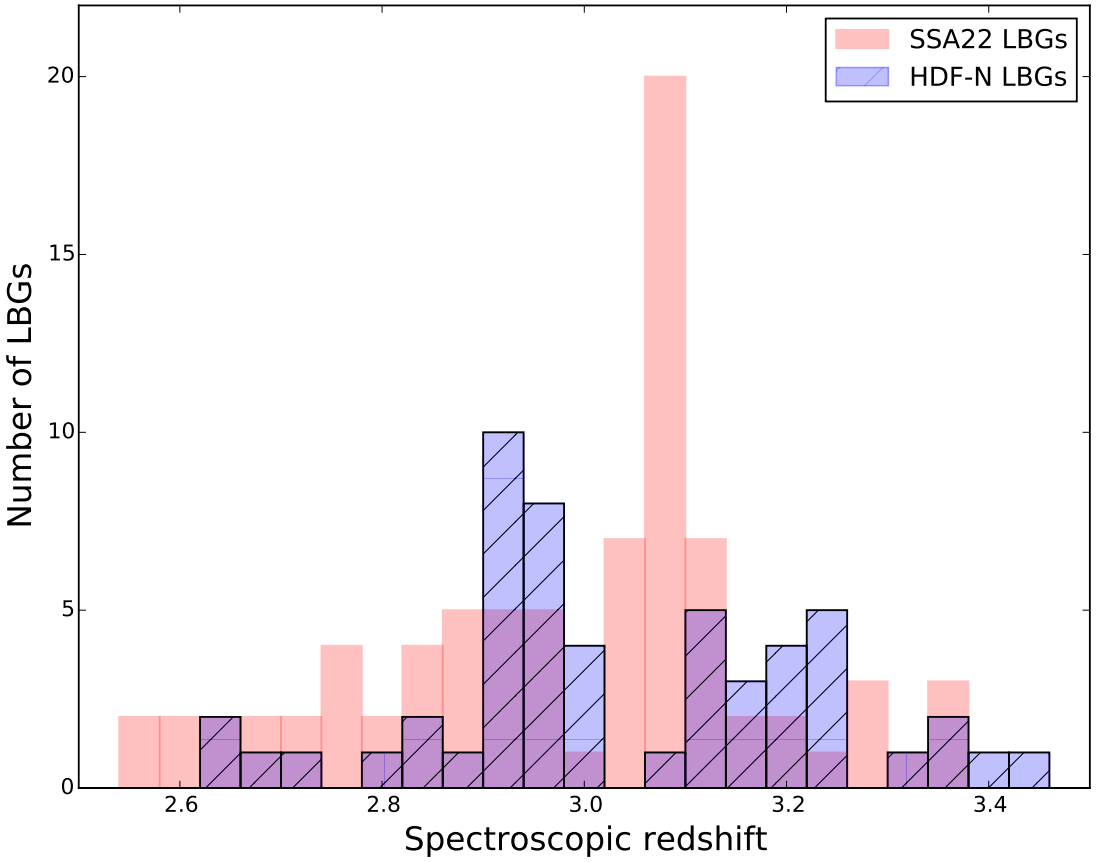

FIGURE 2.1: The redshift distribution of LBGs in SSA22 and HDF-N fields, the protocluster lies at $z = 3.09$. Redshifts were obtained from the Steidel et al. (2003) catalogues.

2.3 Analysis

2.3.1 Classification

I generated 4 arcsec $\times$ 4 arcsec ($\approx$ 30 kpc projected) thumbnail images centred on the coordinates of each LBG where image data of suitable quality was available (e.g. not on an edge). For the classification, I scaled each of these images to produce three versions, containing (a) all flux between $\sim$1 and 15 per cent of the peak flux value (faint scale); (b) all flux between $\sim$15 and 50 per cent of the peak flux value (medium scale) and (c) all flux between $\sim$55 and 80 per cent of the peak flux value (bright scale). I selected these flux ranges to facilitate the visual identification of different structures associated with mergers, such as faint tidal features, coalescing nodes, and so on.

I used the scaled thumbnails for my initial classification, but I also examined the full dynamic range of each image to aid my classification. All targets were classified at least three times, including once by an independent reviewer (see Section 2.3.3), with additional reviews carried

out for those where the classification was ambiguous. I also carried out a 'blind' test (see Section 2.3.3) to eliminate potential unconscious bias. I define six classification categories:

C1 Compact, isolated system, single nucleus.

C2 Compact but with minor asymmetry and no clear evidence of a second nucleus.

M1 Evidence of two nuclei within 1 arcsec diameter aperture ($\sim$8kpc in projection) centred on the brightest part of the LBG. All flux falling within the aperture.

M2 Evidence of two nuclei within the 1 arcsec aperture, but with some flux falling outside.

M3 Evidence of $>$2 nuclei or complex clumpy structure falling within the aperture, but with some flux falling outside.

M4 Evidence of $>$2 nuclei or complex clumpy structure with all flux falling inside the 1 arcsec diameter aperture.

Those classified as 'C' are non mergers, whilst those classified as 'M' are mergers. A small number of targets could have been classified as C2 or a merger. Where there was doubt I conservatively classified as C2, requiring a clear secondary concentration of bright flux (thought to be a nucleus) to classify as a merger. A small number of thumbnails included a near neighbour outside the aperture which could possibly have been interacting with the target LBG in an early stage merger. I did not classify these as a merger unless there was evidence of diffuse emission reminiscent of stellar tidal trails between the two galaxies. The observed morphology could also have been effected by the impact of dust on the UV emission, this is discussed further in Section 3.6. Thumbnails of the protocluster LBGs and their classifications are presented in Fig. 2.2. The images include contours representing the 15, 55 and 80 per cent scaling boundaries used in my analysis, which give a good indication of my classification in most cases.

2.3.2 Merger fractions and merger rates

Merger rates, as defined in the literature, are difficult to calculate; they require time-scales which are generally obtained from simulations (although see Conselice, 2009). For example Lotz et al. (2011) defined the merger rate as:

$$\Gamma_{\rm m} = \frac{f_{\rm gm} \times n_{\rm gal}}{T_{\rm obs}} \tag{2.1}$$

where $f_{\rm gm}$ is the galaxy merger fraction, $n_{\rm gal}$ is the comoving number density of galaxies and $T_{\rm obs}$ is the average observability time-scale. However, *merger fractions* are relatively easy to

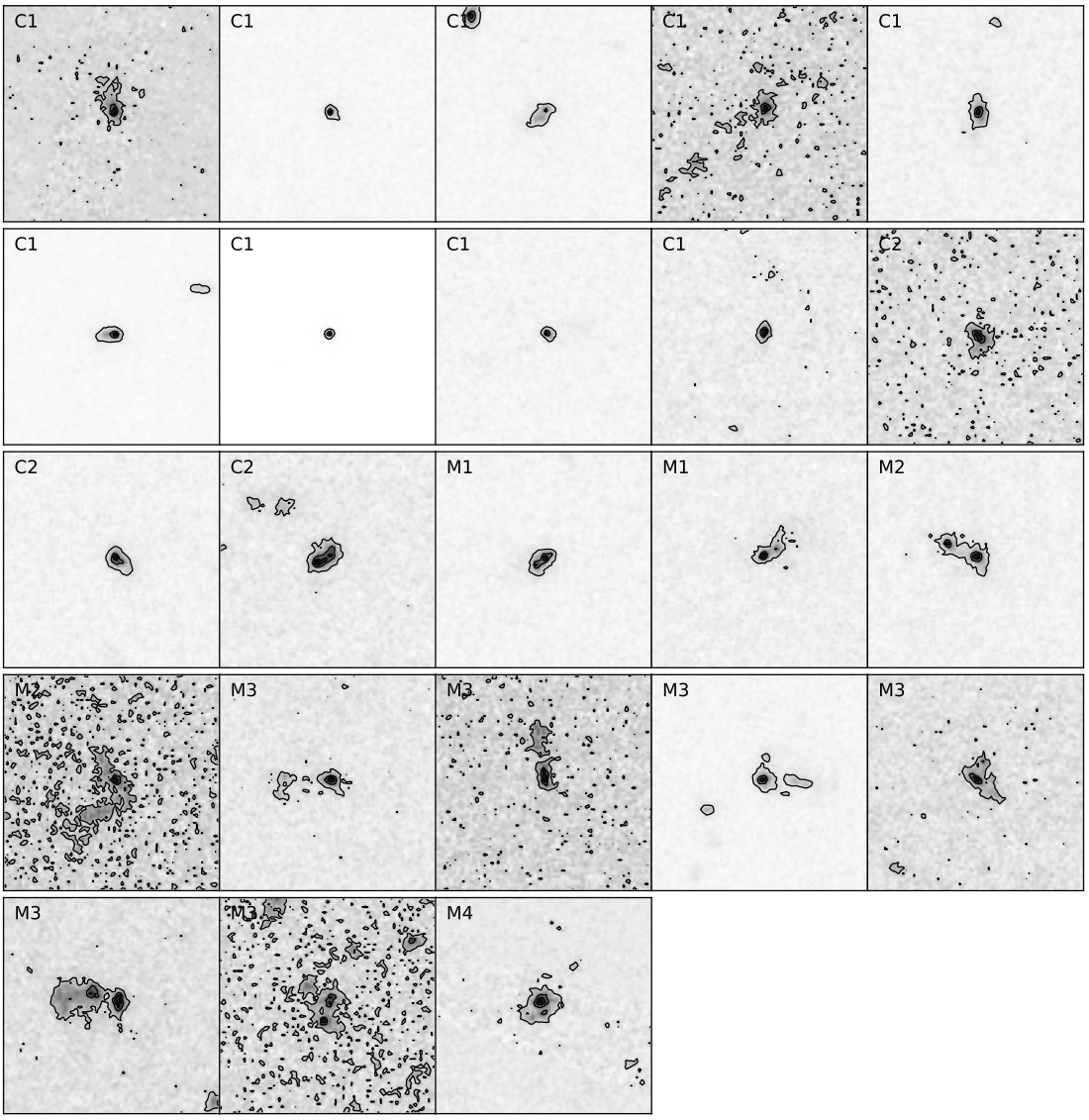

FIGURE 2.2: 4 arcsec $\times$ 4 arcsec (approximately 30 kpc projected) thumbnail ACS $F814W$ images of the protocluster LBGs grouped and labelled by classification. The contours are at the 15, 55 and 80 per cent levels used in my analysis.

measure as they are a simple expression of the instantaneous number of mergers observed in a population and so do not require a time-scale. Two merger fractions are used in the literature (Conselice et al., 2008; Lotz et al., 2011; Stott et al., 2013), the most common and the one used in this work is simply:

$$f_{\rm m} = \frac{N_{\rm m}}{N_{\rm t}} \tag{2.2}$$

where $N_{\rm m}$ is the number of observed mergers in a sample and $N_{\rm t}$ is the total number of galaxies. The second is $f_{\rm gm}$ (the galaxy merger fraction) which is based on the number of galaxies undergoing mergers rather than the number of merging events. In the simple case of two galaxies

TABLE 2.1: Morphological classification and merger fractions for LBGs selected in the protocluster and field environments. Uncertainties on the merger fraction are derived from binomial statistics.

Field	C1	C2	Total non-mergers	M1	M2	M3	M4	Total mergers	Sample size total	Merger fraction
SSA22 Protocluster	9	3	12	2	2	6	1	11	23	0.48±0.10
SSA22 Field	17	5	22	3	2	5	1	11	33	0.33±0.08
HDF-N Field	26	11	37	4	7	5	0	16	53	0.30±0.06
Combined field	43	16	59	7	9	10	1	27	86	0.31±0.05

merging $f_{\rm gm} = 2f_{\rm m}$.

Comparing merger fractions from different studies is problematic as they are highly dependent on the method used to identify mergers, which is often subjective. In my work I use the same classification method for the protocluster and field samples and therefore the fractions should be comparable across the different environments. I calculate merger fractions based on my classification scheme described above. It is important to note that my scheme detects mergers at a specific phase of the merger sequence in all fields, when the two nuclei are very close, but have not yet coalesced.

My classification results are presented in Table 2.1 and Figs 2.3 and 2.4. I measure a merger fraction of 48±10 per cent for the protocluster, 33±8 per cent for the SSA22 field and 30±6 per cent for the HDF-N field, assuming binomial statistics to estimate the uncertainties (Berendsen, 2011). Combining the two field samples by simply adding the number of galaxies classified as mergers or non-mergers gives a result of 31±5 per cent. Based on these statistics I estimate a probability of ∼7 per cent for finding 11 or more mergers in the protocluster sample if the actual merger fraction is 31 per cent (as in the combined field).

2.3.3 Blind and Independent Testing

To check for unconscious bias in my classification process I generated random IDs for all my scaled images and reclassified them without knowing their provenance (i.e. protocluster or field). 95 per cent of my classifications were unchanged under blind classification. The classification changed for five galaxies: three changing from mergers to non mergers and two from non-mergers to mergers. Due to the small number of galaxies in the protocluster sample, the two protocluster galaxies that changed from mergers to non-mergers do have a small but not significant impact on the merger fraction, which becomes 39±10 per cent. However, these two galaxies were also classified as non-mergers during my initial review of the scaled images and it was only during my more detailed examination that I identified the features that led to their final classification as mergers. The blind testing does not identify any systematic bias in my classifications.

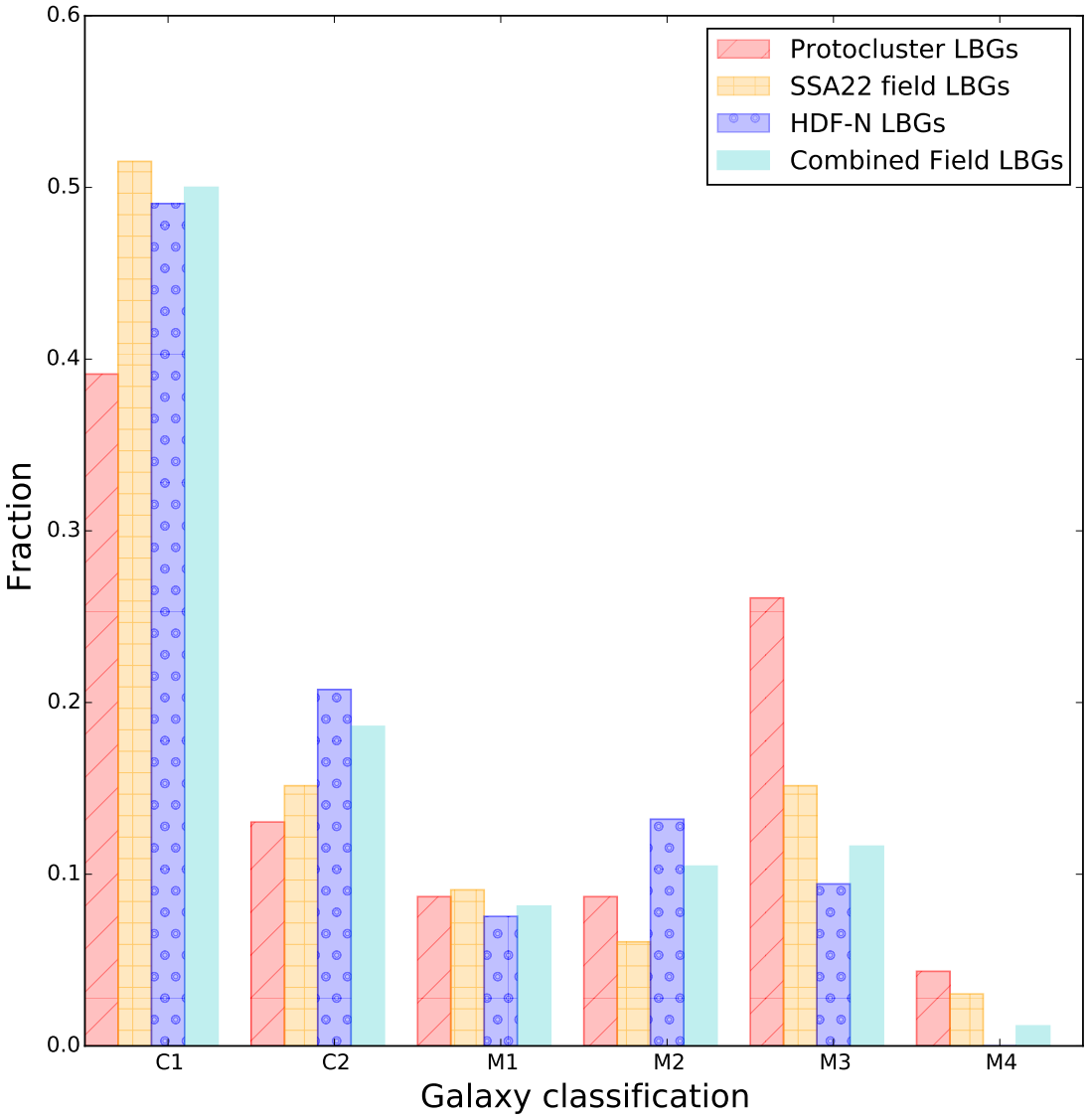

FIGURE 2.3: Fraction of galaxies of each type for the protocluster and average field samples.

An additional independent merger analysis was carried out by a student who was not a member of the group. The independent analysis indicated a protocluster merger fraction of 43±10 per cent and a combined field merger fraction of 22±4 per cent. Both values are lower than the original results, but the independent analysis still indicates a marginally higher merger fraction in the protocluster, with only a 2 per cent probability of obtaining these results if the merger fractions were actually the same.

2.3.4 Chance alignments and image depth

It is possible that when a second source falls within the 0.5 arcsec radius aperture used to categorise the LBGs, this source is not an interacting galaxy, but simply a chance alignment of physically disassociated galaxies along the line of sight. I investigated this possibility using the

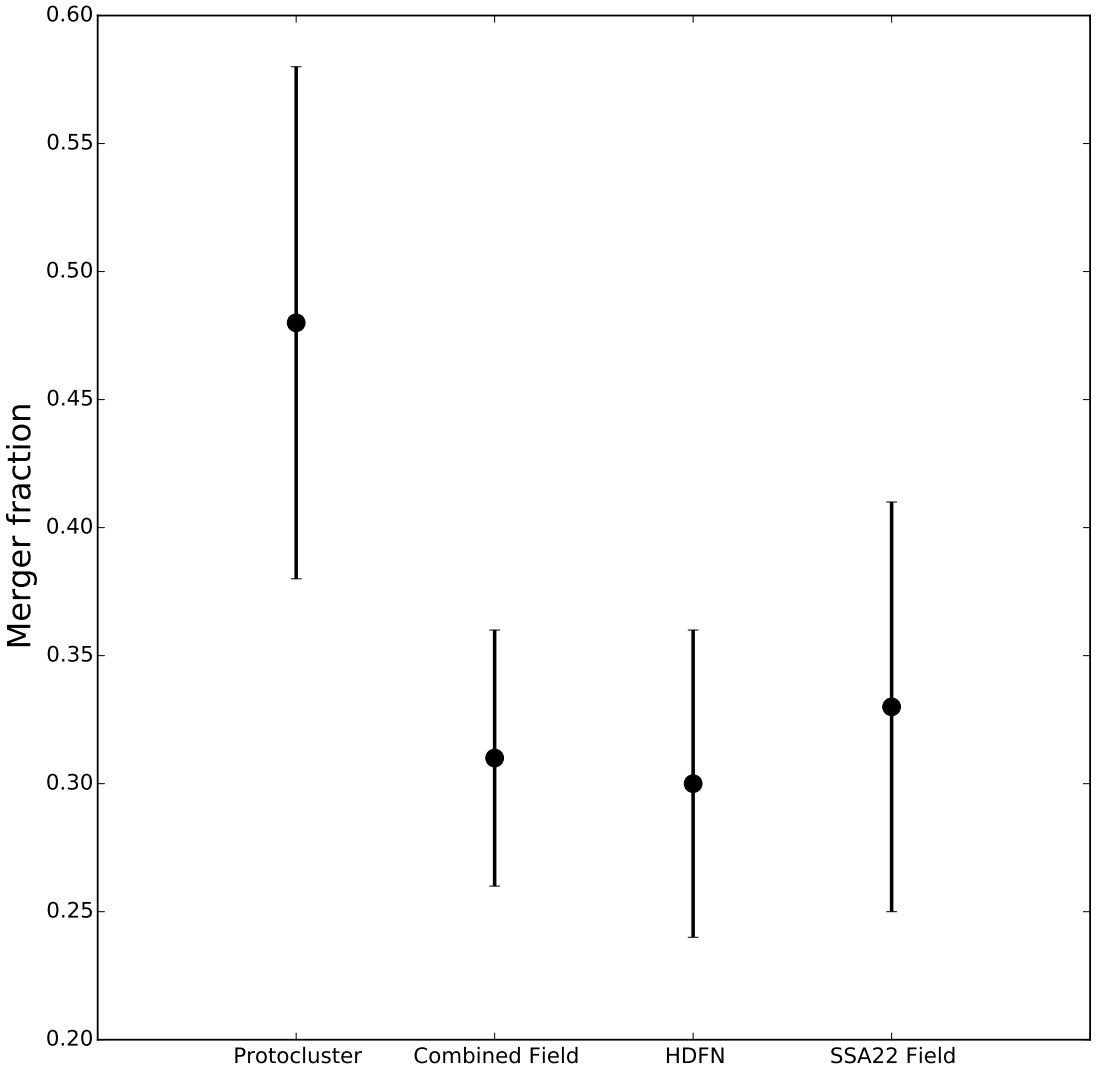

FIGURE 2.4: Merger fractions for my individual samples and the combined field population based on observed morphology.

following procedure. First, I evaluated the median LBG flux within a 0.5 arcsec radius aperture. I then randomly selected 10^4 pixels in each of the full frame images, each time evaluating the total flux within 0.5 arcsec of that pixel. This procedure allows me to estimate the surface density of objects of similar (or greater) flux to the target LBGs, and thus a means of evaluating the likelihood of chance alignments. The results show that for each LBG, there is only $\sim$1 per cent probability that an object of similar flux would be detected within 0.5 arcsec (i.e. mimicking a merger).

My analysis involved the use of a range of images with different exposure times. It is possible that this could also lead to bias in my results, in particular in identifying faint tidal emission that might only become apparent in deeper images. For the SSA22 sample the exposure times of images used range from 2.2–11 ks, and for HDF-N from 1.2–8.9 ks. There were no mergers

identified in the $\sim$ 2ks images, but as there were only two thumbnails in this group, this is unlikely to be significant. The merger fraction for all LBGs in the SSA22 field and protocluster combined was 39 per cent, but when split by exposure times the merger fractions varied between 44 per cent and 33 per cent (ignoring the $\sim$2ks group) showing a slight fall with increasing exposure time. The HDF-N images show a stronger bias, but in the opposite direction. I measured a merger fraction of 26 per cent for shorter exposures ($<$ 3ks) and 39 per cent for longer exposures ($>$ 8ks).

I also compared the percentage of mergers in each exposure time band with the percentage of thumbnails using that exposure time. This indicates a slight enhancement in the SSA22 merger fraction in long exposures, but it is not significant enough to affect my conclusions. For HDF-N I found that 34 per cent of the mergers were in the longer exposures which make up 44 per cent of all thumbnails, giving lower than expected occurrence in long exposures. Thus there was no consistent bias.

All the mergers initially identified using long-exposure images would also have been identified as mergers if I had used the available short-exposure images. All but two of the compact classifications identified in the long-exposures would also have been identified as compacts using short exposures, and two might have been misidentified as mergers due to noise that appeared to link two separate objects. These tests give me confidence that my classification scheme is not strongly dependent on the depth of the image.

2.3.5 Comparison to CAS and Close Pairs

I measured 'CAS' (concentration, asymmetry, smoothness/clumpiness) parameters (Conselice et al., 2008) for my LBGs with a view to determining CAS-based merger fractions for comparison. However, these were not able to distinguish between the merging and non-merging systems in my sample (C. Conselice, private communication). The A parameter is considered to be the most effective for measuring mergers ($A > 0.35$ indicates a merger, Conselice et al., 2008). This definition gives a merger fraction of 22 per cent for the protocluster and 4 per cent for the HDF-N field (the distribution of A values is shown in Fig. 2.5). This does indicate an enhanced merger fraction in the protocluster, but is clearly only identifying a small number of the mergers in my classification (seven in total). This is perhaps not surprising given the limited resolution and relatively low signal to noise of the images at $z \approx 3$ (a signal to noise of 20 is required, C. Conselice, private communication) as well as the fact that my definition of a merger is based on the presence of two unmerged nuclei rather than disturbed morphology.

I carried out a close-pairs analysis, using a separation of 20kpc. This resulted in a merger fraction of 52$\pm$10 per cent. in the protocluster and 38$\pm$5 per cent in the combined field. The larger aperture leads to an increased probability of chance alignment of $\sim$3 per cent. The probability

of the merger fraction in the protocluster being the same as that in the field based on these results increases to 12 per cent. Overall I consider these results to be less reliable due to the increased chance of a low-redshift interloper.

Studies of massive galaxies at slightly lower redshift ranges ($2.3 < z < 3.0$) have found field merger fractions based on close-pair analysis (at 30kpc) of 40 ± 10 per cent (Bluck et al., 2009) and 12 ± 15 per cent (Man et al., 2012). The large uncertainties mean that these findings are consistent with each other and with my results for my field samples. A similar study using CAS parameters indicated a field merger fraction of 27 ± 8 per cent (Bluck et al., 2012), which is also consistent with my results and with earlier work suggesting a peak in the field merger fraction of $\sim$30 per cent at z=3 (Conselice and Arnold, 2009).

These studies involved rest-frame optical observations, whereas my data are rest-frame UV. Taylor-Mager et al. (2007) investigated the impact of using different rest-frame wavelengths to classify galaxies using the CAS parameters and found that using UV data led to higher values for A. Taylor-Mager et al. (2007) found that nearby late-type galaxies (including mergers) were less concentrated, more asymmetric, and more clumpy when observed at UV wavelengths compared to optical observations. They suggest that an adjustment needs to be made to the CAS parameters when applying them to UV observations. Conselice et al. (2008) also found a fractional change in the A parameters when observed in UV rather than optical light of $\frac{\Delta A}{\Delta \lambda} = -0.83 \pm 1.06$ at $z = 0.75 - 1.25$. Given the low number of mergers identified in Section 2.3.5 it seems unlikely that the A parameter is identifying too many mergers, as this lower redshift work would predict. Huertas-Company et al. (2014) found there was generally good correlation between morphological type for UV and optical observations up to $z = 3$. They used a Support Vector Machine with seven parameters (including CAS) to determine the probability of a particular galaxy type and found a relationship of $p^{uv}_{\rm irregular} = (0.7 \pm 0.02) \times p^{\rm optical}_{\rm irregular} + (0.13 \pm 0.01)$. This suggests that wavelength may not have as large an impact as had previously been thought.

2.4 Interpretation and discussion

My classification method is designed to be sensitive to *ongoing* mergers at a specific stage in the merger sequence; very late stage mergers (close to coalescence) or very early (widely separated) interactions are counted as 'non-mergers'. The experiment was intended to be conservative such that I only distinguish between galaxies that are clearly comprised of two or more compact nuclei separated by several kiloparsecs, or isolated systems. Importantly, however, the same methodology was applied to the protocluster members and the field. My results indicate a marginal enhancement of the number of on-going mergers in the protocluster environment at $z \approx 3$. Aside from the possibility that this enhancement merely reflects a statistical fluctuation (described in Section 2.3) there are three possible physical explanations for this:

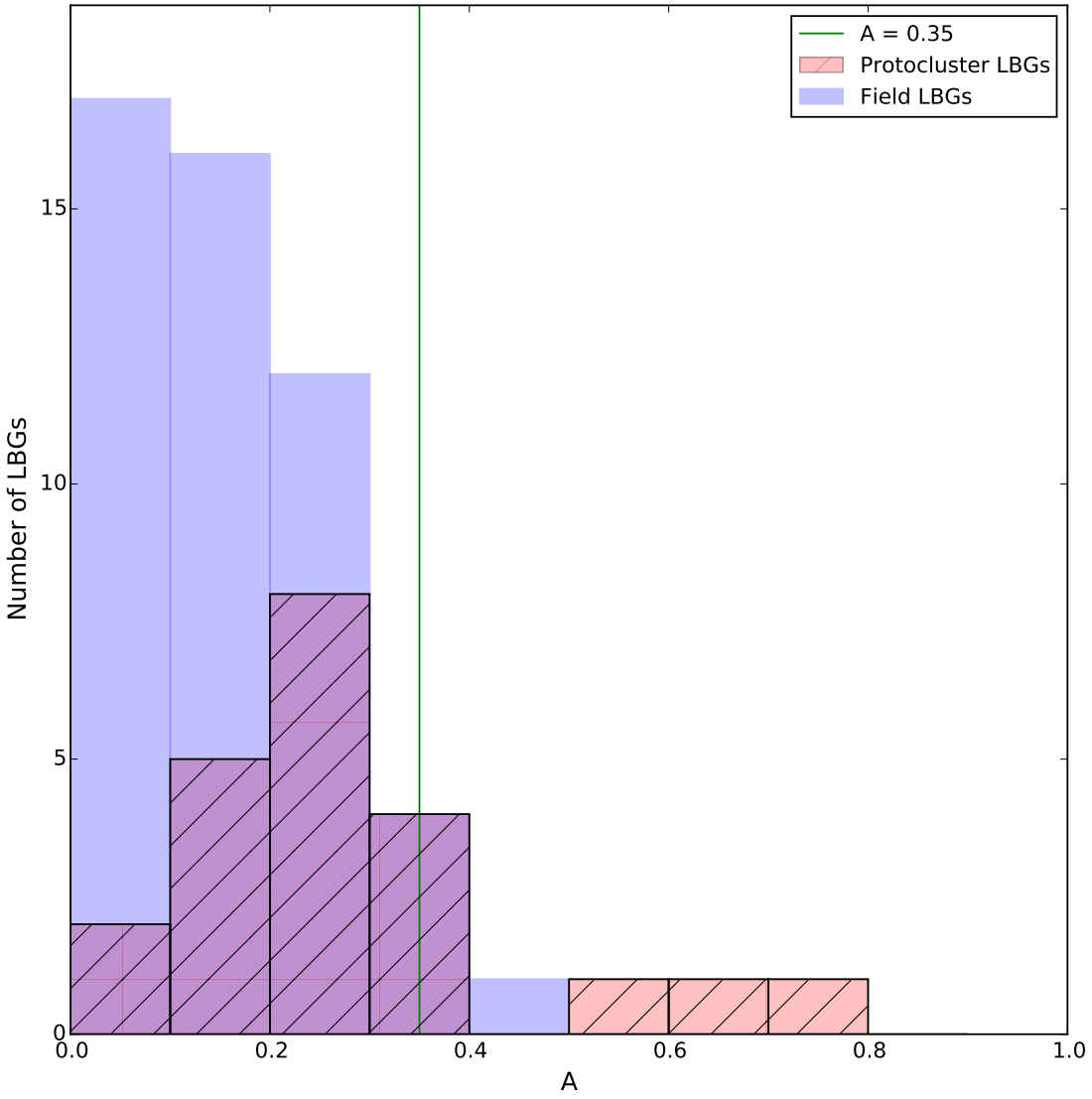

FIGURE 2.5: The A parameter values for the SSA22 protocluster and HDF-N field LBGs. The vertical line indicates the Conselice et al. (2008) classification of a merger. Using this classification only 7 LBGs in total were identified as mergers.

1. *Higher merger rate.* This implies that either more galaxies are undergoing mergers at any one time in the protocluster compared to the field, or that there is a mis-match between the formation epoch of the protocluster and field LBGs.

2. *Multiple mergers.* A higher merger rate could also be due to individual galaxies undergoing multiple mergers, rather than more galaxies undergoing mergers at the same time. I have assumed that each LBG undergoes only one major merger.

3. *A longer duty cycle.* Integrated over time, the merger rate may be the same in the protocluster as in the field, but the protocluster galaxies may take longer to merge compared to their field counterparts, increasing their visibility.

The duty cycle of a merger is thought to be dependent on local factors such as galaxy mass (affecting the dynamics of the merger) and gas fraction (Hopkins et al., 2006; Lotz et al., 2008). Under normal conditions, the rate of star formation scales with gas fraction, so provided dust-obscuration is not extreme, gas-rich galaxies undergoing mergers might be detectable optically for longer (e.g. through stellar streams, bright cores) than gas-poor galaxies. CO surveys of protocluster and identically-selected field galaxies would allow one to compare the gas mass fractions of these two populations. Protocluster galaxies might be expected to have higher gas fractions due to efficient supply of pristine intergalactic gas through filamentary accretion, but this is a picture yet to be empirically tested. Lyα blobs are generally found in high-z protoclusters and indicate the presence of large volumes of cold gas around forming galaxies.

Fakhouri and Ma (2009) examined the role of environment on the halo merger rate in *N*-body simulations, using the friend-of-friends group finder (Davis et al., 1985) within the millennium simulation (Springel et al., 2005) to trace the merger histories of dark matter sub-haloes out to $z = 2$. A key finding was a correlation between environment and merger rate, such that sub-haloes in the densest environments underwent merger rates 2–2.5 times higher than those in the lowest density regions. With the caveat that galaxies are biased tracers of the matter field, it is reasonable to assume that there will be a similar trend for the galaxies themselves. It is interesting that the level of enhancement of the merger rate found by Fakhouri and Ma (2009) in the simulations is broadly in agreement with the enhancement I find for SSA22.

My analysis traces the rest-frame ultraviolet emission which is very sensitive to dust obscuration; for example, extended/clumpy star-forming regions could be hidden and the merger fraction understated, or a clumpy dust distribution could lead to very high extinction to certain stellar populations, giving the stellar emission overall a clumpy morphology, that could possibly be misinterpreted as a merger.

I do not expect the use of rest-frame UV observations to lead to a significant bias in my interpretation unless there is a significant difference between the obscuration properties of galaxies in the protocluster and the field, since I have applied an identical analysis to both. Nevertheless, I have applied to obtain near-infrared *HST*-WFC3 observations that will allow me to repeat my analysis based on the morphology of the rest-frame optical flux. Similarly, I am part of a collaboration to obtain ALMA time to obtain follow-up observations of LBGs along the 'merger sequence' in SSA22. This will allow me to directly detect the thermal emission from cold dust responsible for extinction in the ultraviolet/optical light.

My result is marginal mainly due to small number statistics, which dominate the size of the uncertainties on my merger fractions. This arises from the lack of a complete LBG catalogue covering the whole SSA22 field and sparse *HST* coverage of SSA22. It would be useful to extend my analysis to additional protoclusters and fields at a similar redshift to overcome the potential issues of small number statistics and cosmic variance, but high-z protoclusters are extremely

rare, and generally lack the ancillary data that SSA22 has. Moreover, it is important to note that the morphological classification approach I have presented here *must* be applied to identically selected galaxy populations in order to control for the influence of galaxy properties (chiefly mass) when investigating the influence of large-scale environmental effects in this way. Again, this is not possible for the majority of known $z > 2$ protoclusters.

Currently, the only other LBG catalogue in Steidel et al. (2003) with *HST F*814*W* coverage is the Westphal field. The *HST* data available here are generally shallower than those available for SSA22 and HDF-N and I have therefore not included them in my main analysis. However, I have classified the LBGs in this field where possible, following the same procedure as described above. I measure a merger fraction of 30 ± 5 per cent (26 mergers out of 88 LBGs for which images of reasonable quality were available). This is consistent with my main results for the HDF-N and SSA22 field samples and, if included, would result in a combined average field merger fraction of 30 ± 3 per cent. In order to solidify my result further I would need to significantly improve the spectroscopic completion of the protocluster membership to at least $\sim$70 (LBG) members for a 3σ measurement.

2.5 Summary

I have detected a marginal enhancement of the merger fraction of LBGs in the SSA22 protocluster at $z = 3.1$, with approximately 60 per cent more LBGs actively undergoing mergers in the protocluster compared to the average density field at the same epoch, consistent with large-scale simulations. This hints that mergers could have an important role in driving accelerated galaxy growth in the rare, dense environments destined to become the massive clusters of the present epoch, by triggering and driving star formation and black hole growth.

Chapter 3

Are Lyman-Break Galaxies more massive in dense protocluster environments?

3.1 Introduction

As described in Chapter 1, environment is thought to have an impact on galaxy evolution, accelerating the progression from star-forming to massive, passive galaxies, but it is unclear when signs of this differentiation first appear. Earlier studies have detected indications of enhanced mass in protoclusters at $z \sim 2$ (Steidel et al., 2005; Hatch et al., 2011; Koyama et al., 2013; Cooke et al., 2014), but there has been no detection of a difference in mass at redshifts >3.5 (Overzier et al., 2008, 2009). This suggests that something interesting may be happening at $z \sim 3$ where results are inconsistent (Lehmer et al., 2009; Kuiper et al., 2010; Lemaux et al., 2014; Cucciati et al., 2014; Alexander et al., 2016). The SSA22 protocluster, lying as it does at $z = 3.1$, is therefore an ideal target to use to investigate this subject further.

In this chapter, I address this question by measuring the mass of a sample of SSA22 protocluster LBGs and field LBGs and searching for any statistical evidence of mass enhancement. I do this using multiwavelength data and the SED fitting code CIGALE. I consider first an average LBG for each sample (based on average photometry) and then the individual LBGs in each population. I also combine these results with those from Chapter 2 and the literature to provide a summary of the known SSA22 protocluster LBG properties.

3.2 Sample Selection

3.2.1 SSA22 Sample

My sample of protocluster LBGs was taken from the Steidel et al. (2003) LBG redshift survey using the Palomar 5.08m telescope. The LBGs span a magnitude range of $19.0 \leq R_{AB} \leq 25.5$ mag and spectroscopic redshifts were obtained using the Low Resolution Imaging Spectrometer (LRIS) on Keck (Oke et al., 1995). As in previous studies I identify LBGs at $z = 3.06$ – 3.12 as members of the protocluster (Lehmer et al., 2009; Hine et al., 2016). I select all LBGs within this redshift range, but exclude those identified as AGN either by x-ray detection (Lehmer et al., 2009) or using IRAC colours (Stern et al., 2005), giving a sample of 26.

3.2.2 HDFN Sample

My sample of field LBGs was also selected from the Steidel et al. (2003) survey to ensure that they are comparable to the protocluster LBGs (i.e. selected according to identical criteria). As in my previous work on LBG merger fractions (Chapter 2 and Hine et al., 2016) I restricted my field sample to $2.5 \leq z \leq 3.5$. This is a wide enough redshift range to ensure a reasonable sample size, but narrow enough to avoid biasing my results with potential redshift evolution effects. I identified 52 LBGs within this redshift range.

3.3 Data and Photometry

3.3.1 SSA22 Sample

The SSA22 photometry used in my work is summarised in Table 3.1. UV and optical photometry (U_n, G, R) was obtained from the Steidel et al. (2003) SSA22 catalogue. J and K band photometry was obtained by combing data from the United Kingdom Infrared Telescope (UKIRT) Infrared Deep Sky Survey (UKIDSS, Lawrence et al., 2007) and the VISTA-CFHT Stripe 82 Survey (VICS82, Geach et al. 2017 in prep). I obtained archival *Hubble Space Telescope* (*HST*) images for the LBGs using the Mikulski Archive for Space Telescopes (MAST)[1]. Proposal numbers 9760, 10405, 11636, 12527, 12442, 12443, 12444, 12445, 13063 and 13420 for $F814W$ imaging using Advanced Camera for Surveys (ACS) and proposal numbers 11735, 13844 and 11636 for $F160W$ imaging using The Wide Field Camera 3 (WFC3). I obtained *Spitzer Space Telescope* (*Spitzer*) IRAC observations of the SSA22 protocluster from the Infrared Science Archive (IRSA). The observations used were from GTO 64 and 30328. PID

[1] `http://archive.stsci.edu/`

TABLE 3.1: SSA22 photometry used in my SED fitting. A source reference is given where all data is taken from the same survey. Details of the *HST* and *Spitzer* programmes are given in the text.

	Effective wavelength (μm)	Reference
U_n, G, R	0.355, 0.478, 0.683	Palomar, Steidel et al. (2003)
*F*814*W*, *F*160*W*	0.814, 1.600	*HST*: ACS, WFC3
J, K	1.248, 2.201	UKIDSS, Lawrence et al. (2007)
		VICS82, (Geach et al. 2017 in prep)
IRAC1, IRAC2, IRAC3, IRAC4	3.600, 4.500, 5.800, 8.000	*Spitzer Space Telescope*

64 is a single pointing consisting of a $\sim 5' \times 5'$ area observed with IRAC (AORID 4397824) with an integration time of 6400s pixel^{-1}. PID 30328 covered an area of $\sim$ 375 arcmin^2 using IRAC (AORIDs 17599488, 17599744, 17600000, 17600256, 17600512) with integration times of $3000 - 7500$s pixel^{-1}. This included a 225 arcmin^2 region covered by all four IRAC wavelengths (3.6μm, 4.5μm, 5.8μm and 8μm) to a uniform depth of 7500s pixel^{-1}.

NIR photometry was measured using a 2-arcsec diameter aperture. Uncertainties were calculated as the standard deviation of background noise in 2-arcsec apertures. I used the publicly available tool T-PHOT (Merlin et al., 2015) to measure IRAC photometry using a high resolution (*HST*) image as a prior. Full details of this approach are given in (Merlin et al., 2015).

Not all protocluster LBGs were covered in all 12 wavebands. In particular *HST* coverage was limited, however all LBGs were covered by at least one *HST* band. IRAC photometry was only used when the TPHOT values were considered reliable. TPHOT generates a residual map by subtracting the actual low-resolution (IRAC) map from a mock low-resolution map generated using the high-resolution prior and a kernel (the kernel is produced by convolving the high-resolution point spread function (PSF) and the low-resolution PSF). Any sources lying in regions containing large residuals were excluded, as this suggests that the mock map (which is used to produce the photometry) is not a good fit to the data.

3.3.2 HDFN Sample

I obtained photometry for the HDFN LBGs from the 3D-HST WFC3-selected Photometric Catalog described fully in Skelton et al. (2014). This provides photometry for 22 wavebands from 0.3 to 8μm. I only included photometry flagged as usable and I omitted AGN (identified by x-ray detection or IRAC colours as for the SSA22 LBGs), resulting in a sample of 49 LBGs.

TABLE 3.2: Models and parameter ranges used for SED fitting (further details are given in the text)

Options	Chabrier	Salpeter	M2005	C12
Stellar templates	BC03	BC03	M05	BC03
tau main	3, 7, 10	as for Chabrier	as for Chabrier	7
tau burst	0.05, 1, 5, 10	as for Chabrier	as for Chabrier	as for Chabrier
burst fractions	0.05, 0.1, 0.2, 0.3, 0.4, 0.5, 0.6, 0.7, 0.8	as for Chabrier	as for Chabrier	0.1 to 0.9 (in steps of 0.1)
Age (Gyr)	200, 350, 500, 750, 1000, 1250, 1500, 1600	as for Chabrier	as for Chabrier	200, 350, 500, 750, 1000, 1250, 1500
Burst Age (Gyr)	8, 10, 30, 50, 75, 100, 150	as for Chabrier	as for Chabrier	as for Chabrier
IMF	Chabrier	Salpeter	Salpeter	Chabrier
Nebular lines	Yes	Yes	No	Yes
Ionisation parameter	-2.0	as for Chabrier	N/A	as for Chabrier
Line width (km/s)	300	as for Chabrier	N/A	as for Chabrier
EBV young	0.02, 0.04, 0.08, 0.1, 0.12, 0.14, 0.18, 0.2 0.26, 0.28, 0.3	as for Chabrier	as for Chabrier	0.02 to 0.3 (in steps of 0.01)
EBV old	0.1, 0.5, 0.9	as for Chabrier	as for Chabrier	0.1, 0.3, 0.5, 0.7, 0.9
Dust emission	D14	D14	D14	C12
AGN fraction	0.0, 0.1, 0.2, 0.3, 0.4, 0.5	as for Chabrier	as for Chabrier	as for Chabrier
Dust alpha	1.0, 2.0, 3.0	as for Chabrier	as for Chabrier	1.5, 2.0, 2.5
Dust temperature (K)	N/A	N/A	N/A	27, 37, 47
Emissivity index	N/A	N/A	N/A	1.2, 1.6, 2.0

3.4 SED Fitting

I used version 0.9 of the SED fitting code CIGALE (Code Investigating GALaxy Emission) to estimate the stellar mass of my LBG samples [2]. The original Fortran version of the code is described in Noll et al. (2009). CIGALE uses UV-optical stellar synthesis population model templates (Bruzual and Charlot, 2003; Maraston, 2005, BC03, M05) to generate simple or complex stellar populations. These are then combined with a dust component in the IR (Draine and Li, 2007; Casey, 2012; Dale et al., 2014, D07, C12, D14), and CIGALE can also be configured to allow for nebular emission lines, dust attenuation (Calzetti et al., 2000) and AGN, as described in more detail below.

CIGALE minimises the χ^2 between the observed and model photometry, however it also uses what the authors describe as a 'Bayesian-like' analysis. It is common practice to calculate the probability of individual models (where a model is a given combination of input parameters and choices of stellar SED, dust models etc.) as $\exp^{-\chi^2/2}$, these probabilities are then used

[2] http://cigale.lam.fr/

to produce a probability distribution function (PDF) for a given parameter space. However, this approach can lead to biases due to variation in the model density of different regions of parameter space. The CIGALE 'Bayesian-like' approach seeks to avoid this potential bias. The probability (or likelihood) of each model is calculated by integrating over the PDF from χ^2 to infinity:

$$p(\chi^2/n) = \int_{\chi^2}^{\infty} \frac{x^{(n/2)-1}\exp^{-x/2}}{2^{n/2}\Gamma(n/2)}\mathrm{d}x \tag{3.1}$$

where Γ is the Gamma Function and $n = k-1$, the filter related degrees of freedom. Each output parameter, x (e.g. stellar mass), is then divided into b equal sized bins, i, covering the possible range of values. The probability of each bin containing the expected parameter value is found by searching all models in that bin for the maximum value of $p(\chi^2/n)$:

$$P_i(x) = max(p_j(\chi^2/n)a_{ji}) \quad j\text{=1....m} \tag{3.2}$$

where m is the number of models and a_{ji} is a prior which equals unity if the model j belongs to bin i and otherwise equals zero. The resulting PDF gives the distribution of maximum probabilities for the parameter bins. The expected value for the parameter is then calculated using $P_i(x)$ as a weight for each bin:

$$\langle x \rangle = \frac{\sum_{i=1}^{b} P_i(x)x_i}{\sum_{i=1}^{b} P_i(x)} \tag{3.3}$$

where x_i is the best fit value of x in each bin. The uncertainty is then simply the standard deviation:

$$\sigma_x = \sqrt{\frac{\sum_{i=1}^{b} P_i(x)(x_i - \langle x \rangle)^2}{\sum_{i=1}^{b} P_i(x)}} \tag{3.4}$$

Full details of the approach are given in Noll et al. (2009).

As my primary goal was to compare the stellar mass of average LBGs in the protocluster and field I calculated weighted mean and 'weighted' median photometry for each sample. This was done by combining the photometry of all LBGs for each wavelength and taking the standard error as the uncertainty on each band. The 'weighted' median was calculated using a bootstrapping approach (the flux value and associated uncertainty for each LBG in a given waveband was used to generate a normal distribution from which 10000 values were sampled and the median of all these values (10000 $\times$ the number of LBGs) was then taken to be the weighted median of the LBG population). I then ran CIGALE on this average photometry and compared the results

(see Section 3.5). I also ran CIGALE on average photometry using the standard deviation of the sample as the uncertainty rather than the standard error. This was to ensure that I took account of the large range of photometry values (reflecting large intrinsic scatter) within the sample. The use of this alternative measure of uncertainty did not affect my results.

The choice of inputs can impact the results of the fitting process, for example BC03 templates will give a mass 0.2 dex greater than M05 as they fail to take account of the thermally-pulsating asymptotic-branch stars (TP AGB, Maraston et al., 2006; Salimbeni et al., 2009). These stars were found to burn fuel much more rapidly than had been predicted and hence have much shorter lives impacting predicted mass (Maraston, 1998). Whilst some of these differences should be systematic and have an equal effect on the protocluster and field samples, I wanted to ensure that my choice of inputs did not bias my results. I therefore applied four different combinations of stellar templates, dust models and parameters in order to confirm that any differences between the protocluster and field were not dependent on inputs. These four models are summarised in Table 3.2. The 'Chabrier' model uses the BC03 stellar templates, D14 dust model, Chabrier IMF (Chabrier, 2003) and allows for nebular emission lines. The 'Salpeter' model is identical to the Chabrier model, except for the use of the Salpeter IMF (Salpeter, 1955). The 'M2005' model uses the M05 templates and Salpeter IMF and does not allow for nebular lines (this option is not available with the M05 templates), but is otherwise identical to the Chabrier model. The 'C12' model is identical to the Chabrier model except that it uses the C12 dust emission model and allows for a wider range of dust extinction values. This required some minor changes to the other parameter ranges to keep the number of model options within practical limits.

For all models I have two exponentially-declining star bursts described by the 'Age' parameter (giving the age of the stars from the initial burst), 'Burst Age' (giving the age of the second burst), 'burst fraction' (indicating the mass fraction of the late burst population) and 'τ main' and 'τ age' (indicating the rate of decline of the star formation rate of each burst). I fix metallicity at Solar and the age separation of old and young stars at 10 million years for all models.

Extinction is based on the Calzetti model, but is modified by a UV bump centered at 217.5nm, with an amplitude of $R_v = 3$ and a width of 35nm. This represents the additional absorption observed at these wavelengths in the Milky Way. The Calzetti slope can also be modified by a powerlaw varying between -0.3 and 0.3. Two further parameters can be varied to describe the dust extinction in the younger stellar population (EBV young) and the reduction factor of E(B-V) for the older stellar population compared to the younger (EBV old).

Dust re-emits the absorbed UV light at longer wavelengths, particularly in the IR and submm regime. Continuum dust emission at submm wavelengths is caused by large dust particles (0.01-0.25μm) in thermal equilibrium with the low temperature (typically 15-60K) radiation field. In the MIR continuum emission is mostly from stochastically heated small grains ($\sim$0.01μm), but is overlaid by prominent emission lines from polycyclic aromatic hydrocarbons (PAHs, e.g.

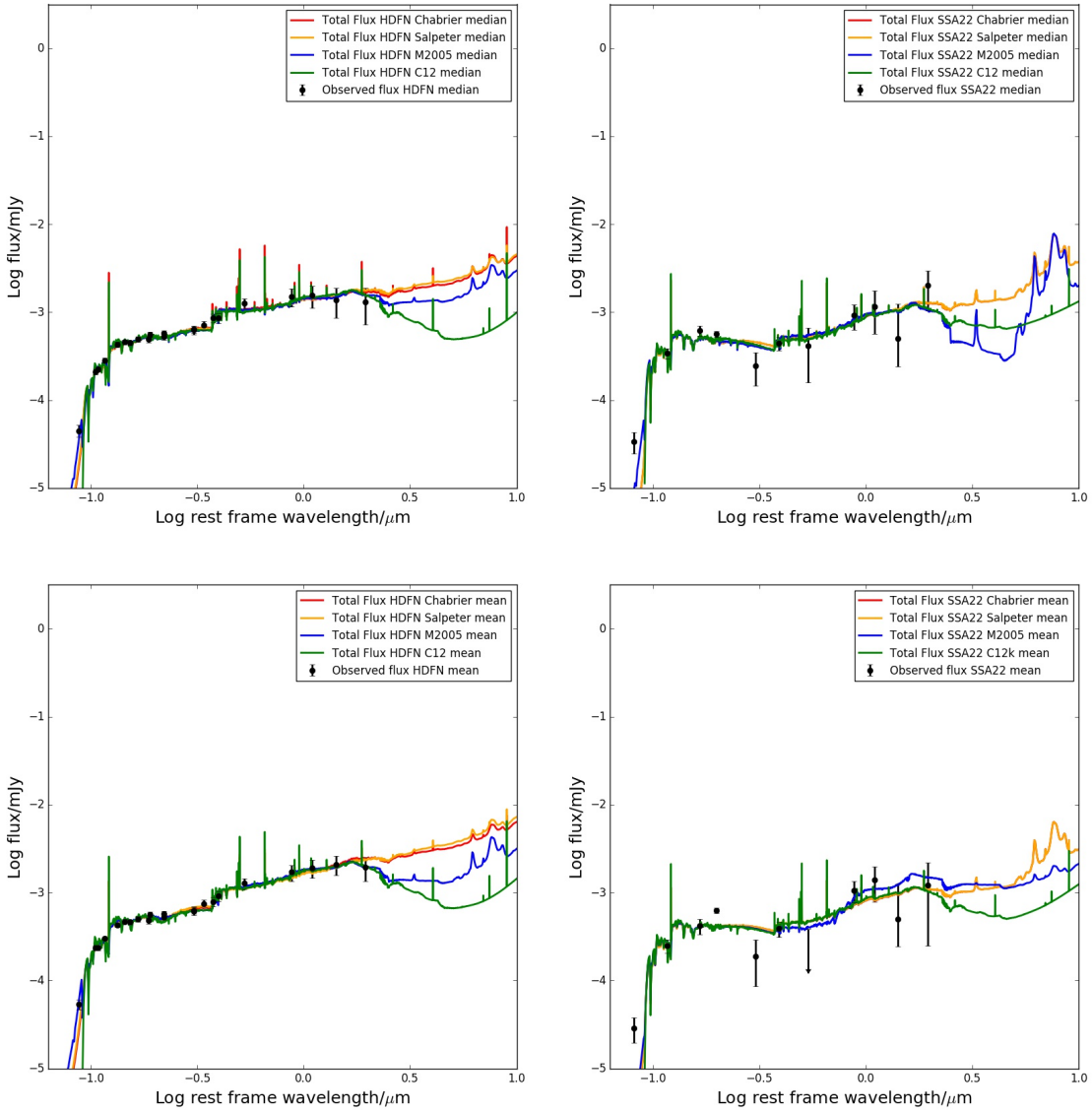

FIGURE 3.1: Average SSA22 and HDFN SEDs for my four test models. The top row are the median LBGs and the bottom row the mean LBGs, with HDFN on the left and SSA22 on the right. The observed photometry is shown as black circles. (Note that for the SSA22 photometry the Chabrier and Salpeter models result in almost identical SEDs and therefore the red Chabrier line is not visible.)

Leger and Puget, 1984; Tielens, 2008; da Cunha et al., 2008). The D14 dust emission model consists of empirical templates parametrised by α_{SF} (dust alpha) representing the relative contribution of the various templates. The FIR re-emission is modelled to balance the absorption of dust under the Calzetti model, however it also allows for additional emission from AGN (not balanced by dust absorption). By contrast C12 uses an SED composed of a power law in the MIR and a grey body in the FIR. It is described by three parameters, temperature and emissivity index for the grey body and a dust alpha for the power law.

In Figure 3.1 I show the SEDs produced by the 'Bayesian-like' fit for each of my four models. The median SEDs are shown on the top row and the means on the bottom.

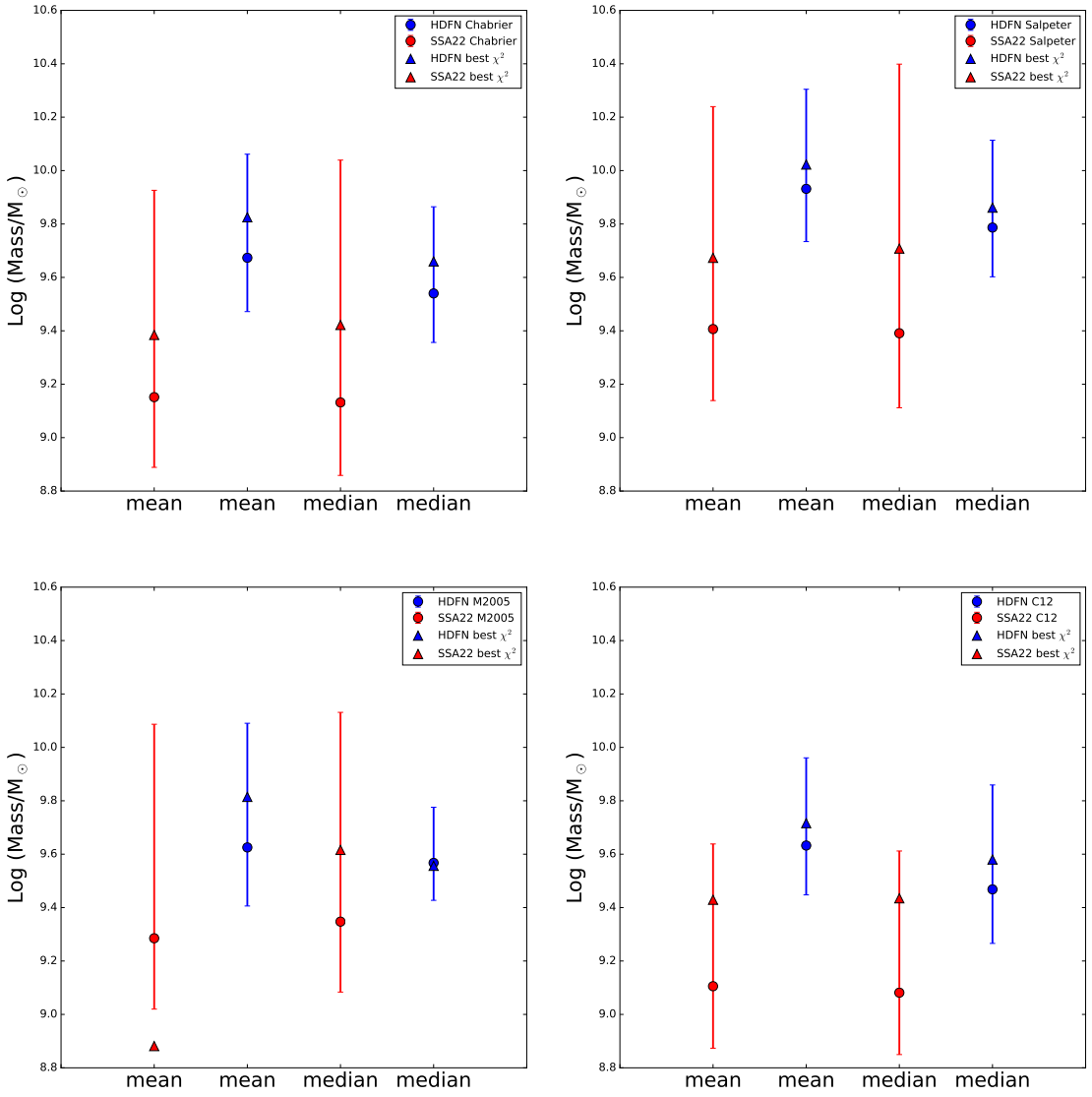

FIGURE 3.2: Log Mass of mean and median LBGs in the field (blue) and protocluster (red) for my four test models. Circles indicate the expected values from the 'Bayesian-like' fit with related uncertainties, triangles indicate the best χ^2 fit.

3.5 Analysis

In Fig. 3.2 I plot the stellar mass expected values and uncertainties for the protocluster (red) and field (blue) mean and median LBGs. For all model fits there is no significant difference in the mass of an average LBG within the protocluster compared to the field. The figure also indicates the best χ^2 fit for each model, which is consistent with the 'Bayesian-like' fit in all but one case. Although the best χ^2 mass value lies within the range of possible values for the 'Bayesian-like' fit it is generally higher than the expected value, suggesting that a χ^2 approach could lead to overstated masses. The mean mass varies for different models, with the highest masses corresponding to BC03 templates with a Salpeter IMF (as we would expect given that both the BC03 models and Salpeter IMF lead to higher mass). The M05 stellar models result in

lower mass values due to the inclusion of TP AGB stars and the Salpeter IMF results in higher mass values (as it overstates the number of low mass stars), these two effects largely cancel in the M2005 models giving masses similar to the BC03/Chabrier IMF combination. The use of the C12 dust model results in slightly lower masses. In this case the choice of parameters will have an impact on the mass, this is not a problem for comparing the two populations of LBGs (as any impact will be consistent), but it makes comparing masses with the other models inappropriate. However, in all cases the field and protocluster masses are consistent within the uncertainties. I also ran CIGALE on a version of the average HDFN LBGs with the photometry restricted to those filters available for the SSA22 LBGs to ensure that the different photometry was not introducing any bias. This had no impact on my analysis.

All masses output by CIGALE have large uncertainties, this is to some extent unavoidable due to the various assumptions made during the fitting process. In particular the output uncertainties on the mean and median LBG masses are influenced by the input uncertainty on the average photometry. This is the standard error of the LBG flux densities, and in the case of the protocluster this is a large number due to the small number of galaxies in the sample and the relatively large intrinsic scatter in flux-density values. The field sample is larger and this helps to reduce the standard error. If the errors on the protocluster sample were half their actual value I would still see no evidence for a difference in mass for the medians for all four test models. The means would show no difference for M2005, but for the other three models would actually indicate that the mass of LBGs is higher in the field group.

Due to the large uncertainties on the mass values relating to the average photometry I also consider the mass values obtained when CIGALE is run on the individual LBGs. Fig. 3.3 shows the distribution of possible stellar mass values for each LBG based on the CIGALE fitting. I used the 'Bayesian-like' value of mass and the associated uncertainty as the mean and standard deviation to define a Gaussian distribution for each LBG, from which I then sampled and plotted 10,000 values of mass. The figure illustrates the large degree of overlap of these two populations. Again I see a slight trend towards more massive galaxies in the field, but this is not statistically significant. To confirm this I applied a two sample Kolmogorov-Smirnov (KS) test 10,000 times to the sampled mass values, resulting in a mean p-value $\geq$ 14% for all of the models. I therefore accept the null hypothesis that both samples are from the same population.

I also considered the two redshift peaks within the protocluster reported by Topping et al. (2016). These are thought to represent two separate physical structures, which will eventually merge. Only two of my SSA22 LBGs lie clearly within the blue ($z \sim 3.069$) peak, a further five lie in the trough between the two peaks, leaving 19 clearly within the red ($z \sim 3.095$) peak. I compared these 19 LBGs to the HDFN sample to ensure that there was no sign of enhanced mass within this structure. My KS test showed a p-vlaue of $\geq$11% for all four models, confirming that there is no statistical difference in the mass of the two LBG populations.

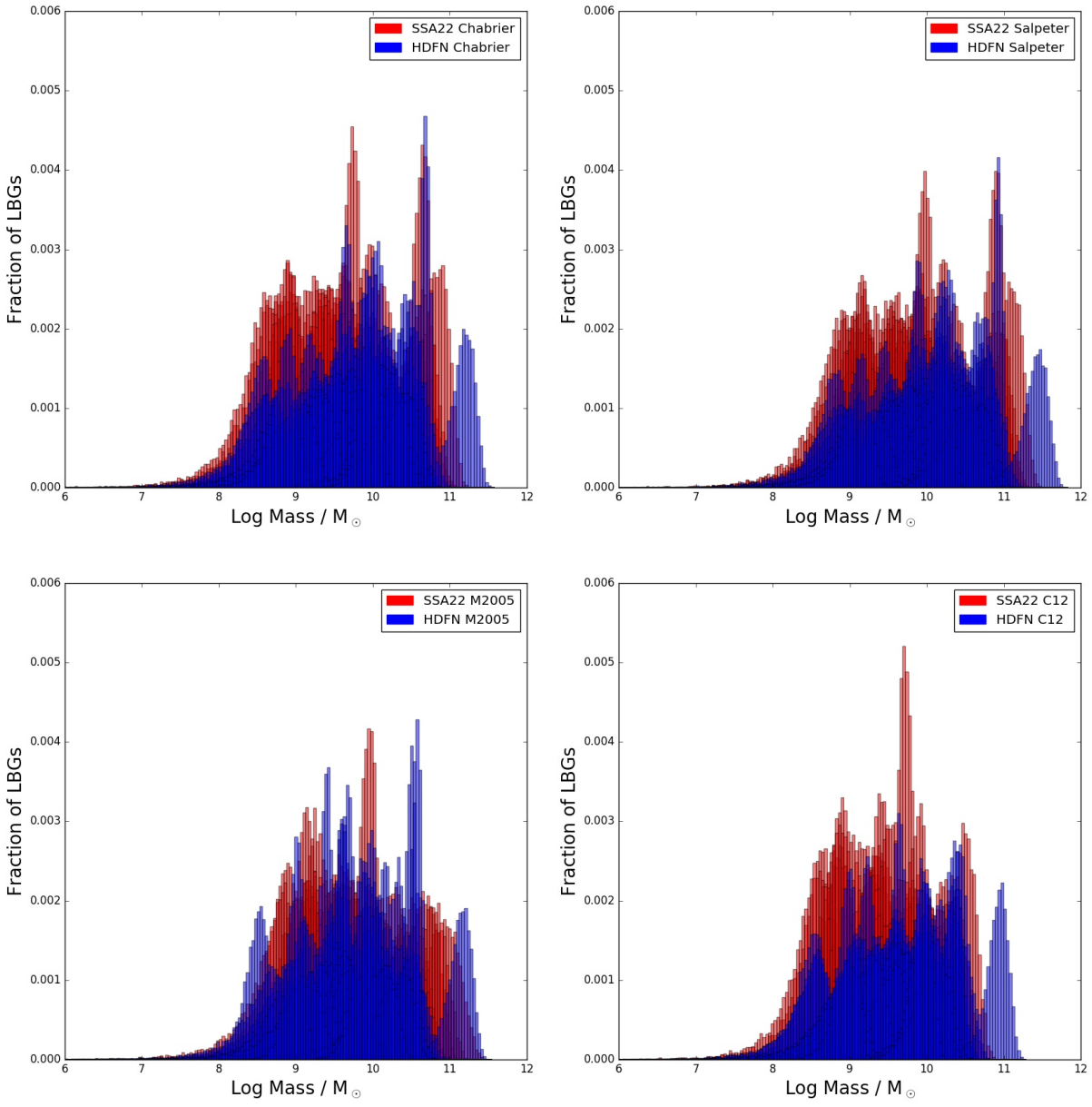

FIGURE 3.3: The possible stellar mass distributions for the LBGs in the field (blue) and protocluster (red) for my four test models. I used the masses and uncertainties obtained from the 'Bayesian like' fits to create Gaussian distributions for each LBG, from which I then sampled and plotted 10,000 values of mass. The distributions have been normalised to aid comparison.

3.6 Discussion

I find no evidence that the SSA22 protocluster LBGs are more massive than those in the field at $z \sim 3$, despite finding an enhanced merger fraction in the same protocluster in previous work (Chapter 2 and Hine et al., 2016). I may be observing the protocluster during a period when the cosmic overdensity is causing an increase in the frequency of mergers, but has not yet lead to the protocluster LBGs accumulating sufficient additional mass for an enhancement in mass to be observed. Protoclusters at $2 < z < 2.5$ have potentially had an additional $\sim$0.5-1.2 Gyr to evolve and build mass compared to $z \sim 3$. This may explain the detection of a mass enhancement in the LBG and Hα emitter (HAE) populations of lower redshift protoclusters (Steidel et al. 2005, Hatch et al. 2011, Koyama et al. 2013, Cooke et al. 2014), when I fail to detect one at $z \sim 3$. Studies at $z > 3.5$ have not detected evidence of enhanced mass in protocluster LBGs (Overzier et al., 2008, 2009) and so it may be that the transition to protoclusters dominated by more massive galaxies occurs at $2.5 \leq z \leq 3.5$. However, such a trend is not supported by all studies, Cucciati et al. (2014) find no evidence for a difference in mass in their sample of $z = 2.9$ protocluster galaxies detected in the VIsible MultiObject Spectrograph (VIMOS) ultra deep survey (VUDS).

Different selection techniques sample galaxies with different masses and SFRs and this may contribute to the conflicting results in some of these studies. HAEs have a wider range of masses than LBGs (Oteo et al., 2015), this increases the potential intrinsic scatter, so it may be easier to detect a clear difference in mass in populations of HAEs than in populations of LBGs. It should also be noted that just as the final mass of clusters varies due to the amplitude of the initial dark-matter overdensities, so too will the redshift at which the galaxy populations of individual protoclusters become more massive than the field. Initial dark-matter overdensities of different amplitudes will build baryonic mass at different rates, so at a given redshift protoclusters (and the galaxies within them) are likely to be at different stages of evolution (e.g. Chiang et al., 2013; Muldrew et al., 2015). A larger initial amplitude is likely to lead to a protocluster galaxy population that exceeds the average field mass at an earlier redshift than a smaller initial amplitude. So I would expect to see some variation in the redshift at which departure from the field norm becomes observable.

Lehmer et al. (2009) suggested that the galaxies in the SSA22 protocluster were $\geq$ 1.2-1.8 times more massive than those in the field. This conclusion was based on predicted median rest frame H-band absolute magnitudes, which they obtained by fitting an SED to multiwavelength data using the HYPERZ fitting code. My best fit median flux density values for H-band (rest frame) do not show the same trend. In fact I find median H band flux densities are slightly greater in the field than in the protocluster based on my best fit SEDs for all four models (although I do not place any reliance on this trend due to the uncertainties in the fitting process). The difference between my results and those in Lehmer et al. (2009) may be due in part to my use of TPHOT to

obtain more reliable photometry for the IRAC bands (the IRAC3 and IRAC4 bands are closest to the rest frame H-band at $z = 3.1$). SED fitting is also a more reliable method of obtaining mass than assuming a direct correlation with the H-band photometry, as it makes use of a larger data set and allows for exploration of a larger parameter space. It has also been suggested that caution is required when using H band photometry as a tracer of mass due to the uncertainties introduced by emission from TP AGB stars (Zibetti et al., 2009; Conroy, 2013).

In contrast, Alexander et al. (2016) found no difference in the mass of AGN in the SSA22 protocluster and the field, in line with my results. Kubo et al. (2015) found evidence of massive quiescent galaxies within the SSA22 protocluster, but it is not yet clear whether they are statistically more massive than their equivalents in the field. Studies of other $z \sim 3$ protoclusters also show mixed results. Kuiper et al. (2010) found that their protocluster LBGs were more massive than the field, but they concluded that this was not significant given the uncertainties of SED fitting. Lemaux et al. (2014) found an overdensity of very massive galaxies in a $z = 3.3$ protocluster although they also found that the general galaxy population was not significantly different from the field. Their sample is not directly comparable to ours as it was not restricted to LBGs. It is possible that whilst the LBG population of the SSA22 protocluster does not have a detectable mass enhancement, other galaxy populations within the protocluster do.

3.7 Conclusions

In summary I have found no indication of a significant difference in the mass of average LBGs in the protocluster compared to the field. It may be that I am observing these galaxies before they have had time to acquire additional mass. To confirm this result it would be useful to obtain better photometry, which would, hopefully reduce the uncertainties in the mass values. Improved photometry might also allow me to extend this work to look at other physical properties, such as age and SFR. I discuss the potential for improving the fitting results further in Chapter 5.

Chapter 4

The average submillimetre properties of Lyman-α Blobs at $z = 3$

The work in this chapter has previously been published as Hine et al., 2016, *Monthly Notices of the Royal Astronomical Society*, 455, 2363.

4.1 Introduction

Lyman-α Blobs (LABs) are large diffuse regions of Lyman-α (Lyα) emission (10 – 100 kpc scale) with integrated Lyα luminosities of $\sim 10^{42}$ - 10^{44} erg s^{-1} typically found at $z = 2$ – 6 (although one was detected at $z \sim$1, Barger et al. 2012). The first LAB was detected in the Small Selected Area 22^{hr} (SSA22) field at $z \sim 3$ (Steidel et al., 2000), however, extended areas of diffuse Lyα emission (that we might now class as LABs) had earlier been detected around overdensities of luminous galaxies and AGN at $z \sim 2.4$ (Francis et al. 1996; Keel et al. 1999), in association with high redshift submillimetre galaxies (SMGs, Ivison et al., 1998) and around high redshift radio galaxies (De Breuck et al. 1999; Kurk et al. 2000). Later surveys have detected further high redshift LABs with a range of sizes and luminosities (Matsuda et al. 2004; Matsuda et al. 2009; Matsuda et al. 2011; Yang et al. 2009; Erb et al. 2011 Bridge et al. 2013). Many appear to lie in dense regions that are expected to become massive clusters (Steidel et al., 1998).

The Lyα emission in LABs is thought to be powered either by feedback processes (involving superwinds, massive stars or AGN), or cold gas accretion. Many LABs contain luminous ionizing sources that could provide the energy needed to generate the observed Lyα emission (Francis et al. 1996; Keel et al. 1999; Dey et al. 2005; Geach et al. 2005; Geach et al. 2007; Geach et al. 2009; Geach et al. 2014; Webb et al. 2009; Rauch et al. 2011; Cantalupo et al. 2012; Ao et al.

2015). One scenario is that Lyα is emitted from cold gas clouds in a central galaxy fuelled either by massive stars or an AGN. A fraction of the Lyα emission escapes the galaxy and is scattered into our line of sight by the circumgalactic medium (CGM, Zheng et al. 2010: Zheng et al. 2011; Steidel et al. 2011; Hayes et al. 2011c; Rauch et al. 2011; Cen and Zheng 2013; Geach et al. 2014). An alternative scenario involves ionizing radiation escaping from a galaxy, or AGN, (which may be offset from the centre of the LAB) leading to Lyα emission from cold gas in the CGM itself, which is then also scattered by gas in the CGM (Cantalupo et al. 2012; Prescott et al. 2015). Geach et al. (2009) showed that the typical bolometric luminosities of such sources are sufficient to power the observed Lyα emission. The third feedback process involves superwinds. Here a starburst leads to multiple supernovae, creating overlapping bubbles which form a superwind and shock heat cold gas (Taniguchi and Shioya 2000; Mori et al. 2004; Mori and Umemura 2006). It is possible that more than one of these processes is contributing to the observed emission, especially in the larger LABs that contain multiple galactic sources.

However, not all LABs have been found to contain luminous galaxies or AGN (Nilsson et al. 2006; Smith and Jarvis 2007; Smith et al. 2008). Hydrodynamic simulations suggest that the growth of massive ($M_h \geq 12M_{\odot}$) galaxies at $z \geq 2$ is dominated by 'cold mode' accretion. Narrow streams of cold ($T \sim 10^{4-5}$K) pristine gas penetrate the hot, virially shocked gas in the galaxy halo (Katz et al. 2003; Keres et al. 2005: Keres et al. 2009, Dekel et al. 2009). So far there is little direct observational evidence for the existence of such flows, however simulations have predicted the emission of Lyα from infalling cold gas (Dijkstra et al. 2006b; Haiman et al. 2000). Goerdt et al. (2010) found that the cold streams in their high-resolution simulations could produce the observed physical properties of LABs and similar results were obtained by Rosdahl and Blaizot (2012). However the moving mesh code simulation investigated by Nelson et al. (2013) did not support the existence of cold flows in all dark matter haloes (DMHs). They found that the fraction of gas that remained cold as it approached the central galaxy was sensitive to the simulation code used. In addition Faucher-Giguère et al. (2010) found that in their simulations cold accretion could not power the LABs unless emission from dense cores capable of producing star formation were included, whereas feedback processes could provide the observed emission.

It is difficult to predict the actual Lyα flux resulting from the gas flows generated in these simulations. The flux will depend on gas turbulence, radiative transfer and the presence of local ionizing sources (Rosdahl and Blaizot, 2012). The radiative transfer is particularly complicated due to the resonance of the Lyα line (Neufeld, 1990) and its sensitivity to assumptions about sub-grid physics (Nelson et al., 2013). Simulations using different models of radiative transfer therefore predict a wide range of physical and observable properties (Dijkstra et al. 2006a; Dijkstra et al. 2006b; Faucher-Giguère et al. 2010; Rosdahl and Blaizot 2012; Nelson et al. 2013).

Recently Prescott et al. (2015) suggested that the non-detection of a luminous galaxy within some LABs is actually evidence *against* cold accretion, as such flows should be triggering star formation at a similar rate to the gas inflow ($\sim$100s $M_{\odot}$ yr^{-1}). Hayes et al. (2011a) found evidence of polarization from a large LAB at $z \sim$3, suggesting the presence of a central ionizing source rather than cold accretion (see also Geach et al., 2014). Cen and Zheng (2013) presented a model relying primarily on ionizing sources to provide the energy for LABs, but with a contribution from cold gas accretion. This successfully reproduced the Lyα luminosity function and the luminosity-size relation of the Matsuda et al. (2004) and Matsuda et al. (2011) LABs. It appears likely that both cold gas accretion and heating by feedback processes play a part in the creation of LABs, but the relative importance of the different mechanisms is still unclear.

In this work I consider the LABs in the extensively studied $z = 3.1$ SSA22 protocluster. The two largest LABs in SSA22 (LAB1 and LAB2) were first detected by Steidel et al. (2000) during a general Lyα survey of the protocluster. LAB1 and LAB2 have since been studied extensively at a range of wavelengths (Chapman et al. 2001; Chapman et al. 2004; Bower et al. 2004; Wilman et al. 2005; Geach et al. 2005; Geach et al. 2014; Matsuda et al. 2007; Webb et al. 2009; Uchimoto et al. 2008; Uchimoto et al. 2012; Martin et al. 2014). A comprehensive search for LABs in the protocluster (Matsuda et al., 2004, M04) identified a total of 35 LABs with a flux greater than 0.7×10^{-16} erg s^{-1} cm^{-2} (which they defined as the limit for LABs) varying in area isophotal from 222 arcsec^2 to 16 arcsec^2.

Geach et al. (2005) used the Submillimetre Common User Bolometer Array (SCUBA) instrument on the James Clerk Maxwell Telescope (JCMT) to search for submillimetre (submm) sources in 25 of the LABs. They found individual 850μm detections at $\geq 3.5\sigma$ for five LABs (LABs 1,5,10,14,18, IDs from M04) and a detection at the $\geq 3.0\sigma$ level for the full sample using mean stacking (at a 1σ depth of 1.5mJy for the main sample and $\sim$5.3mJy for a subset). However, AzTEC/ASTE 1.1mm observations of the 35 LABs (with an rms noise level of 0.7 – 1 mJy beam^{-1}) did not detect any sources at $>3.5\sigma$, whilst their stacking analysis showed a mean $S_{1.1mm}$ <0.40 mJy (3σ) (Tamura et al., 2013). More recently, deeper Atacama Large Millimeter/submillimeter Array (ALMA) observations have detected 1.1mm sources in LABs 12 and 14 (Umehata et al., 2015).

The deeper SCUBA-2 survey of the SSA22 field (1.1 mJy, compared to 1.5 mJy at 1σ) is now complete and I have used these data to revisit the work of Geach et al. (2005) obtaining updated individual and stacked submm detections for 34 SSA22 LABs (there is no coverage of LAB17). SCUBA-2 sources at $z \sim 3$ are expected to be SMGs which could provide the star-forming activity required to fuel the LABs.

4.2 Observations

4.2.1 Submm observations

The SSA22 field was observed as part of the JCMT Submillimetre Common User Bolometer Array 2 (SCUBA-2, Holland et al. 2013 Cosmology Legacy Survey (S2CLS, project ID MJLSC02). 105 observations were made between 23 August 2012 and 29 November 2013 to produce a $30'$ diameter map centred on 22:17:36.3, +00:19:22.7. The limiting conditions were a zenith optical depth in the range $0.05 < \tau_{225} < 0.1$, with a mean $\tau_{225} = 0.07$. The beam-convolved map has a 1σ depth of 1.1 mJy beam^{-1} and an integration time of $\sim$3000s per 2 arcsec pixel.

The data reduction steps are described fully in (Geach et al., 2017), but I describe the main steps here. The Dynamical Iterative Map-Maker (DIMM) within the *Sub-Millimetre Common User Reduction Facility* (SMURF; Chapin et al. 2013) is used to extract astronomical signals from each SCUBA-2 bolometer time stream, mapping the result onto a celestial projection. All S2CLS maps are projected on a tangential co-ordinate system with 2 arcsec pixels.

Flat-fields are applied to the time-streams using flat scans that bracket each observation, and a polynomial baseline fit is subtracted from each time stream. Data spikes are rejected (using a 5σ threshold in a box size of 50 samples), DC steps are removed and gaps filled. Next, an iterative process begins that aims to fit the data with a model comprising a common mode signal, astronomical signal and noise. The common mode modelling is performed independently for each SCUBA-2 sub-array, deriving a template for the average signal seen by all the bolometers; it is removed from the stream, and an extinction correction is applied (Dempsey et al., 2013). Next, a filtering step is performed in the Fourier domain, which rejects data at frequencies corresponding to angular scales $\theta > 150$ arcsec and $\theta < 4$ arcsec. Finally, a model of the astronomical signal is determined by gridding the time streams onto a celestial projection (since a given sky position will have been visited by many independent bolometers) and then subtracted from the input time streams. The iterative process continues until the residual between the model and the data converges.

The last processing step is to apply a matched filter to the maps, convolving with the instrumental PSF to optimize the detection of point sources. Geach et al. (2017) used the PICARD recipe *scuba2_matched_filter* which first smooths the map (and the PSF) with a 30 arcsec Gaussian kernel, then subtracts this from both to remove any large scale structure not eliminated in the filtering steps that occurred during the DIMM reduction. The map is then convolved with the smoothed beam. A flux conversion factor of 591 Jy beam^{-1} pW^{-1} is applied; this canonical calibration is the average value derived from observations of hundreds of standard submillimetre calibrators observed during the S2CLS campaign (Dempsey et al., 2013), and includes a 10 per

cent correction necessary to account for losses that occur due to the combination of filtering steps applied to the data (see Geach et al. 2013). The flux calibration is expected to be accurate to within 15 per cent.

4.2.2 Infrared observations

I obtained reduced *Spitzer Space Telescope* (*Spitzer*) observations of the SSA22 protocluster from the Infrared Science Archive (IRSA). The observations used were from GTO 64 and GTO 30328 (P.I.: Fazio) and GO 3473 (P.I.: Blain). PID 64 and 30328 were used by Webb et al. (2009) in their analysis of IRAC and MIPS sources in the SSA22 LABs. PID 64 is a single pointing consisting of a $\sim 5' \times 5'$ area observed with IRAC (AORID 4397824) with an integration time of 6400s pixel^{-1}. PID 30328 covered an area of ~ 375 arcmin^2 using IRAC (AORIDs 17599488, 17599744, 17600000, 17600256, 17600512) with integration times of $3000 - 7500$s pixel^{-1}. This included a 225 arcmin^2 region covered by all four wavelengths to a uniform depth of 7500s pixel^{-1}. I used data from PID 3473 for LABs not covered by these deep observations. These shallower observations achieved a depth of 0.2, 0.5, 3.1 and 4.5μJy for IRAC channels 1 to 4 respectively (Hainline et al., 2009). Where available I reviewed data for all four IRAC channels (3.6 - 8 μm). These data were used to identify IRAC sources within the LABs, the coordinates of which were then used for stacking the SCUBA-2 data, see Section 4.3.2.

4.3 Analysis

4.3.1 Individual Sources

The SCUBA-2 850μm flux density (S_{850}) measurements for the individual LABs are listed in Table 4.1. Only two have significant detections at $\geq 3.5\,\sigma$, LAB1 and LAB18, indicated in bold in the Table. LAB16 is marginally detected at $\sigma = 3.0$.

Our results differ from those in Geach et al. (2005, G05), which had five detections at ≥ 3.5 sigma and larger flux density values for both LAB1 and LAB18. The revised flux density figure for LAB1 was first reported in Geach et al. (2014), which suggested that the discrepancy may have been due to flux boosting in the original SCUBA data (Chapman et al., 2001). As well as flux boosting, the SCUBA results from G05 may be subject to enhancement due to early issues with data reduction and calibration, whereas the SCUBA-2 pipeline is considered to be more mature and more reliable. There is no SCUBA-2 coverage of LAB17 which lies on the edge of the field.

TABLE 4.1: Summary of Lyα and 850 μm data relating to the individual SSA22 Lyman-α Blobs. The coordinates in columns two and three are from Matsuda et al. (2004) and give the location of the maxiumum Lyα luminosity. The IRAC coordinates give the offset from these values. The Geach et al. (2005) results are included for comparison (G05). The two individual detections are highlighted in bold. [1] The submm source close to LAB8 falls within the original boundary of LAB1. [2] Data taken from Matsuda et al. (2004).

ID[2]	RA[2]	Dec[2]	Area[2] arcsec^2	IRAC $\Delta\alpha$ $''$	IRAC $\Delta\delta$ $''$	Log($L_{Ly\alpha}$)[2] erg s^{-1}	S_{850} mJy	G05 S_{850} mJy
LAB1	**22 17 26**	**+00 12 32**	**222**	**3.3**	**3.0**	**44.0**	**4.6±1.1**	**16.8±2.9**
LAB2	22 17 39	+00 13 23	152	3.7	7.9	43.9	0.1±1.1	3.3±1.2
LAB3	22 17 59	+00 15 25	78	1.4	4.3	43.8	0.1±1.1	-0.2±1.5
LAB4	22 17 25	+00 22 05	57	4.3	-1.2	43.6	2.4±1.1	0.9±1.5
LAB5	22 17 12	+00 16 41	55	2.0	4.7	43.2	1.9±1.1	5.2±1.4
LAB6	22 16 51	+00 24 58	42	1.4	5.7	43.2	1.0±1.1	-0.5±1.8
LAB7	22 17 41	+00 11 20	40	no source	no source	43.2	1.2±1.1	0.2±1.6
LAB8	22 17 26	+00 12 50	39	2.2	-2.7	43.2	2.6±1.1[1]	0.3±5.3
LAB9	22 17 51	+00 17 20	38	6.0	-1.5	43.1	2.2±1.1	1.3±5.3
LAB10	22 18 02	+00 25 52	34	1.3	7.4	43.3	3.2±1.1	6.1±1.4
LAB11	22 17 20	+00 17 28	30	-1.5	-1.2	43.0	2.5±1.1	-0.4±5.3
LAB12	22 17 32	+00 16 55	29	3.8	1.3	42.9	0.8±1.1	3.2±1.6
LAB13	22 18 08	+00 16 41	28	-1.8	5.6	43.0	1.2±1.1	-
LAB14	22 17 36	+00 15 54	27	-0.8	-0.5	43.1	2.0±1.1	4.9±1.3
LAB15	22 18 08	+00 10 19	26	-2.5	1.8	43.3	2.4±1.1	-
LAB16	22 17 25	+00 11 13	25	2.6	5.3	43.0	3.4±1.1	2.2±5.3
LAB17	22 18 36	+00 07 16	24	0	0	43.1	-	-
LAB18	**22 17 29**	**+00 07 48**	**22**	**3.1**	**-3.6**	**42.9**	**5.2±1.1**	**11.0±1.5**
LAB19	22 17 19	+00 18 43	21	2.8	2.4	43.1	-0.4±1.1	-8.6±5.3
LAB20	22 17 35	+00 12 43	21	no source	no source	42.8	0.2±1.1	0.4±1.5
LAB21	22 18 17	+00 12 04	20	0.7	3.1	42.9	0.9±1.1	-
LAB22	22 17 35	+00 23 31	20	no source	no source	42.9	1.3±1.1	-
LAB23	22 18 08	+00 23 13	19	no source	no source	43.0	1.0±1.1	-
LAB24	22 18 01	+00 14 35	19	no source	no source	42.9	-0.6±1.1	-
LAB25	22 17 22	+00 15 47	19	no source	no source	42.8	-1.5±1.1	1.4±5.3
LAB26	22 17 50	+00 17 28	18	-3.0	2.0	42.8	1.1±1.1	-2.7±5.3
LAB27	22 17 07	+00 21 25	18	-1.6	1.4	42.8	2.1±1.1	0.5±1.6
LAB28	22 17 59	+00 22 48	18	no source	no source	43.3	-0.6±1.1	-
LAB29	22 16 54	+00 22 55	17	no source	no source	42.8	0.7±1.1	-
LAB30	22 17 32	+00 11 28	17	-1.9	0.6	43.0	1.9±1.1	3.3±1.3
LAB31	22 17 39	+00 10 59	17	no source	no source	43.0	0.0±1.1	-3.7±5.3
LAB32	22 17 24	+00 21 50	17	no source	no source	42.8	0.9±1.1	1.8±1.4
LAB33	22 18 12	+00 14 28	16	no source	no source	43.0	0.7±1.1	1.6±1.5
LAB34	22 16 58	+00 24 25	16	no source	no source	42.9	0.4±1.1	-
LAB35	22 17 25	+00 17 13	16	-4.0	1.7	43.0	1 .0±1.1	1.2±5.3

4.3.2 Stacking

I stacked the SCUBA-2 data to determine whether on average a submm source lies within each LAB. This would indicate a dust obscured source that could potentially produce the observed Lyα emission in LABs where no optical source has been detected. The stack consists of the inverse variance weighted mean of each pixel value in a 31 $\times$ 31 pixel square centred on the coordinates of each LAB (see Table 4.2). The value of the central pixel in the stack was taken as the weighted mean flux of all 34 LABs. The large size of the LABs (especially LAB1 and LAB2) introduces the risk of missing any associated SCUBA-2 sources, as the point of maximum $L_{Ly\alpha}$ emission (M04 coordinates) may not coincide with the SMG responsible for the emission due to scattering. This risk is mitigated to some extent by the large beam size (15 $''$), but to reduce it further I used data from *Spitzer* to search for infrared sources lying within, or close to the LABs (Geach et al. 2007; Webb et al. 2009). IRAC sources are often used to identify SMG counterparts as these longer wavelengths are less affected by dust than optical or UV (Ashby et al. 2006; Pope et al. 2006; Biggs et al. 2011; Michałowski et al. 2012b: Koprowski et al. 2015). By stacking on the coordinates of *Spitzer* sources (see Table 4.1), where available, I increased my chances of stacking on the location of any SMGs within the LABs. I identified potential IRAC counterparts using an aperture of radius = area$^{1/2}$ (the isophotal area of each LAB is as given in Table 4.1) centred on the original M04 coordinates. Where there was more than one potential source (e.g LAB1) I used existing studies to confirm the appropriate coordinates where possible (Geach et al. 2007; Webb et al. 2009) I fitted a Gaussian to the IRAC photometry to obtain the IRAC coordinates used in my stacking.

I also stacked subgroups of LABs to explore the possibility that they are not a homogeneous population, as more than one process may be responsible for the $L_{y\alpha}$ emission. I stacked based on both area and Ł$_{\mathrm{Ly}\alpha}$. The results of my various stacks are presented in Table 4.2 (which also includes the corresponding mean $L_{\mathrm{Ly}\alpha}$ and star formation rate for each stack) and Fig. 4.3.

Stacking all 34 LABs gives a significant detection of 0.6$\pm$0.2 mJy at 3.1σ, compared to a higher value of 3.0$\pm$0.9 mJy at 3.3σ in G05. I also stacked just those LABs included in the G05 stack resulting in a 0.8$\pm$0.2mJy detection at 3.5σ. This suggests that the smaller sample in G05 may have introduced some bias, but most of the change is due to the improved data. I compare our work to that of G05 in Section 4.5.2. Excluding the two individually-detected LABs reduces the stacked result to 0.3$\pm$0.2mJy at 1.7σ. The validity of excluding the two individual detections is controversial, but I include the result for information. I also carried out blind stacking of 10,000 sets of 34 random coordinates. This indicated a less than 0.1 per cent chance of obtaining a $\geq$ 3σ detection.

Fig. 4.1 presents a 62$''\times$ 62$''$ $\sim$480kpc projected at $z \sim$3.1) image showing the result of stacking all 34 LABs. The contours start at 2σ and are in steps of 0.5σ. Fig. 4.2 shows a histogram of

TABLE 4.2: LAB stacking results (LAB17 is not included in any of the stacks as there is no data for this LAB.) The mean $L_{Ly\alpha}$ for each stack is also included, based on the figures in M04. Star formation rates (SFR) are calculated from S_{850} using a modified black body model (see Section 4.4.1).

Stacked Sample	S_{850} mJy	Mean $L_{Ly\alpha}$ $\times 10^{43}$ erg s^{-1}	SFR $M_{\odot}$year^{-1}
All	0.6±0.2	1.8±0.05	50±20
All non detections (excluding LAB1 and LAB18)	0.3±0.2	1.6±0.05	30±20
LABs 1-12 ($>$ 29 arcsec^2)	1.4±0.3	3.1±0.09	120±30
LABs 2-12 (152 - 29 arcsec^2)	1.2±0.3	2.7±0.09	100±30
LABs 13-24 (28 - 19 arcsec^2)	0.6±0.3	1.0±0.09	50±30
LABs 13-24 (excl. 18, 28 - 19 arcsec^2)	0.2±0.4	1.0±0.1	20±70
LABs 25-35 (19 - 16 arcsec^2)	-0.3±0.3	0.9±0.09	-
Lyα Bright ($L_{Ly\alpha} > 1.0 \times 10^{43}$ erg s^{-1})	0.8±0.3	2.9±0.07	70±30
Lyα Faint ($L_{Ly\alpha} < 1.0 \times 10^{43}$ erg s^{-1})	0.4±0.3	0.8±0.07	30±30

the individual S_{850} values and the associated uncertainties for each bin. This confirms that the average S_{850} value for all LABs is greater than zero.

Stacking by size indicates a significant difference between the LABs with the largest areas and those with the smallest areas. LABs 1-12 (large LABs, $>$ 29 arcsec^2) have a significant 4.5σ detection (3.4σ if I exclude LAB1), whilst LABs 13-24 (medium LABs, 28 - 19 arcsec^2) and LABs 25-35 (small LABs $\leq$ 19 arcsec^2) do not have a significant detection ($<2\sigma$ for both groups). The Lyα Bright ($L_{Ly\alpha} > 1.0 \times 10^{43}$ erg s^{-1}) stack has a marginal 3.0σ detection (2.1σ excluding LAB1) whilst the Lyα Faint ($L_{Ly\alpha} < 1.0 \times 10^{43}$ erg s^{-1}) LABs are not detected (1.6σ, falling to 0.8σ when LAB18 is excluded). This indicates that the Lyα luminosity may be correlated with the S_{850}. However, neither population has a significant detection at $\geq$3.5σ and the result is very dependent on whether LAB16 is included in the faint or bright group (LAB16 is the the 18th brightest of all the LABs, so is included in the bright group only because I don't have coverage for LAB17 and could otherwise be included in either group). These differences are also illustrated in Fig. 4.3 which shows the S_{850} values for each stack. The large LABs have a marginally higher submm flux density than the other groups, albeit with a $\sim$1 σ significance.

4.4 Comparison to theoretical models

I now compare my SCUBA-2 results to two possible models for the production of LABs, central star formation (where the Lyα emission is generated inside a central galaxy and then scattered in the CGM) and cold gas accretion.

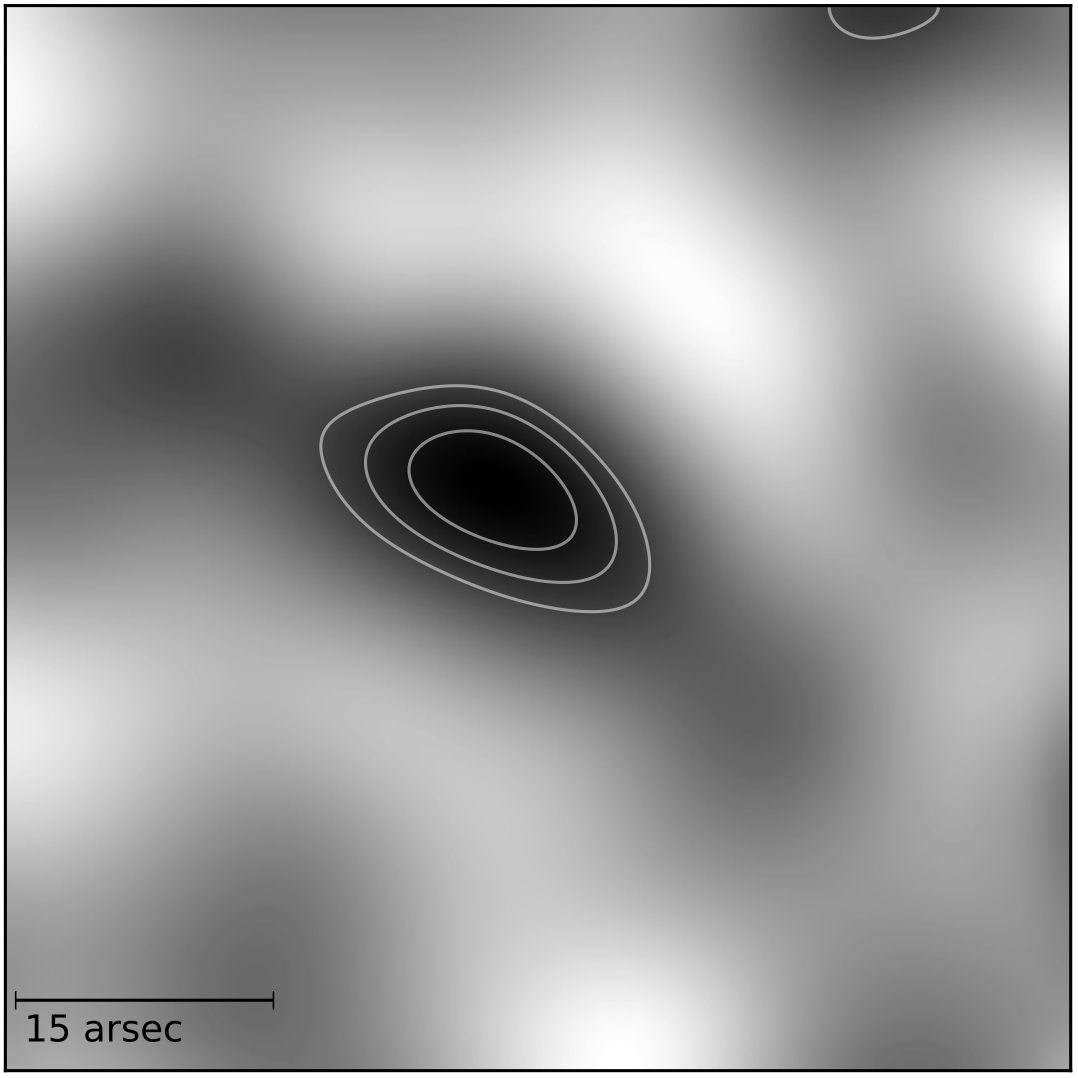

FIGURE 4.1: Result of stacking all 34 LABs. The image is 62 " × 62 " and the contours start at 2σ and are in steps of 0.5σ.

4.4.1 Star formation model

I assumed that the far infrared SED can be modelled by a modified black body allowing me to calculate theoretical values for total infrared luminosity (L_{IR}) corresponding to given S_{850} values. I used the modified blackbody function in equation 4.1 (Hildebrand 1983; Magnelli et al. 2012) and integrated between 8μm and 1000μm (rest frame).

$$S_\nu \propto \frac{\nu^{3+\beta}}{\exp(h\nu/kT_{\rm dust}) - 1} \tag{4.1}$$

where S_ν is flux density, β is the dust emissivity spectral index (assumed to be 2) and T_{dust} is the dust temperature (assumed to be 30K). I discuss the appropriateness of my assumed values in Section 4.5.3.

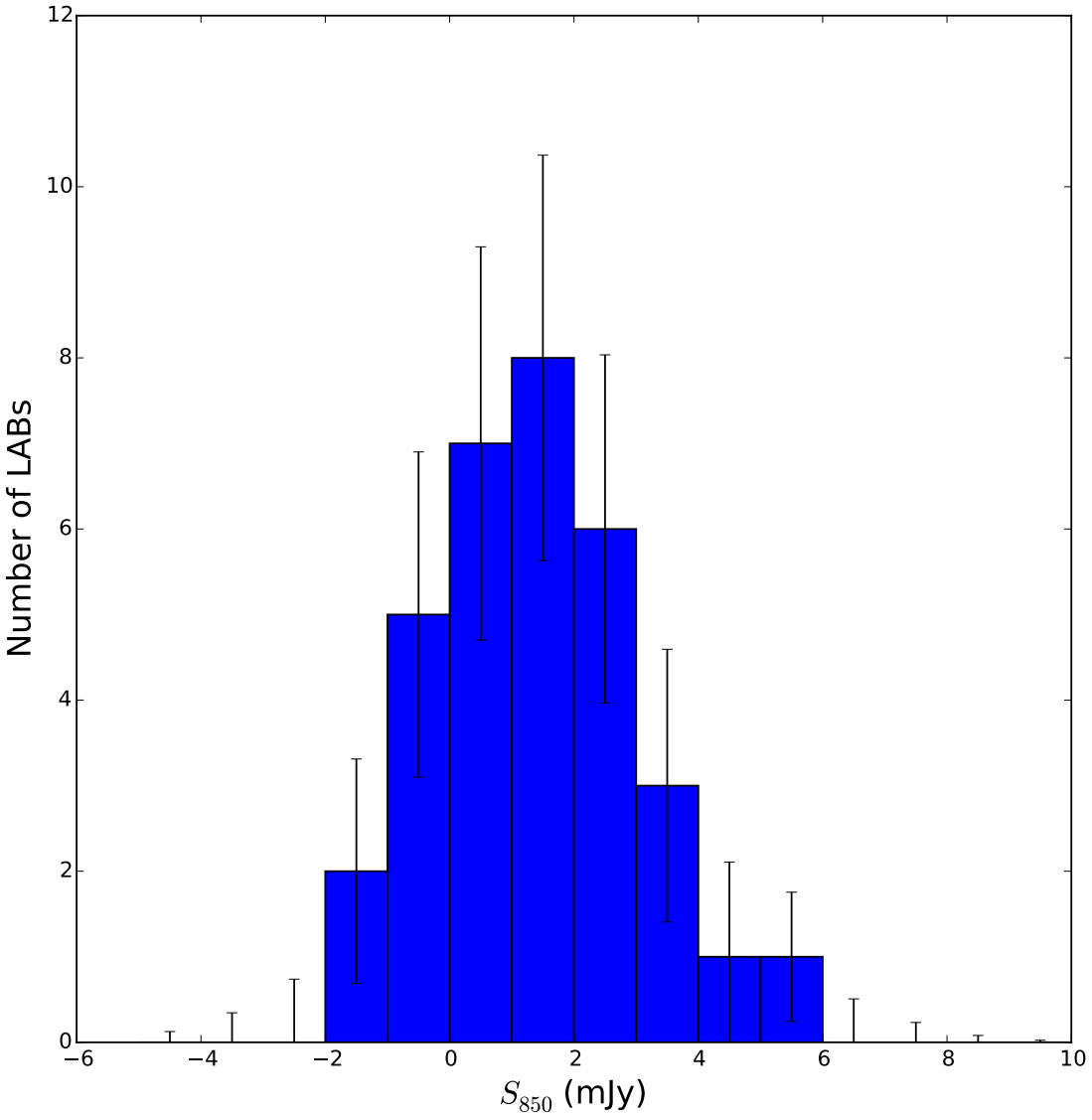

FIGURE 4.2: A histogram of the SCUBA-2 S_{850} values for all LABs. The error bars were calculated using Monte Carlo Sampling.

A correlation between the star formation rate (SFR) and L_{IR} is given in Kennicutt and Evans (2012) (see also Hao et al. 2011; Murphy et al. 2011).

$$\log(SFR_{IR}/M_{\odot}yr^{-1}) = \log(L_{IR}/ergs^{-1}) - 43.41 \tag{4.2}$$

A similar relationship between the intrinsic Lyα star formation rate ($SFR_{Ly\alpha i}$) and intrinsic Lyα luminosity ($L_{Ly\alpha i}$) can be obtained (equation 4.3) by combining the standard Case B $L_{Ly\alpha}$: Hydrogen-α luminosity ($L_{H\alpha}$) ratio (8.7, Brocklehurst 1971) and the Kennicutt and Evans (2012) $L_{H\alpha}$ to SFR correlation (equation 4.4, Dijkstra and Westra 2010):

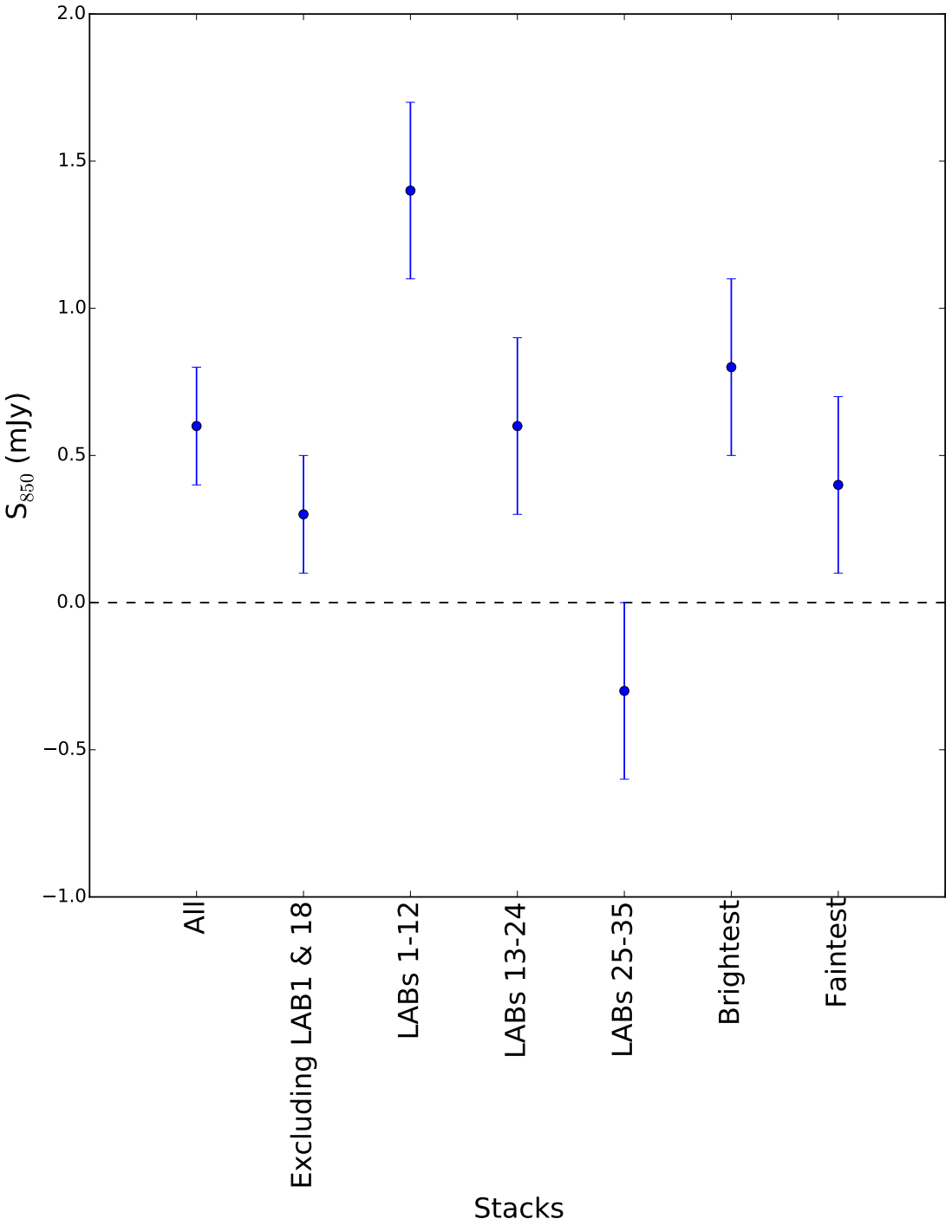

FIGURE 4.3: The SCUBA-2 S_{850} values for the key stacks are presented. The first two points illustrate the full stack with and without the two individual detections. The next three points relate to the LABs' size and the final points to the LABs' brightness. This illustrates the higher flux densities associated with the larger LABs.

$$\log(SFR_{\mathrm{Ly}\alpha}) = \log(L_{\mathrm{Ly}\alpha\mathrm{i}}/8.7) - 41.27 \tag{4.3}$$

$$\log(SFR_{H\alpha}) = \log(L_{H\alpha}) - 41.27 \tag{4.4}$$

which implies

$$L_{\mathrm{Ly}\alpha\mathrm{i}} \approx 0.06 \times L_{\mathrm{IR}} \tag{4.5}$$

This assumes L_{IR} scales linearly with S_{850}, all L_{IR} is from re-processed starlight (representing the majority of active star formation) and a Kroupa initial mass function (IMF, Kroupa and Weidner 2003).

To obtain the observed $L_{Ly\alpha}$ I must consider the fraction of Lyα photons that actually escape from the galaxy, f_{esc}, and the fraction of these photons that are then scattered by the CGM into our line of sight, f_{sca} (Geach et al., 2014).

$$L_{\mathrm{Ly}\alpha} \approx 0.06 \times f_{\mathrm{esc}} \times f_{\mathrm{sca}} \times L_{\mathrm{IR}} \tag{4.6}$$

In Fig. 4.4 (upper image) I plot $L_{Ly\alpha}$ against S_{850} for the individual LABs, the stacked LABs (All 34 LABs), the area stacks (large LABs, medium LABs and small LABs) and the two individually detected LABs (LAB1 and 18). I also indicate the theoretical position of LABs resulting from star formation processes, as calculated above, for a range of values of $f_{\mathrm{esc}}f_{\mathrm{sca}}$.

Hayes et al. (2011b) combined the results of a number of observational studies out to $z \sim 8$ to produce an expression for the evolution of the $L_{Ly\alpha}$ escape fraction with redshift, giving a range of values, 5 – 10 per cent at $z \sim 3$. This is in reasonable agreement with the Dijkstra and Jeeson-Daniel (2013) empirical constraint of the effective $L_{Ly\alpha}$ escape fraction at ~ 10 per cent for $z \sim 3$ – 4. These papers define the effective escape fraction as the ratio of observed to intrinsic $L_{Ly\alpha}$ and hence their figures includes both my f_{esc} and f_{sca}. I have plotted theoretical lines with $f_{\mathrm{esc}}f_{\mathrm{sca}}$ 0.02, 0.05, 0.1, 0.2 and 0.3. LAB18 can easily be fuelled with an effective escape fraction of 0.02, well below the values in the literature. This rather low value could be due to a more homogeneous gas distribution restricting the escape of Lyα, or higher levels of dust obscuring the emission. LAB1, the full stack and large LABs require a higher value of $f_{\mathrm{esc}}f_{\mathrm{sca}}$ 0.2-0.3, whilst the small and medium LABs could be produced with a lower value, closer to that in the literature. If the escape fractions in the literature are correct, this suggests that central star formation alone may not be sufficient to fuel the larger LABs.

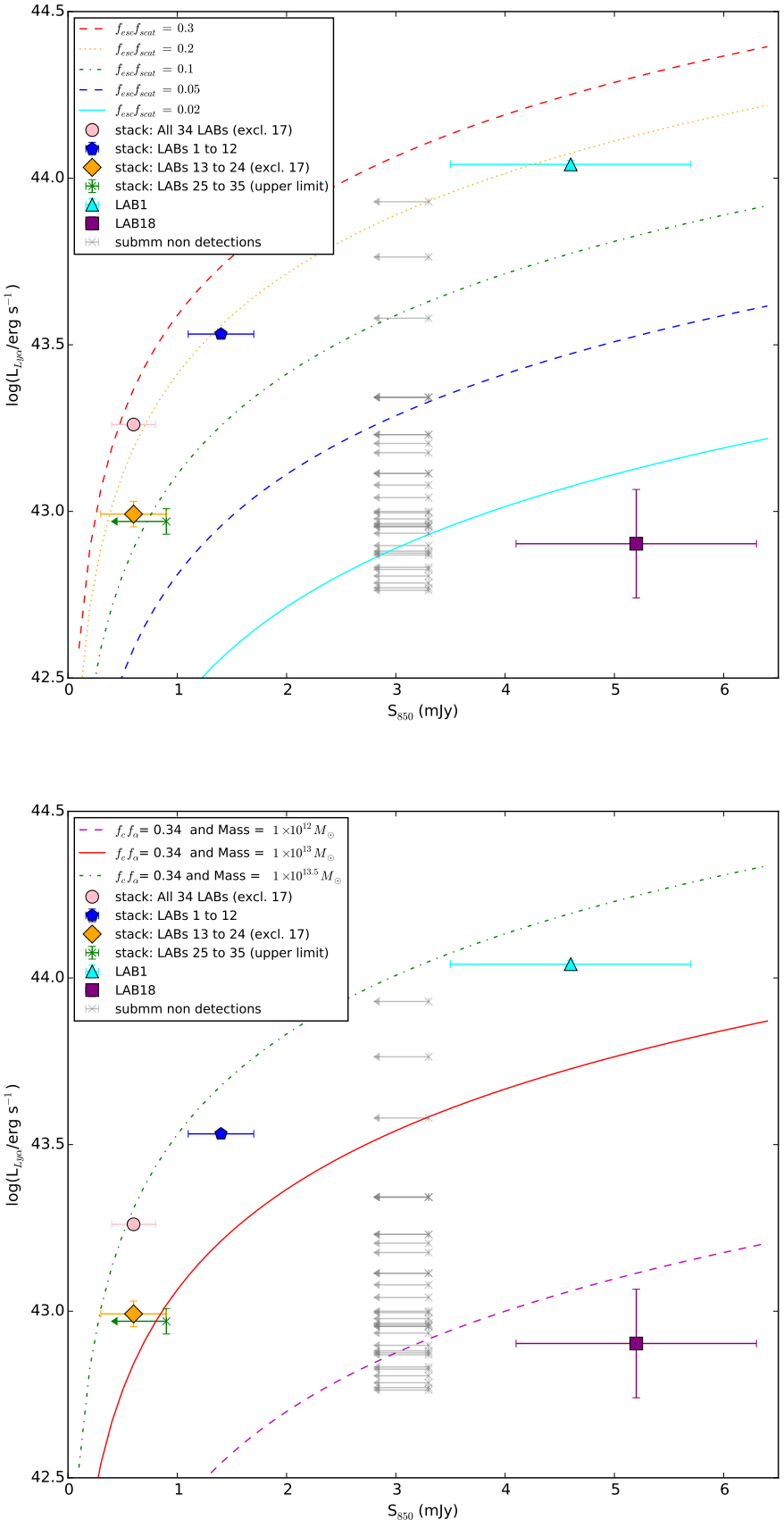

FIGURE 4.4: Log Lyα luminosity plotted against S_{850} for the full stack (pink circle), large LABs (blue pentagon), medium LABs (orange diamond), small LABs (green arrow upper limit only) and the two individually detected LABs, LAB1 (cyan triangle) and LAB18 (purple square). Non detections are shown as grey upper limits at 3 $\times$ rms. The lines in the upper image indicate the theoretical $L_{Ly\alpha}$-S_{850} relationship if the LABs are fuelled by star formation processes for a range of values of $f_{esc}f_{sca}$. In the lower image the lines indicate the theoretical $L_{Ly\alpha}$-S_{850} relationship if the LABs are fuelled by cold accretion, for a range of values of halo mass with $f_c f_\alpha = 0.34$.

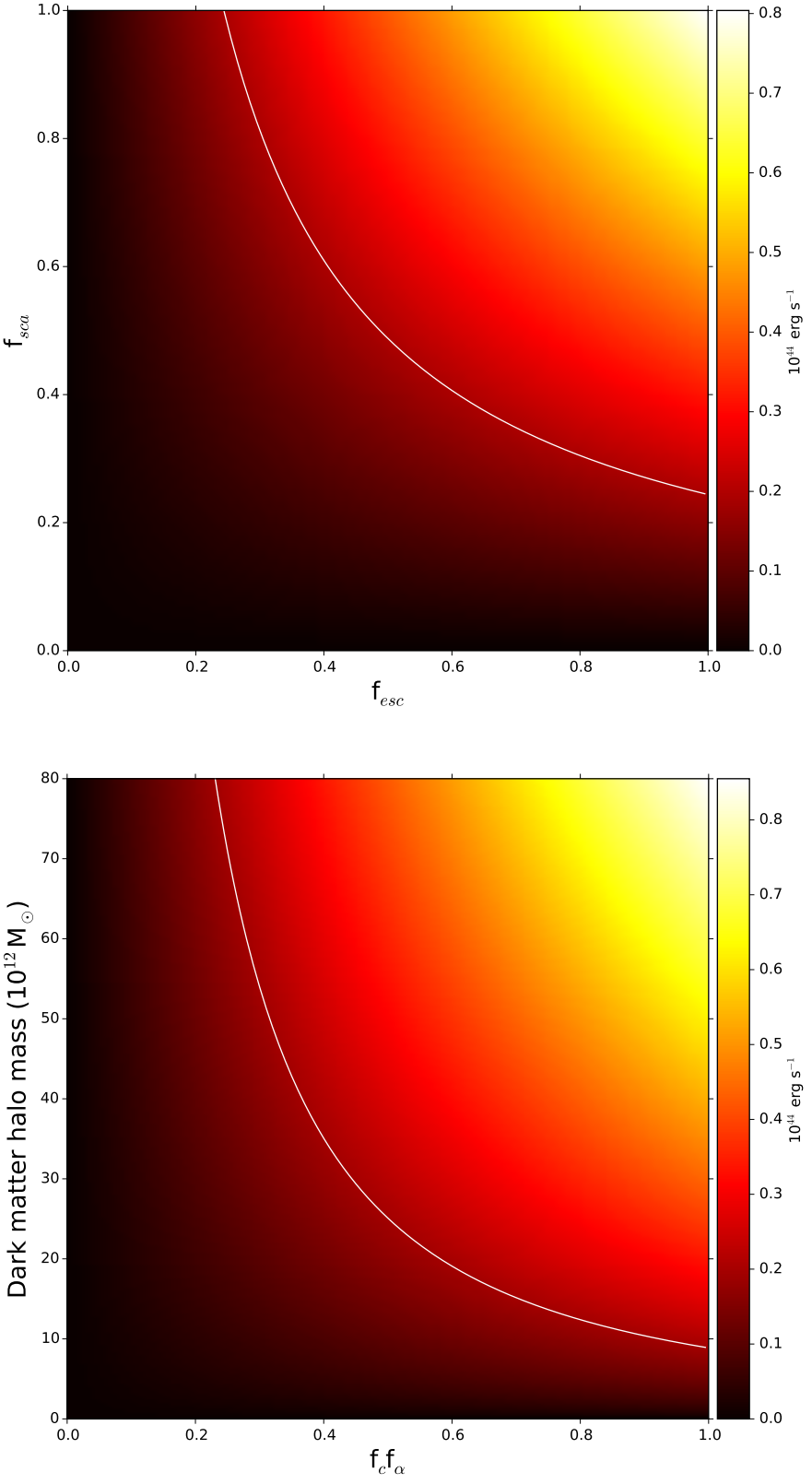

FIGURE 4.5: Upper: Colour maps showing how $L_{Ly\alpha}$ varies with f_{esc} and f_{sca} for the star formation model (upper) and $f_c f_\alpha$ and halo mass for the cold accretion model (lower), assuming S_{850} = 0.6mJy as obtained for the stacked LABs. The white line indicates the mean $L_{Ly\alpha}$ for all 34 LABs

Figure 4.5 (upper image) illustrates how $L_{Ly\alpha}$ (normalised to the S_{850} values obtained for the full stack) varies with f_{esc} and f_{sca} for a star formation model. The mean $L_{Ly\alpha}$ of all 34 LABs, $\sim 2 \times 10^{43}$erg s^{-1} (white line), can be obtained for a reasonable range of combinations of f_{esc} and f_{sca}. The implications of the results in this section are discussed further in Section 4.5.

4.4.2 Cold mode accretion

I calculated theoretical $L_{Ly\alpha}$ for the cold accretion mode based on the toy model in Goerdt et al. (2010). The gravitational energy released by the cold gas as it streams from the virial radius towards the centre of the halo is expressed as:

$$\dot{E}_{grav} = f_c \dot{M}_c \hat{\phi} V_v^2 \tag{4.7}$$

where $\dot{E}_{grav}$ is the gravitational power deposited in the cold gas at a given radius, r, per unit radial length, f_c is the fraction of the total power produced that heats the cold stream (rather than heating the hot virialized gas, or increasing the velocity of the infalling gas), $\dot{M}_c$ is the accretion rate of the cold gas, $\hat{\phi}$ is the gravitational potential at r, and V_v is the virial velocity.

Goerdt et al. (2010) considered an NFW potential well (Navarro et al., 1997), with a halo concentration parameter $C \approx 3$ ($C = \frac{r_v}{r}$) for a halo of mass 10^{12}M$_\odot$ at $z = 3$ (Bullock et al., 2001), resulting in $\hat{\phi} \approx 2.5$ as r $\rightarrow$ zero. For the purposes of my work I take the accretion rate to approximately equal the SFR, assuming that all the inflowing cold gas is converted to stars with no lag time. This gives:

$$\dot{E}_{grav} = f_c \times SFR \times 2.5 \times 236 \mathrm{km}^{-2} \mathrm{M}_{12}^{2/3} \tag{4.8}$$

where virial velocity ≈ 236 kms$^{-1} M_{12}^{1/3} (1+z)_4^{1/2}$ (Goerdt et al., 2010), $M_{12} \equiv M_v / 10^{12}M_\odot$ and $(1+z)_4 \equiv (1+z)/4$. A further parameter, f_α is added to represent the fraction of this energy emitted as observable Lyα radiation.

I used the Kennicutt and Evans (2012) SFR calibration for L_{IR} (equation 4.2) , which assumes a Kroupa IMF, to produce SFRs for the range of L_{IR} used in Section 4.4.1. In Fig. 4.4 (lower image) I plot theoretical lines for a 10^{12}M$_\odot$, 10^{13}M$_\odot$ and $10^{13.5}$M$_\odot$ dark matter halo (DMH) with $f_c f_\alpha = 0.34$. I used $f_c f_\alpha = 0.34$ as this was the value adopted by Goerdt et al. (2010) to obtain a reasonable fit to the observed LAB luminosity function (see section 4.5.3 for further discussion). As for the star-formation model, I also plot the individual LABs (pale grey), the stacked LABs (All 34 LABs), the area stacks (large LABs, medium LABs and small LABs) and the two individually detected LABs (LAB1 and 18). From the figure I see that LAB18 can

easily be produced with a relatively low mass DMH, whereas LAB1, the full stack and the large LABs require a halo approaching $10^{13.5}M_{\odot}$. The small and medium LABs could possibly be produced with a slightly lower mass DMH.

Fig. 4.5 (lower image) illustrates how $L_{Ly\alpha}$ (normalised to the S_{850} value obtained from the stack) varies with $f_c f_\alpha$ and halo mass for a cold accretion model. The mean $L_{Ly\alpha}$ of all 34 LABs, $\sim 2 \times 10^{43}$erg s^{-1} (white line), can only be obtained with a massive DMH, $> 3 \times 10^{13}M_{\odot}$, for $f_c f_\alpha, = 0.34$. The implications of the results in this section are discussed further in Section 4.5.

4.5 Interpretation and discussion

4.5.1 A summary of current detections in LABs

My results show that on average the larger LABs ($>$ 29 arcsec^2) are associated with submm emission, however there is no significant detection for the medium and small LABs. I summarise sources previously detected within the LABs in Table 4.3. X-ray detections in five of the LABs (Basu-Zych and Scharf 2004; Lehmer et al. 2009; Geach et al. 2009) indicate the presence of an AGN which could easily provide the power needed to produce LABs (Cantalupo et al. 2012; Prescott et al. 2015). Weak radio detections were reported for only two of the LABs (Chapman et al. 2004; Geach et al. 2005, G05), but these include LAB1, the largest and brightest LAB. IRAC detections in all four bands (Geach et al. 2007; Webb et al. 2009) have been obtained for 6 LABs, suggesting the presence of star forming, luminous galaxies hidden by dust. The two SCUBA-2 detections in my work also suggest the presence of dusty star forming galaxies. It is interesting to note that these luminous sources are only found in the larger LABs ($>$ 21 arcsec^2).

Table 4.3 also includes Lyman-break galaxies (LBGs, Steidel et al., 2003), the location of which within individual LABs was obtained from Matsuda et al. (2004). These, together with the K-band NIR galaxies (Uchimoto et al. 2008; Uchimoto et al. 2012; Erb et al. 2014; Kubo et al. 2015; Kubo et al. 2016) are common across all LABs, irrespective of size. Some of these *K*-band detections were associated with the LBGs, others were classified as Distant red galaxies (DRG). I also note two 1.1mm 3σ possible detections (Tamura et al., 2013). I calculated the expected flux density for 1.1mm observations based on my S_{850} = 0.6 mJy stack and the modified black body model used in Section 4.4.1 as 0.3 mJy. This is consistent with the stacked value of $S_{1.1mm}$ $<$0.40 mJy (3σ) reported in (Tamura et al., 2013). More recently (Umehata et al. 2015) have detected 1.1mm sources in LABs 12 and 14 (their deep ALMA observations were restricted to the central portion of the SSA22 protocluster).

TABLE 4.3: Summary of sources detected in SSA22 LABs based on published literature.

ID	X-ray ($L_{2-32keV}$)[a] 10^{44} erg s^{-1}	IRAC 3.6[b] μJy	IRAC 4.5[b] μJy	IRAC 5.8[b] μJy	IRAC 8.0 [b] μJy	SCUBA-2 [c] mJy	NIR [d] K_{AB}	Notes[e]
LAB1	<0.24	7.3±0.1	9.2±0.2	11.5±0.8	14.2±1.0	4.6±1.1	22.97±0.11 (DRG*)	Radio 21cm, MIPS
		8.4±0.1	11.1±0.2	14.7±0.8	15.9±1.0		23.34±0.11 (C11*)	LBGs (C11,C15)
							22.02±0.10	
							23.97±0.22	
LAB2	0.81±0.03	5.6±0.2	6.7±0.2	8.3±0.9	6.5±1.4	<3.9	22.91±0.11	LBG (M14)
		5.8±0.2	7.8±0.2	10.5±0.9	15.4±1.4	<3.9	(DRG, vicinity M14*)	
LAB3	2.13±0.02					<3.9	22.54±00.12 (DRG)	
LAB4	<0.56					<3.9		Radio 21cm
LAB5	<0.44	7.7±0.1	9.4±0.2	10.1±1.0	12.4±1.3	<3.9	<24.3	
LAB6		5.2±0.3	5.4±0.8	<9.0	<25.0	<3.9		
LAB7	<0.22	2.8±0.4	2.8±0.3	<7.0	<10.0	<3.9	23.49±0.12 (DRG, C6*)	LBGs (C6,M4)
							23.65±0.13 (M4*)	
							23.97±0.18 (C6*)	
LAB8	<0.20	2.6±0.1	1.0±0.2	<4.0	<5.0	<3.9	24.35 ±0.28 (C15*)	LBG (C15)
LAB9	<0.37	2.3±0.2	2.2±0.2	<5.0	<10.5	<3.9	<24.3	
LAB10						<3.9		
LAB11	<0.28	3.0±0.2	2.6±0.2	<5.0	<6.0	<3.9	23.79±0.17 (C47*)	LBG (C47)
							24.49±0.23 (C47*)	
							24.94±0.24 (C47*)	
LAB12	0.91±0.03	2.6±0.2	3.0±0.2	4.8±0.9	<6.0	<3.9	22.11±0.10	LBG (M28)
							23.67±0.21 (M28*)	$S_{1.1} = 0.7\pm0.1$ mJy U15
LAB13	<1.57					<3.9		
LAB14	1.82±0.02	7.4±0.1	10.6±0.2	15.0±0.8	19.6±1.1	<3.9	22.45±0.11 (DRG)	$S_{1.1} = 1.8\pm0.1$ mJy
								U15 (3σ, T13), MIPS
LAB15	<0.87	1.7±0.3	1.8±0.3	<12.0	<8.0	<3.9		
LAB16	<0.36	5.8±0.1	7.3±0.2	9.6±1.1	15.2±1.5	<3.9	22.99±0.11	MIPS
							23.51±0.19	
LAB17								
LAB18	1.59±0.03	7.3±0.2	8.7±0.3	15.7±1.5	19.2±1.6	5.2±1.1		MIPS, 1.1mm (3σ, T13)
		4.9±0.2	7.8±0.3	8.6±1.5	17,6±1.6	<3.9		
LAB19	<0.36	2.8±0.1	2.4±0.2	<4.0	<5.5	<3.9	<24.3	
LAB20	<0.22	1.3±0.2	<1.0	<4.0	<7.5	<3.9	23.3±0.11 (C12*)	LBG (C12)
LAB21	<2.84					<3.9		
LAB22	<0.56	<3.0	<2.0	<6.0	<8.0	<3.9		
LAB23		<1.5	<4.0	<13.0	<27	<3.9		
LAB24	<0.39	<0.8	<1.0	<5.0	<7.0	<3.9	23.36±0.13 (DRG)	
LAB25	<0.23	1.2±0.1	2.4	<4.0	<8.0	<3.9	<24.3	
LAB26	<0.23	<1.0	<1.0	<5.0	<10.0	<3.9	<24.3	
LAB27	<0.97					<3.9	<24.3	
LAB28	<0.99					<3.9		
LAB29		3.6±0.3	<4.0	<8.0	<24.0	<3.9		
LAB30	<0.27					<3.9	22.96±0.11 (D3*)	LBG (D3)
							23.51±0.19	
LAB31	<0.23	1.1±0.3	<1.5	<6.0	<8.0	<3.9	23.20±0.11	
LAB32	<0.47					<3.9		
LAB33	<2.08	1.8±0.2	2.1±0.3	<10.0	<10.0	<3.9		
LAB34		1.8±0.2	<2.0	<6.5	<13.5	<3.9		
LAB35	<0.27	1.4±0.2	1.4±0.2	<4.5	<6.0	<3.9	<24.3	

a) Luminosities taken from Geach et al. (2009), originally reported in Lehmer et al. (2009), first detection of LAB2 in Basu-Zych and Scharf (2004).
b) IRAC flux densities taken from Webb et al. (2009), original detections for LAB1,2 in Geach et al. (2007), further information on LAB1 in Geach et al. (2014). Some LABs contain more than one source.
c) This work.
d) AB magnitudes from Uchimoto et al. (2012) (many originally detected in Uchimoto et al. (2008)). Uchimoto et al. (2012) used a 6″ radius and a combination of photometric redshifts and Lyman-α spectroscopic redshifts (z_{spec}) of probable K-band counterparts to identify LAB sources (* indicates z_{spec} was provided in. Uchimoto et al. (2012)). In some cases there are multiple possible K-band counterparts for a single LBG. Where no LAB counterpart was detected by Uchimoto et al. (2012) an upper limit is quoted. DRG stands for Distant Red Galaxy. Uchimoto et al. (2012) covered only 20 of the LABs, there is currently no information available for the other 15. NIR z_{spec} were later obtained for the counterparts of LABs 1,12,12 30 and 35 (Erb et al., 2014; Umehata et al., 2015) and for these LABS these values are used to determine membership of the protocluster.
e) LBGs are listed together with their ID numbers from Steidel et al. (2003), their positions within the LABs are taken from Matsuda et al. (2004) Geach et al. (2007) and Radio 21cm detections from Chapman et al. (2004) and Geach et al. (2005). 1.1mm detections are from Tamura et al. (2013).

The LBGs are not present in all LABs and therefore could not explain the observed Lyα emission in all cases. Furthermore, the observed relationship between the L_{IR} to L_{UV} ratio and the UV spectral slope, β, (Meurer et al. 1999; Heinis et al. 2013; Álvarez-Márquez et al. 2015) suggests that the contribution form infrared sources will dominate that from LBGs.

The detections summarised above provide strong evidence that the larger LABs contain star-forming galaxies, or AGN, that could produce, or at least significantly contribute to the observed LABs. The case for the smaller LABs is less convincing, as these do not contain such powerful counterparts. This split is consistent with my results from stacking by area and suggests that

there may be two populations. It could be that the largest LABs are composed of multiple overlapping smaller LABs resulting from multiple sources. However, I should also note that the larger area of the large LABs group may increase the likelihood of chance alignment.

In addition, not all LABs have been observed at all wavelengths and deeper observations may reveal previously undetected sources in those that have. The upper limits for X-ray observations are generally low enough to make it unlikely that future observations would reveal an AGN, however LAB33 has an upper limit of 2×10^{44} erg s^{-1} allowing scope for a future detection. AGNs could also be obscured by dust (Geach et al., 2009), however the lack of IRAC 8μm detections in the smaller LABs makes this unlikely. The upper limits on IRAC and submm observations do allow for future detections and ALMA observations would help to confirm the presence or otherwise of any dusty star forming galaxies in the smaller LABs and of multiple sources in the larger LABs.

4.5.2 Further exploration of powering mechanisms

I explored two options for powering the LABs in Section 4.4. I found that the full stack could be produced via star formation with $f_{\rm esc}f_{\rm sca}$ = 0.2-0.3, or via cold accretion for a relatively massive halo ($\sim 10^{13.5} M_{\odot}$) with $f_c f_\alpha = 0.34$. A value of $f_{\rm esc}f_{\rm sca}$ = 0.2 (0.3) implies that 20 per cent (30 per cent) of the Lyα emitted within a central galaxy is able to escape from the galaxy and is then scattered by the CGM into our line of sight. This value is higher than the figure of 0.1 typically found in the literature (Hayes et al. 2011b; Dijkstra and Jeeson-Daniel 2013), but these figures generally apply to LAEs. For LAEs any scattering takes place close to the galaxy, however, in the case of LABs, scattering is occurring over an extended region and a higher value of f_{sca} is therefore plausible. There is also some variation in escape fraction values in the literature. Wardlow et al. (2014) found a significantly higher range of values, with lower limits of 0.1-0.3 depending on the SED used to fit their LAEs. Geach et al. 2009 found that a value as low as 0.006 was sufficient to power the LABs containing AGN. However, if their Figure 4 were recreated using my SCUBA-2 results, this would result in a higher escape fraction, which is more in line with my results. In order for Lyα to escape from the central galaxy there must be a relatively low covering fraction (Steidel et al. 2011; Trainor et al. 2015). However, sufficient cold gas is also required in the CGM in order for scattering to take place. This suggests the need for an irregular, patchy CGM (Steidel et al., 2010), in line with predictions from recent simulations (van de Voort et al. 2011; van de Voort and Schaye 2012; Rosdahl and Blaizot 2012). The dark-matter halo function obtained from simulations (Springel et al. 2005; Lukić et al. 2007; Martinovic 2015), suggests that a $\sim 10^{13.5}$ M$_{\odot}$ DMH is rare at $z \sim 3$. Whilst such a massive DMH might be possible for some of the LABs (e.g LAB1) it is not possible for all LABs to exist in such massive DMHs. Thus my cold accretion model appears to require more extreme conditions than the star formation model and I suggest that, on average, star formation

is more likely to be the dominant process. Additional contributions from cold accretion and AGN are also likely for some individual LABs.

LAB18 is relatively easy to produce via either process, but LAB1 requires more extreme conditions; either a high mass halo or a higher value of $f_{\rm esc}f_{\rm sca}$ than proposed by (Hayes et al. 2011b; Dijkstra and Jeeson-Daniel 2013). In fact, as can be seen from Table 4.3, LAB1 contains multiple galaxies and a radio source. It is therefore likely that this LAB is the result of more than one process and a higher value of $f_{\rm esc}f_{\rm sca}$ may not be required to explain the observed emission.

The results for the large LABs stack are similar to those for the full stack, though not quite as extreme. The value of $f_{\rm esc}f_{\rm sca}$ = 0.2 is more achievable than the extremely massive dark matter halo that is required under the cold accretion model. This makes star formation more likely to be the dominant process for the large LABs, although contributions from other processes may also be required. The results for the medium and small LABs require a lower $f_{\rm esc}f_{\rm sca}$, consistent with the literature and so these smaller LABs could be produced from star formation without contributions from other sources. However, they also require a lower mass DMH ($\sim 10^{13}$ $M_{\odot}$) than other stacks and therefore this scenario is also possible.

Our results indicate a significantly lower mean S_{850} than G05. This implies a smaller chance of finding submm sources in all LABs and lower SFRs ($\sim$50 $M_{\odot}yr^{-1}$ rather than $\sim 10^3$ $M_{\odot}yr^{-1}$). However, my analysis still favours central star formation over cold accretion as the primary fuelling method. G05 considered the superwind model rather than the two models discussed in this thesis. I have not repeated this aspect of their work as alternative models involving scattering are now considered more likely (Hayes et al. 2011c; Geach et al. 2014). G05 found a trend between the $L_{Ly\alpha}$ of the haloes and submm flux, but I find only a marginal correlation to luminosity and a much higher correlation to the size of the LABs.

4.5.3 Underlying assumptions

I now consider some of the assumptions made in applying these models. In my star formation model I assume a dust temperature of 30K which compares to an average measured value for submm galaxies of 30-40K (Casey et al., 2014). I tested the sensitivity of my work to dust temperature by increasing the temperature to 40K and found that this increased the L_{IR} by $\sim 4 \times 10^{45}$ erg s^{-1}. Such an increase allows LAB1, the full stack, and large LABs to be created with $f_{\rm esc}f_{\rm sca}$ = 0.05 - 0.1, in line with values in the literature. I also varied the value of β in my model (usually found to be in the range 1-2 in starburst galaxies (Hildebrand 1983; Chapin et al. 2011; Casey et al. 2014). For a value of β =1 (and 30 K) L_{IR} is decreased by $\sim 1 \times 10^{45}$ erg s^{-1}, requiring $f_{\rm esc}f_{\rm sca} > 0.3$ to generate LAB1 the full stack and large LABs. It is therefore possible that with a high dust emissivity and temperature, the star formation model could account for

all the Ly-α emission observed in the LABs. However, a lower value of β together with a low temperature make the star-formation model less likely as the sole source of emission.

The value of C used to compute the cold accretion Lyα values in section 4.4.2 is based on the Bullock et al. (2001) formula, $C \approx 3M_{12}^{-0.13}(1+z)_4^{-1}$, which results in $C \approx 3$ for a halo mass of 10^{12}M$_\odot$ at $z = 3$. However, a more massive halo may be required to produce the LABs by cold accretion. Assuming a halo mass of 10^{13}M$_\odot$ results in a revised value of $\hat{\phi} \approx 2.2$. Re-plotting Fig. 4.4 using this revised value of $\hat{\phi}$ had no significant impact on my conclusions. I also assume that the accretion rate is approximately equal to the SFR. If only a proportion of the accreted gas produces stars then I am underestimating the accretion rate in my model and therefore underestimating the production of Lyα emission due to cold accretion. This could allow for the production of LAB1 and the stack with a lower halo mass.

The value of $f_c f_\alpha$ (the fraction of gravitational power released that heats the cold streams $\times$ the fraction of energy emitted as observable Lyα emission) used in the cold accretion model is also uncertain. I use 0.34 as this was the value adopted by (Goerdt et al., 2010) to obtain a reasonable fit to the observed LAB luminosity function. However, in the same paper, a figure of f_α = 0.85 is used for their hydrodynamic simulations. This would require f_c = 0.4 if applied to the toy model, but Goerdt et al. (2010) suggest elsewhere that $f_c \sim 1$. There is disagreement in the literature as to whether the infall velocity of the cold streams is close to free fall, giving a value of $f_c \sim 0$ (Rosdahl and Blaizot 2012; Faucher-Giguère et al. 2010), or whether the velocity is largely constant for all radii, giving $f_c \sim 1$ (Goerdt et al. 2010; Goerdt and Ceverino 2015). Rosdahl and Blaizot (2012) found f_c between 0 and 0.3 in Adaptive Mesh Refinement zoom simulations, with a higher value in messy streams in low mass haloes. By contrast, the Goerdt and Ceverino (2015) simulations indicated a constant velocity in low mass haloes and only a slight increase in velocity for higher mass haloes ($>5 \times 10^{12}$ M$_\odot$). If I were to use a maximum value of $f_c f_\alpha = 1 \times 0.85 = 0.85$ in Fig. 4.4, LAB1 and the full stack could be produced with a halo mass of 10^{13}M$_\odot$, still massive, but less extreme than required with $f_c f_\alpha = 0.34$. Given the large uncertainties in the submm flux LAB1 could potentially be fuelled in a 10^{13} M$_\odot$ halo with $f_c f_\alpha$ as low as 0.55, but this would not produce the flux seen in the stack or large LABs.

The non detection of a submm source does not necessarily rule out the presence of a luminous galaxy. A luminous source could be obscured by dust in cold clumpy gas, which would not be observable from some orientations.

Finally, I note that in both scenarios cold gas is required outside the galaxies in order to scatter the Lyα into our line of sight. Therefore, even if the Lyα emission is fuelled primarily by star-formation processes, the observed LABs are still evidence of the presence of cold gas in the CGM. In addition the high value of $f_{esc}f_{sca}$ implied suggests that a clumpy configuration is more likely than narrow streams in the CGM and requires inhomogeneous HII regions within the galaxy powering the LAB (Haiman and Spaans, 1999).

4.6 Conclusions

I used SCUBA-2 CLS data to search for SMGs in the SSA22 LABs, investigating both individual detections and the mean stack. I then compared my results to two potential mechanisms for fuelling LABs, central star formation and cold accretion. My findings are as follows:

- Two of the LABs had SCUBA-2 detections at $> 3.5\sigma$, LAB1 (4.6±1.1mJy) and LAB18 (5.2±1.1mJy).
- My mean stacking of all 34 LABs resulted in an average flux density of 0.6±0.2mJy at 3.1σ. This implies that, on average, each LAB contains a dusty, star forming galaxy and that star-formation processes are at least partly responsible for fuelling the LABs.
- My stacking of the LABs based on their size suggests that the larger LABs are marginally more likely to contain a submm source ($S_{850} > 1$mJy) than the smaller LABs. A review of the literature suggests that luminous sources can be found in most of the larger LABs (LABs 1–18), but are missing from the smaller LABs. Whilst future observations may change this picture, it is possible that there are two populations of LABs, large LABs created by luminous sources (galaxies or AGN) and smaller LABs containing less luminous galaxies, or fuelled solely by cold accretion.
- My investigation of two possible fuelling processes suggests that central star formation is more consistent with being the dominant source of the Lyα emission than cold accretion. However, given the uncertainty in $f_c f_\alpha$ and $f_{\rm esc} f_{\rm sca}$, neither process can be ruled out and it is likely that both processes are involved to some extent in most LABs.

Deeper data from the Atacama Large Millimeter/submillimeter Array (ALMA) are required to detect individual SMGs in the LABs and place further constraints on the fuelling processes.

Chapter 5

Further discussion and conclusions

In this thesis I have investigated the impact of a high density environment on the evolution of galaxies using the SSA22 z =3.1 protocluster. In this final Chapter I set out my key conclusions, review progress made since completing my work described in earlier chapters, and look ahead to future research that could address some of the remaining questions. I first consider the need for improved simulations, then discuss the SSA22 protocluster LBG population, the LABs and gas dynamics within galaxies and in the circumgalactic medium (CGM), and finally the wider population of protoclusters.

5.1 The role of simulations

To help understand the impact of the protocluster environment on galaxy evolution, I need to develop a high-resolution hydrodynamic simulation of a protocluster, which can then be compared to observations. Simulations have been used to trace the evolution of large samples (1000s) of clusters (e.g., Chiang et al., 2013; Muldrew et al., 2015). These are semi-analytic simulations based on the Millennium Simulation, tracing the evolution of of $z = 0$ clusters (Mass $\gtrsim 10^{14}$ $M_\odot$) out to their high-redshift progenitors. They are able to trace the mass of galaxies ($>10^8 M_\odot$) and dark-matter halos, but they do not have sufficient resolution to study features within galaxies (particle masses $\sim 10^8$ $M_\odot$) and cannot trace gas in either the CGM or lower mass galaxies. Saro et al. (2009) used the Zoomed Initial Condition (ZIC, Tormen et al., 1997) approach to create high resolution ($\sim$2 kpc, gas particle mass $\sim 10^7$ $M_\odot$) hydrodynamic simulations of two protoclusters at $z \sim$2.1 ($\sim 10^{14}$ $M_\odot$ and $\sim 10^{15}$ $M_\odot$) and compare them to the Spiderweb protocluster (z =2.16). ZIC works by tracing all the hydrodynamic particles in a $z = 0$ cluster (in the original low resolution cosmic simulation) back to the initial conditions and replacing each particle with several lower-mass particles. These new particles are then perturbed according to

the density fluctuations used in the original simulation plus additional higher-frequency density fluctuations. The Saro et al. (2009) simulations were hydrodynamic and reasonably high resolution, but lacked radiative transfer of Lyα emission and so could not be used to trace gas dynamics in galaxies in the CGM.

To make further progress in my investigation of the SSA22 protocluster I need a zoom hydrodynamic protocluster simulation with radiative transfer, this will allow me to probe both the physical properties of galaxies and the gas dynamics within the galaxies and in the CGM. This could be achieved using the ZIC technique, selecting a galaxy cluster, similar in mass to the predicted $z = 0$ mass of SSA22, from an extremely large, low-resolution parent simulation and re-simulating with radiative hydrodynamics at $\sim$kpc spatial resolution. A currently running EAGLE (The Evolution and Assembly of GaLaxies and their Environments, Schaye et al., 2015; Crain et al., 2015) simulation ($L = 800$ Mpc, baryon particle mass $=10^6$ M$_\odot$) would be ideal for this (R. Crain, private communication). I will seek to simulate on a scale of several 1000 hydrodynamic particles per 10^8 M$_\odot$ galaxy. I will use SKIRT-RT (Camps & Baes, 2015) to simulate UV/optical attenuation and IR re-emission/scattering and the TLAC Lyα RT code (Gronke et al. 2014, 2015) to simulate Lyα emission. TLAC is a Monte Carlo code that traces the path of photon packets through real and frequency space, using an algorithm to determine whether each packet interacts with gas or dust and how it is absorbed or scattered. When photon packets escape the simulation domain, their frequency and other properties are recorded and the combined frequency of all such packets produces the Lyα spectra.

I will use the simulation to predict:

- Gas dynamics within galaxies and in the CGM. Section 5.3.2 explores how observations of Lyα emission, the [OII] emission line and the CO(4-3) line can be used to compare to the simulated multiphase gas dynamics.
- The role of mergers in the assembly of the protocluster. In section 5.2.1 I consider how the simulation can be combined with multiwavelength observations of LBGs to explore the role of mergers versus gas accretion in the build up of stellar mass in the protocluster.
- Physical properties of protocluster galaxies (e.g. mass, age, SFR). In section 5.2.2 I explore approaches to obtaining reliable physical properties for the LBGs in my protocluster sample. These could then be used to compare to the simulated properties to aid my understanding of protocluster galaxy evolution.

By simulating observations and comparing directly to real observations (as discussed below), I will be able to further refine the simulation and the theoretical assumptions on which it is based.

5.2 Accelerated galaxy evolution in protocluster environments

In Chapters 2 and 3, I studied the LBGs in the SSA22 protocluster, looking for evidence of accelerated evolution compared to field LBGs. I found that there was a marginal enhancement of the merger fraction, but no indication of a difference in stellar mass. About 60% more protocluster LBGs were undergoing mergers, compared to the field sample, suggesting that mergers may play an important role in driving galaxy growth within protoclusters. The dense environment appears to cause more frequent mergers than in less-dense regions, as predicted by existing simulations. However, there is no evidence that this has led to an increase in the average mass of LBGs. It may be that the LBG population will become more massive than the field at a later epoch. It is also possible that other galaxy populations may already have accumulated an enhanced mass. Massive red galaxies (rare at this redshift) have been observed, particularly at the centre of the protocluster (Kubo et al., 2015), might these have been detectable as LBGs at an earlier time? My picture of protocluster galaxies is still incomplete and further observations are required. The work in this thesis could naturally be extended in a number of ways as explained in the following two sections.

5.2.1 Mergers

My work on merger fractions used rest-frame UV data and I suggested in Chapter 2 that repeating the experiment with rest-frame optical *HST* data would allow me to confirm (or otherwise) the presence of an enhanced merger fraction. As existing archive $F160W$ data covers all of the HDF-N LBG sample and 17 LBGs in the SSA22 protocluster this would require obtaining further observations to complete the SSA22 sample. I have since analysed the existing $F160W$ data covering the 17 LBGs and classified them according to my original scheme. Of the 14 LBGs for which I have data in both wavebands, nine have the same classification in $F814W$ and $F160W$, but five have changed from mergers in $F814W$ to non mergers in $F160W$. Whilst this may be in part due to genuine differences in emission at the two wavelengths (rest-frame UV light traces star formation whereas rest-frame optical traces older, less-massive stars), it is clear that part of the change in classification is due to the lower resolution of the $F160W$ data. This means that what appear as separate cores in the $F814W$ images are blended to appear as one source in the $F160W$ images, see Fig. 5.1. My method of classifying galaxies as mergers or non mergers may not be appropriate for the $F160W$ images. Looking ahead, the James Webb Space Telescope could potentially be used to obtain deeper images suitable for this type of analysis (launch planned for 2018).

A more reliable method of confirming my merger fraction would be to obtain optical and NIR IFU spectroscopic observations of the LBG samples. I might expect to see two sources of emission with a velocity offset for merging systems (Nesvadba et al., 2008), and could therefore

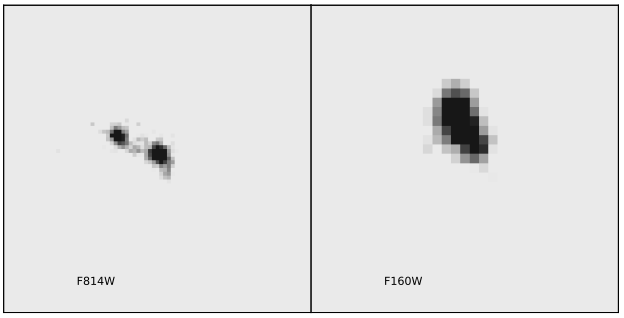

FIGURE 5.1: On the left is an $F814W$ image of an LBG. Two separate cores are visible, indicating a merger. The right hand image shows the same LBG in $F160W$. The lower resolution means that the cores are blended, this would be classified as a non merger using my definition. Both images are $4'' \times 4''$, they are not registered.

obtain a more reliable merger fraction. However, to cover both samples in full would require a significant amount of observing time. Obtaining observations of a sub sample, to check the reliability of my method of classification may be more realistic.

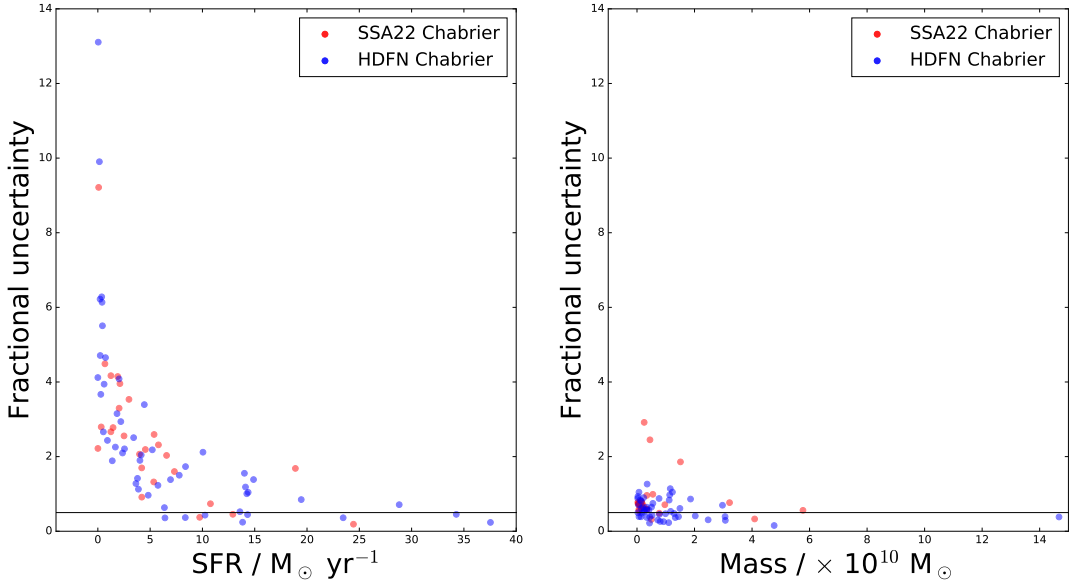

FIGURE 5.2: Fractional uncertainties (uncertainty/parameter) for SFR (left) and mass (right) obtained from my CIGALE fitting using the Chabrier model. Blue circles indicate the HDFN LBG sample and red circles the SSA22 protocluster sample of LBGs. The black line indicates an uncertainty of half the parameter value. The fractional uncertainties related to the SFR values are significantly higher than those for mass.

This work could then be extended by using the zoom simulation described above to address the question of whether mergers (and merger triggered star formation), or star formation from cold gas accretion contribute the most to the build up of stellar mass. Using multiwavelength SED fitting to obtain SFRs for the LBGs in my sample, I could compare the merger rate and SFRs from the simulation to those obtained from observations. For this to be an effective experiment I would need to obtain SFRs with uncertainties significantly lower than those obtained in my CIGALE fitting in Chapter 3. Although I was primarily interested in the mass of the LBGs, I

also obtained SFRs, but these had uncertainties significantly larger than those obtained for the masses, see Fig. 5.2. Only $\sim$6% of the SFR values have fractional uncertainties of less than 0.5, compared to $\sim$36% for mass. In addition the maximum SFR fractional uncertainty is $\sim$13 whereas the maximum for the mass values is $\sim$3. In section 5.3 I discuss the possibility of improving the SED fitting.

A recent survey by Topping et al. (2016) obtained additional spectroscopic redshifts for LBGs in the SSA22 protocluster, bringing the total number of LBGs with confirmed redshifts within the 3.06 - 3.12 range to 40. The details of these additional LBGs are not yet publicly available, but this does raise the possibility of increasing my sample size, although this would still be below the 70 required for a 3σ measurement (see Chapter 2). Such an extension of this work would only be possible if *HST* imaging were available for these additional sources and so I would propose to observe any that were not covered by archive data.

5.2.2 Physical properties

The zoom simulation, described in section 5.1, could be used to predict observable physical properties within the protocluster, and these could then be compared to actual observations. As illustrated in Fig. 5.2, the uncertainties on many of the physical properties derived from my SED fitting are high and I would aim to improve on these results further before making my comparisons. Further reducing the uncertainties on the mass values would also allow me to confirm my conclusions regarding the lack of a mass enhancement in the protocluster. However, obtaining more precise physical parameters is not necessarily a straightforward process.

I could potentially improve the SED fitting results by obtaining photometry at longer wavelengths, as this would allow me to constrain the FIR peak of thermal cold dust emission and address the age-dust degeneracy referred to in Chapter 1. Although observations exist at longer wavelengths (e.g. SCUBA-2, *Herschel Space Observatory*) it is hard to obtain photometry that is suitable for SED fitting as the large beam size causes problems with confusion. Bourne et al. (2017) have recently demonstrated that TPHOT (see Chapter 3) can be used to obtain photometry from SCUBA-2 data. In addition the XID+ code can be used to obtain photometry from *Herschel* SPIRE maps (Hurley et al., 2017). The use of these prior based codes could help to obtain usable photometry to constrain the FIR SED. A better option would be to use submm interferometers, such as ALMA. Koprowski et al. (2016) obtained ALMA observations of 5 of the protocluster LBGs and detected one at 3σ. As expected I found that using the ALMA photometry for this one LBG made no significant difference to the derived mass, however, it also had no significant impact on age or dust extinction , which is more surprising given the dust-age degeneracy. It would be interesting to see if obtaining ALMA coverage for the rest of the LBG sample has any impact on the fits.

The uncertainties on the CIGALE physical parameters are mainly dependent on the errors on the input photometry, although the number of degrees of freedom (number of filters - 1) also has some impact. Increasing the degrees of freedom (by adding another filter) should lead to a decrease in the uncertainty, although this may not be the case if the available models are not a good fit to the data. Improving the photometry of existing wavebands should also lead to smaller uncertainties. However, the authors of CIGALE recommend a minimum error of 5% on input photometry due to systematic errors arising from the limitations of the models and the potential issues involved in using errors evaluated by different methods for different instruments. Small errors for certain wavebands may cause systematic offsets between those and other wavebands, leading to incorrect fits. Finally, it may also be possible to obtain better fits by improving the models. This could be attempted both by using the recent update to CIGALE, which has improved nebular models, and by considering the use of other SED fitting codes (e.g. MAGPHYS, da Cunha et al., 2008).

The additional protocluster LBGs identified by Topping et al. (2016) could also be added to my analysis assuming they are covered by existing observations.

5.2.3 LBG Summary

In Table 5.1, I present a summary of the known properties of my SSA22 LBG sample, based on my work in this thesis and a review of the literature. This includes the SCUBA2 and ALMA submm counterpart detections summarised in Chapter 4 and later in this chapter. The limited submm coverage and large uncertainties on some of the mass values make it difficult to draw any definite conclusions, but it is worth noting the following:

- The two LBGs that are also thought to be AGN are compact non mergers, and are also the most massive LBGs in the sample (my masses are consistent with those found for AGN in the protocluster by Lehmer et al. (2009)). These LBGs may have undergone a recent merger, resulting in an increase in mass and then become active at some point after the two cores had coalesced.

- There is no correlation between the detection of a submm source and galaxy morphology, but the three submm sources are all relatively high mass (although the mass value for C11 has very large uncertainties and so is not reliable). It may be that the submm sources are higher mass due to having higher SFR and/or being post merger, however with incomplete ALMA coverage it is too soon to draw any definite conclusions.

- All the high mass LBGs ($\geq 10^{10} M_{\odot}$) are either mergers or contain an AGN or luminous submm source. This suggests that higher mass can be driven by mergers, or by the higher

TABLE 5.1: A summary of the SSA22 LBG population used in this work.

ID[a]	Merger[b]	AGN[c]	LAB[d]	SMGs[e]	Mass[f] $Log_{10}(M/M_{\odot})$
SSA22a-C4	m*	-	-	-	8
SSA22a-C6	m*	-	LAB7	-	9
SSA22a-C11	m	-	LAB1	SCUBA2	9***
SSA22a-C12	c	-	LAB20	-	8
SSA22a-C15	c	-	LAB1,8	-	9
SSA22a-C16	m	-	-	ALMA	10
SSA22a-C24	m	-	-	-	9
SSA22a-C27	m	-	-	-	10 **
SSA22a-C28	c	-	-	-	9
SSA22a-C30	c	-	-	-	8
SSA22a-C35	m	-	-	-	9
SSA22a-C36	m	-	-	-	10
SSA22a-C39	m	-	-	-	8
SSA22a-C48	c	-	-	-	8
SSA22a-C50	c	-	-	SCUBA2	10
SSA22a-D3	c	-	LAB30	-	9***
SSA22a-D12	c	Yes	-	-	11
SSA22a-D17	c	-	-	-	9
SSA22a-M4	N/A	-	LAB7	-	9
SSA22a-M10	m	-	-	-	10
SSA22a-M14	c	Yes	LAB2	-	10
SSA22a-M28	c*	-	LAB12	-	9
SSA22a-MD14	m	-	-	-	9
SSA22a-MD23	c	-	-	-	9 **
SSA22a-MD32	m	-	-	-	9
SSA22a-MD46	m	-	-	-	8
SSA22b-D9	c	-	-	-	9**
SSA22b-C5	N/A	-	-	-	8

a) IDs are taken from Steidel et al. (2003).
b) m indicates a merger and c a non merger based on my $F814W$ analysis in Chapter 2.
* indicates that there were no $F814W$ data available and the analysis is based on $F160W$ imaging.
Two LBGs had no coverage in either *HST* band and these are indicated by N/A.
c) Identification from Lehmer et al. (2009)
d) Association with a LAB taken from Matsuda et al. (2004)
e) SCUBA2 identifications from this work, Chapter 4 (the other LBGs are all non detections at 3σ).
ALMA identifications from Koprowski et al. (2016), C27, C35, C36, and C39 are non detections,
I have no ALMA data for the other LBGs.
f) Masses indicate the order of magnitude only, based on averaging my four model fits.
** have errors larger than the mass value, *** have errors $> 75\%$ for all models.

SFRs indicated by the presences of AGN or luminous galaxies. However, further observations are required to draw any definite conclusions, especially as not all mergers are high mass.

5.3 Cold gas in the CGM of protoclusters

5.3.1 Powering LABs

In Chapter 4, I investigated the potential powering mechanisms for LABs using SCUBA-2 observations and concluded that star-formation processes are more likely to be the main source of Lyα emission than cold accretion. However, there remain uncertainties in the parameters used in both of my models and it is likely that both processes make some contribution. I also suggested that the fuelling mechanism in the larger LABs, which contain more luminous objects (SMGs and AGN), may be different from that in the smaller LABs, which do not. Further investigation of the presence of submm sources in the LABs will require the use of ALMA.

Recent ALMA 850 μm continuum observations have confirmed the presence of three ALMA sources in LAB1 (Geach et al., 2016), one of which has a spectroscopic redshift, confirming its physical presence within the LAB. These three sources, two of which are thought to be a merging system, correspond to the single source detected with SCUBA-2 (discussed in Chapter 4). Geach et al. (2016) also highlight the presence of many lower-mass galaxies (detected with the *HST*) within LAB1 and suggest these may be satellites of the SMGs. Such a picture is consistent with the LAB representing a region of cold gas lit up by highly star-forming galaxies, but also containing less-massive galaxies, with lower SFRs that may eventually merge with the SMGs as the cluster forms.

Alexander et al. (2016) observed four LABs known to be associated with AGN (LABs 2, 3, 12 and 14) and detected ALMA 870 μm sources in all four, although the LAB3 ALMA detection is in the outskirts of the LAB and may not be associated. ALMA 860 μm sources have also been detected in LABs 5 and 18 in as yet unpublished work (Y. Matsuda private communication). In Fig. 5.3 I have added these new ALMA observations (stars) to my original Fig. 4.4.

Both LAB1 and LAB18, the two SCUBA-2 detections, were found to have multiple ALMA detections. In Fig. 5.3 I plot the sum of the flux density in all ALMA sources within each LAB as LAB1 ALMA (LAB18 ALMA) and the original SCUBA-2 flux densities as LAB1 (LAB18). There is some discrepancy between the total ALMA value and the total S_{850} detected with SCUBA-2. Geach et al. (2016) suggest that this could be due to flux boosting, or there could be additional faint sources not detected in the ALMA observations, but contributing to the SCUBA-2 flux density.

LAB1 and LAB2 are both giant LABs, extending for more than 100 kpc, such large LABs are sometimes considered to be a separate class from the smaller LABs (e.g. Matsuda et al., 2011). The ALMA observations for these two giant LABs put them in the most extreme part of the luminosity space for both models. They both require $f_{esc}f_{sca} > 0.3$ if their Lyα emission is caused by star-formation processes and a dark-matter halo $> 10^{13.5}$ $M_{\odot}$ if cold accretion is

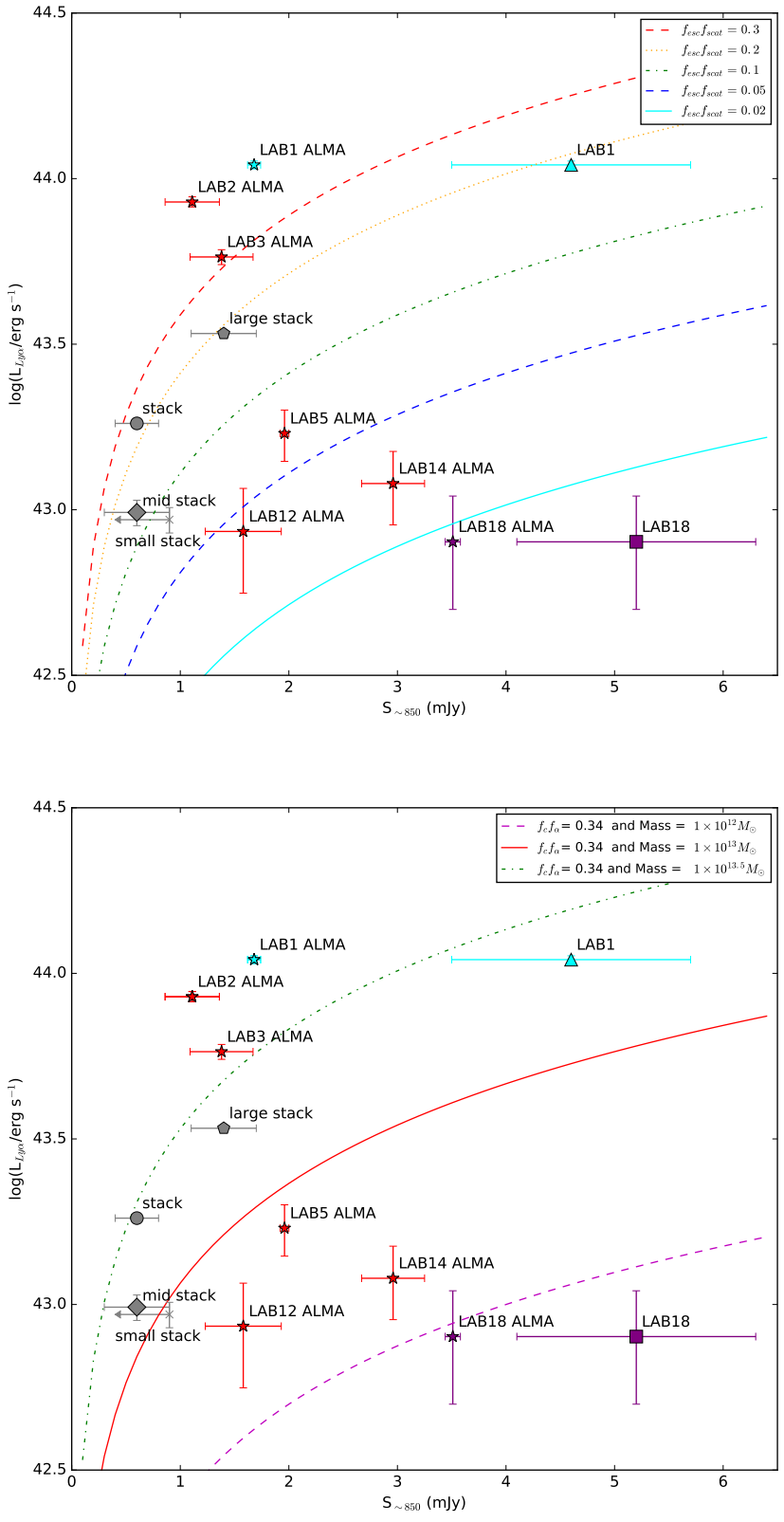

FIGURE 5.3: Log Lyα luminosity plotted against S_{850} as in Fig. 4.4 (Now shown as $S_{\sim 850}$ as some ALMA observations are reported as S_{860} or S_{870}). The lines in the upper image indicate the theoretical $L_{Ly\alpha}$-S_{850} relationship if the LABs are fuelled by star formation processes for a range of values of $f_{esc}f_{sca}$. In the lower image the lines indicate the theoretical $L_{Ly\alpha}$-S_{850} relationship if the LABs are fuelled by cold accretion, for a range of values of halo mass with $f_c f_\alpha = 0.34$. The SCUBA-2 detections for LAB1 (cyan triangle) and LAB18 (purple square) are shown as before, but I have now added ALMA detections from the literature published since my work in Chapter 4 (stars, LAB1 and LAB18 have the same colours as their SCUBA-2 detections for ease of comparison, the rest are in red). The original stacks are also shown in grey.

the dominant process. Both of these scenarios are unlikely. Neither of my models are able to explain the Lyα emission observed in these giant LABs and a more complex scenario is probably required. Despite their large size and high $L_{Ly\alpha}$ the two LABs may have slightly different origins. LAB1 contains multiple submm sources, two LBGs and many faint galaxies, whereas LAB2 contains only one submm source and one LBG, but also has an AGN. This suggests that large LABs can be generated by different combinations of luminous galaxies, AGN and fainter galaxies. Star-formation processes seem to dominate, although it is still possible that cold accretion may also make some contribution.

LAB3 is slightly smaller than the giant LABs, 78 kpc, but lies close to LABs 1 and 2 in luminosity space and also seems to require extreme conditions. It contains a bright x-ray source (AGN), but no LBGs. It appears likely that this LAB is fuelled primarily by the AGN, but it is not clear why it is smaller than LAB2, which has a much fainter AGN. It may be that some of the observed differences in size are due to orientation effects. If Lyα is generated by outflows from an AGN or galaxy, these may well not be symmetrical and so viewing angle would affect the observed projected size.

The remaining LABs are all < 60 kpc and generally lie in less extreme positions in the luminosity space. All require $f_{esc}f_{sca} < 0.1$, which is in agreement with literature values. LABs 5, 12 and 14 require a dark-matter halo mass between $10^{13}\,M_{\odot}$ and $10^{12}\,M_{\odot}$ and simulations indicate that such halo masses are feasible, whilst not common at $z = 3$ (Martinovic, 2015). So these three LABs could be generated by either of the models I considered in Chapter 4, although the conditions required for the star formation model are less extreme. Again, whilst lying in a similar position in the figure, these three LABs are rather different. The only source detected in LAB5 was with IRAC, whilst LABs 12 and 14 contain AGN, IRAC and K band detections (plus an LBG in LAB12). It appears that a number of different star formation processes could be involved with generating the Lyα emission.

LAB18 only requires a halo mass of $10^{12}\,M_{\odot}$ or less and could easily be produced by either of the models. It is interesting that this LAB is so small and faint, compared to LAB1, although they both contain multiple submm sources and were the only two SCUBA-2 detections. LAB18 also contains an AGN, which one might think would generate a larger brighter LAB. Perhaps the smaller size is due to orientation effects, or a more homogeneous gas distribution resulting in a higher covering fraction and therefore lower Lyα escape fraction.

These new observations have, if anything, added further questions regarding the mechanisms involved in generating LABs. All ALMA observations targeting SSA22 LABs have resulted in a detection, but there is no clear correlation between the size and/or Lyα luminosity of the LABs and the presence of AGN and bright galaxies. Evidence so far supports the idea that star-formation processes are important, but suggests that the actual mechanisms may be complex and my analysis may be limited by orientation effects. Most of the LABs have still not been

observed with ALMA and the existing observations have, in general, targeted the larger LABs or those containing AGN. It is still possible that the dominant source of Lyα emission in some of the smaller LABs is cold accretion rather than star formation. Further ALMA observations of the remaining LABs would help to clarify this point.

5.3.2 LABs as tracers of the CGM

The LABs also offer an opportunity to explore the dynamics of the gas in the CGM, as they indicate the presence of large clouds of cold gas within 100 kpc of young galaxies. By combining IFU studies of the Lyα emission, [OIII] line observations tracing ionized gas and ALMA CO(4-3) line observations tracing the dense molecular gas within the galaxies, I can trace inflows and outflows of pristine and recycled gas. These observations can then be compared to my simulation and will help me to understand the contribution of cold accretion to galaxy growth and the impact of outflows on star formation within galaxies. They will also provide further evidence as to the origin of the Lyα emission in LABs.

I will initially study LAB1, for which I already have ALMA Cycle 4 CO(4-3) line observations (awaiting reduction), a MUSE Lyα velocity field map (Hayes 2017 in prep.) and [OIII] line observations (Kubo et al., 2015). I will then aim to use these results to obtain further observations of the other LABs and gain an overall understanding of gas flows around galaxies within the protocluster.

5.3.2.1 Further study of LAB1

Previous ALMA observations of LAB1 have pinpointed the central dusty sources in velocity space with sub-arcsecond accuracy and optical/near-infrared spectroscopy has measured the redshifts of the stellar counterparts to these submillimetre sources (Kubo et al., 2015; Geach et al., 2016). But spectroscopic identification of a dense-gas tracer that can be directly associated with dense molecular reservoirs located within the two sources would allow me to address two important questions:

1. What is the systemic redshift of the main sites of star formation within these two galaxies and how do these relate in terms of relative velocity to (a) each other, and (b) the surrounding Lyα emission? The two ALMA sources are only separated by a few tens of kpc in projection on the sky – a key question is whether they are close in velocity space too; a low relative velocity would lend credence to the hypothesis that the two sources are destined to merge into a single system (expected if the environment is a proto-cluster core). In addition, I will determine if there is any relative offset in velocity of the [OIII] lines associated

with ionized gas in the vicinity of the submillimetre sources; since the dense gas is expected to be actively forming stars, velocity offsets might indicate outflows: I will search for and determine if the ALMA sources are blowing winds into the CGM, which was one of the early LAB-formation hypotheses (e.g. Taniguchi and Shioya, 2000). Measuring the velocity offset between the central sources and the surrounding Lyα is also critical: since Lyα is a resonant line, in order to scatter with a large escape fraction into our line of sight, the photons must go on long flights and be shifted out of resonance (Hayes et al., 2011c) therefore I would expect the systemic redshift of the 'source' galaxies to be close to the centre of the two wings of Lyα emission already observed in LAB1.

2. What is the star formation efficiency (SFE = SFR/Mass of dense molecular gas) of the central galaxies? Armed with measurements of the continuum flux close to the peak of the thermal dust spectrum (850μm measurements trace rest-frame 210μm emission) I can estimate the total SFRs of each ALMA source; with an estimate of the total dense molecular gas (rather than just the total molecular gas) mass I can measure SFR$/M_{\mathrm{H_2}}$ and thus estimate a SFE for the galaxies. This is important to constrain LAB 'cooling' models, since in the equilibrium case the gas accretion rates from the surrounding halo are roughly matched by gas consumption rates. With an empirical estimate of the latter, I will be able to rule in/out gas accretion models, which generally depend on halo mass and baryon fraction. I will also compare these galaxies to other star-forming galaxies at the same redshift not associated with LABs (e.g. Bothwell et al., 2013) – are the 850μm/CO properties consistent with other active galaxies at this epoch? Since LABs are rare objects, there is some reason to believe that the galaxies within them are outliers in terms of SFE.

5.4 The wider population of protoclusters

This thesis has focused on the SSA22 protocluster as a case study. However, to truly understand the impact of the protocluster environment on galaxy evolution, I need to extend my work to additional protoclusters at a range of redshifts. In addition to the $\sim$40 protoclusters already identified, there are ongoing studies searching for protoclusters at different wavelengths, including the JCMT SCUBA-2 protocluster survey, of which I am a member. In the near future I should be in a position to select a sample of protoclusters at a range of redshifts and undertake a comparison of galaxy properties, LAB luminosity and size, merger fractions and gas dynamics. However, it will take some time to build up the multiwavelength observations needed to make such comparisons feasible, particularly for the higher redshift protoclusters where the required observations can only be carried out with state-of-the-art instruments.

The James Webb Space Telescope, due to be launched in 2018, will be particularly useful in obtaining the required photometry for the high-redshift protoclusters, where UV and optical

emission has been redshifted into the NIR. ALMA and MUSE will also continue to be vital for studying submm galaxies and obtaining redshifted CO lines and Lyα IFU maps. Looking further into the future a range of ground-based telescopes are due to start operating in the 2020s, including the European Extremely Large Telescope (E-ELT, a 39m mirror operating at optical, NIR and MIR wavelengths), The Thirty Meter Telescope (TMT, 30m mirror, Near UV to MIR), The Giant Magellan Telescope (effective 24.5m mirror, optical and NIR), and the Large Synoptic Sky Survey Telescope (LSST, UV-optical whole sky 10 year survey). These will provide a rich source of high-resolution photometry and spectroscopy facilitating the in-depth study of protoclusters up to high-redshift. Further space telescopes are also planned, with a mid 2020 launch planned for the WFIRST IR survey telescope and 2028 the current target for the Athena X-ray observatory.

5.5 Final Summary

This multiwavelength study of a $z \sim 3$ protocluster has provided evidence that environment has had an impact on the frequency of mergers, but not, so far, on the mass of LBGs. Differences in galaxy mass may take longer to emerge, or may already have emerged in other types of galaxies not covered by this study. This work has also shed additional light on the generation of Lyα emission observed in the cold gas of the circumgalactic medium, suggesting that star formation processes are the likely dominant source. Further studies of this, and a wider sample of protoclusters, are required to reveal the full impact that environment has on galaxy evolution and to determine at what stage of a protocluster's development these effects become large enough to be observed.

Bibliography

Adelberger, K.L., Steidel, C.C., Shapley, A.E., et al., 2004. Optical Selection of Star-forming Galaxies at Redshifts $1 < z < 3$. *ApJ*, 607:226.

Alexander, D.M., Simpson, J.M., Harrison, C.M., et al., 2016. ALMA observations of a $z \sim 3.1$ protocluster: star formation from active galactic nuclei and Lyman-alpha blobs in an overdense environment. *MNRAS*, 461:2944.

Álvarez-Márquez, J., Burgarella, D., Heinis, S., et al., 2015. Dust properties of Lyman break galaxies at $z \sim 3$. *ArXiv e-prints*.

Anderson, L., Aubourg, E., Bailey, S., et al., 2012. The clustering of galaxies in the SDSS-III Baryon Oscillation Spectroscopic Survey: baryon acoustic oscillations in the Data Release 9 spectroscopic galaxy sample. *MNRAS*, 427:3435.

Angulo, R.E., Springel, V., White, S.D.M., et al., 2012. The journey of QSO haloes from $z \sim 6$ to the present. *MNRAS*, 425:2722.

Ao, Y., Matsuda, Y., Beelen, A., et al., 2015. What Powers Lyman alpha Blobs? *ArXiv e-prints*.

Ashby, M.L.N., Dye, S., Huang, J.S., et al., 2006. Mid-Infrared Identifications of SCUBA Galaxies in the CUDSS 14 Hour Field with the Spitzer Space Telescope. *ApJ*, 644:778.

Ashby, M.L.N., Willner, S.P., Fazio, G.G., et al., 2013. SEDS: The Spitzer Extended Deep Survey. Survey Design, Photometry, and Deep IRAC Source Counts. *ApJ*, 769:80.

Avila-Reese, V., Zavala, J., and Lacerna, I., 2014. The growth of galactic bulges through mergers in Λ cold dark matter haloes revisited - II. Morphological mix evolution. *MNRAS*, 441:417.

Baldry, I.K., Glazebrook, K., Brinkmann, J., et al., 2004. Quantifying the Bimodal Color-Magnitude Distribution of Galaxies. *ApJ*, 600:681.

Barger, A.J., Cowie, L.L., Sanders, D.B., et al., 1998. Submillimetre-wavelength detection of dusty star-forming galaxies at high redshift. *Nature*, 394:248.

Barger, A.J., Cowie, L.L., and Wold, I.G.B., 2012. A Flux-limited Sample of z ˜ 1 Lyα Emitting Galaxies in the Chandra Deep Field South. *ApJ*, 749:106.

Basu-Zych, A. and Scharf, C., 2004. X-Ray Detection of an Obscured Active Galactic Nucleus in a z=3.09 Radio-quiet Lyα Nebula. *ApJ*, 615:L85.

Baugh, C.M., 2006. A primer on hierarchical galaxy formation: the semi-analytical approach. *Reports on Progress in Physics*, 69:3101.

Begelman, M.C., Blandford, R.D., and Rees, M.J., 1984. Theory of extragalactic radio sources. *Reviews of Modern Physics*, 56:255.

Bell, E.F., McIntosh, D.H., Katz, N., et al., 2003. The Optical and Near-Infrared Properties of Galaxies. I. Luminosity and Stellar Mass Functions. *ApJ*, 149:289.

Bell, E.F., Naab, T., McIntosh, D.H., et al., 2006. Dry Mergers in GEMS: The Dynamical Evolution of Massive Early-Type Galaxies. *ApJ*, 640:241.

Benson, A.J., 2010. Galaxy formation theory. *Physics Reports*, 495:33.

Benson, A.J., Frenk, C.S., Baugh, C.M., et al., 2001. The clustering evolution of the galaxy distribution. *MNRAS*, 327:1041.

Berendsen, H.J.C., 2011. *A Student's Guide to Data and Error Analysis*. Cambridge University Press, Cambridge.

Biggs, A.D., Ivison, R.J., Ibar, E., et al., 2011. The LABOCA survey of the Extended Chandra Deep Field-South - radio and mid-infrared counterparts to submillimetre galaxies. *MNRAS*, 413:2314.

Blain, A.W. and Longair, M.S., 1993. Submillimetre Cosmology. *MNRAS*, 264:509.

Bluck, A.F.L., Conselice, C.J., Bouwens, R.J., et al., 2009. A surprisingly high pair fraction for extremely massive galaxies at z ˜ 3 in the GOODS NICMOS survey. *MNRAS*, 394:L51.

Bluck, A.F.L., Conselice, C.J., Buitrago, F., et al., 2012. The Structures and Total (Minor + Major) Merger Histories of Massive Galaxies up to z ˜ 3 in the HST GOODS NICMOS Survey: A Possible Solution to the Size Evolution Problem. *ApJ*, 747:34.

Bolzonella, M., Miralles, J.M., and Pelló, R., 2000. Photometric redshifts based on standard SED fitting procedures. *A&A*, 363:476.

Bothwell, M.S., Smail, I., Chapman, S.C., et al., 2013. A survey of molecular gas in luminous sub-millimetre galaxies. *MNRAS*, 429:3047.

Bourne, N., Dunlop, J.S., Merlin, E., et al., 2017. Evolution of cosmic star formation in the SCUBA-2 Cosmology Legacy Survey. *MNRAS*.

Bouwens, R.J., Aravena, M., Decarli, R., et al., 2016. ALMA Spectroscopic Survey in the Hubble Ultra Deep Field: The Infrared Excess of UV-Selected z = 2-10 Galaxies as a Function of UV-Continuum Slope and Stellar Mass. *ApJ*, 833:72.

Bouwens, R.J., Bradley, L., Zitrin, A., et al., 2014. A Census of Star-forming Galaxies in the Z ˜ 9-10 Universe based on HST+Spitzer Observations over 19 Clash Clusters: Three Candidate Z ˜ 9-10 Galaxies and Improved Constraints on the Star Formation Rate Density at Z ˜ 9.2. *ApJ*, 795:126.

Bower, R.G. and Balogh, M.L., 2004. The Difference Between Clusters and Groups: A Journey from Cluster Cores to Their Outskirts and Beyond. *Clusters of Galaxies: Probes of Cosmological Structure and Galaxy Evolution*, page 325.

Bower, R.G., Morris, S.L., Bacon, R., et al., 2004. Deep SAURON spectral imaging of the diffuse Lyman α halo LAB1 in SSA 22. *MNRAS*, 351:63.

Boylan-Kolchin, M., Springel, V., White, S.D.M., et al., 2009. Resolving cosmic structure formation with the Millennium-II Simulation. *MNRAS*, 398:1150 .

Bridge, C.R., Blain, A., Borys, C.J.K., et al., 2013. A New Population of High-z, Dusty Lyα Emitters and Blobs Discovered by WISE: Feedback Caught in the Act? *ApJ*, 769:91.

Brinchmann, J., Charlot, S., White, S.D.M., et al., 2004. The physical properties of star-forming galaxies in the low-redshift Universe. *MNRAS*, 351:1151.

Brinchmann, J. and Ellis, R.S., 2000. The Mass Assembly and Star Formation Characteristics of Field Galaxies of Known Morphology. *ApJ*, 536:L77.

Brocklehurst, M., 1971. Calculations of level populations for the low levels of hydrogenic ions in gaseous nebulae. *MNRAS*, 153:471.

Bruzual, G. and Charlot, S., 2003. Stellar population synthesis at the resolution of 2003. *MNRAS*, 344:1000.

Bullock, J.S., Kolatt, T.S., Sigad, Y., et al., 2001. Profiles of dark haloes: evolution, scatter and environment. *MNRAS*, 321:559.

Burgarella, D., Buat, V., and Iglesias-Páramo, J., 2005. Star formation and dust attenuation properties in galaxies from a statistical ultraviolet-to-far-infrared analysis. *MNRAS*, 360:1413.

Calistro Rivera, G., Lusso, E., Hennawi, J.F., et al., 2016. AGNfitter: SED-fitting code for AGN and galaxies from a MCMC approach. Astrophysics Source Code Library.

Calzetti, D., Armus, L., Bohlin, R.C., et al., 2000. The Dust Content and Opacity of Actively Star-forming Galaxies. *ApJ*, 533:682.

Cantalupo, S., Lilly, S.J., and Haehnelt, M.G., 2012. Detection of dark galaxies and circumgalactic filaments fluorescently illuminated by a quasar at z = 2.4. *MNRAS*, 425:1992.

Caputi, K.I., Dunlop, J.S., McLure, R.J., et al., 2004. A deeper view of extremely red galaxies: the redshift distribution in the GOODS/CDFS ISAAC field. *MNRAS*, 353:30.

Cardelli, J.A., Clayton, G.C., and Mathis, J.S., 1989. The relationship between infrared, optical, and ultraviolet extinction. *ApJ*, 345:245.

Casey, C.M., 2012. Far-infrared spectral energy distribution fitting for galaxies near and far. *MNRAS*, 425:3094.

Casey, C.M., Cooray, A., Capak, P., et al., 2015. A Massive, Distant Proto-cluster at z = 2.47 Caught in a Phase of Rapid Formation? *ApJ*, 808:L33.

Casey, C.M., Narayanan, D., and Cooray, A., 2014. Dusty star-forming galaxies at high redshift. *Physics Reports*, 541:45.

Cassata, P., Giavalisco, M., Guo, Y., et al., 2011. The Relative Abundance of Compact and Normal Massive Early-type Galaxies and Its Evolution from Redshift z $\sim$ 2 to the Present. *ApJ*, 743:96.

Cen, R., 2014a. Evolution of Cold Streams and the Emergence of the Hubble Sequence. *ApJ*, 789:L21.

Cen, R., 2014b. Frequent Spin Reorientation of Galaxies due to Local Interactions. *ApJ*, 785:L15.

Cen, R., 2014c. On the Origin of the Hubble Sequence: I. Insights on Galaxy Color Migration from Cosmological Simulations. *ApJ*, 781:38.

Cen, R. and Ostriker, J.P., 2000. Physical Bias of Galaxies from Large-Scale Hydrodynamic Simulations. *ApJ*, 538:83.

Cen, R. and Zheng, Z., 2013. The Nature of Lyα Blobs: Powered by Extreme Starbursts. *ApJ*, 775:112.

Chabrier, G., 2003. Galactic Stellar and Substellar Initial Mass Function. *PASP*, 115:763.

Chapin, E.L., Berry, D.S., Gibb, A.G., et al., 2013. SCUBA-2: iterative map-making with the Sub-Millimetre User Reduction Facility. *MNRAS*, 430:2545.

Chapin, E.L., Chapman, S.C., Coppin, K.E., et al., 2011. A joint analysis of BLAST 250-500 μm and LABOCA 870 μm observations in the Extended Chandra Deep Field-South. *MNRAS*, 411:505.

Chapman, S.C., Blain, A.W., Smail, I., et al., 2005. A Redshift Survey of the Submillimeter Galaxy Population. *ApJ*, 622:772.

Chapman, S.C., Lewis, G.F., Scott, D., et al., 2001. Submillimeter Imaging of a Protocluster Region at Z=3.09. *ApJ*, 548:L17.

Chapman, S.C., Scott, D., Windhorst, R.A., et al., 2004. Further Multiwavelength Observations of the SSA 22 Lyα-Emitting Blob. *ApJ*, 606:85.

Chiang, Y.K., Overzier, R., and Gebhardt, K., 2013. Ancient Light from Young Cosmic Cities: Physical and Observational Signatures of Galaxy Proto-clusters. *ApJ*, 779:127.

Chiang, Y.K., Overzier, R., and Gebhardt, K., 2014. Discovery of a Large Number of Candidate Protoclusters Traced by ˜15 Mpc-scale Galaxy Overdensities in COSMOS. *ApJ*, 782:L3.

Chiang, Y.K., Overzier, R.A., Gebhardt, K., et al., 2015. Surveying Galaxy Proto-clusters in Emission: A Large-scale Structure at z = 2.44 and the Outlook for HETDEX. *ApJ*, 808:37.

Cimatti, A., Brusa, M., Talia, M., et al., 2013. Active Galactic Nucleus Feedback at z ˜ 2 and the Mutual Evolution of Active and Inactive Galaxies. *ApJ*, 779:L13.

Coe, D., Zitrin, A., Carrasco, M., et al., 2013. Clash: Three strongly lensed images of a candidate z $\sim$ 11 galaxy. *ApJ*, 762(1):32.

Coleman, G.D., Wu, C.C., and Weedman, D.W., 1980. Colors and magnitudes predicted for high redshift galaxies. *ApJ*, 43:393.

Colless, M., Dalton, G., Maddox, S., et al., 2001. The 2dF Galaxy Redshift Survey: spectra and redshifts. *MNRAS*, 328:1039.

Conroy, C., 2013. Modeling the Panchromatic Spectral Energy Distributions of Galaxies. *Annual Review of Astronomy and Astrophysics*, 51:393.

Conselice, C.J., 2007. Galaxy Mergers and Interactions at High Redshift. In F. Combes and J. Palouš, editors, *Galaxy Evolution across the Hubble Time*, volume 235 of *IAU Symposium*, pages 381–384.

Conselice, C.J., 2009. The structures of distant galaxies - IV. A new empirical measurement of the time-scale for galaxy mergers - implications for the merger history. *MNRAS*, 399:L16.

Conselice, C.J., 2014. The Evolution of Galaxy Structure Over Cosmic Time. *Annual Review of Astronomy and Astrophysics*, 52:291.

Conselice, C.J. and Arnold, J., 2009. The structures of distant galaxies - II. Diverse galaxy structures and local environments at z = 4-6 implications for early galaxy assembly. *MNRAS*, 397:208.

Conselice, C.J., Mortlock, A., Bluck, A.F.L., et al., 2013. Gas accretion as a dominant formation mode in massive galaxies from the GOODS NICMOS Survey. *MNRAS*, 430:1051.

Conselice, C.J., Rajgor, S., and Myers, R., 2008. The structures of distant galaxies - I. Galaxy structures and the merger rate to z $\sim$ 3 in the Hubble Ultra-Deep Field. *MNRAS*, 386:909.

Contini, E. and Kang, X., 2015. Semi-analytic model predictions of mass segregation from groups to clusters. *MNRAS*, 453:L53.

Cooke, E.A., Hatch, N.A., Muldrew, S.I., et al., 2014. A z = 2.5 protocluster associated with the radio galaxy MRC 2104-242: star formation and differing mass functions in dense environments. *MNRAS*, 440:3262.

Coppin, K.E.K., Geach, J.E., Almaini, O., et al., 2015. The SCUBA-2 Cosmology Legacy Survey: the submillimetre properties of Lyman-break galaxies at z = 3-5. *MNRAS*, 446:1293.

Cowie, L.L., Songaila, A., Hu, E.M., et al., 1996. New Insight on Galaxy Formation and Evolution from Keck Spectroscopy of the Hawaii Deep Fields . *ApJ*, 112:839.

Cox, T.J., Jonsson, P., Somerville, R.S., et al., 2008. The effect of galaxy mass ratio on merger-driven starbursts. *MNRAS*, 384:386.

Crain, R.A., Schaye, J., Bower, R.G., et al., 2015. The EAGLE simulations of galaxy formation: calibration of subgrid physics and model variations. *MNRAS*, 450:1937.

Croton, D.J., Springel, V., White, S.D.M., et al., 2006. The many lives of active galactic nuclei: cooling flows, black holes and the luminosities and colours of galaxies. *MNRAS*, 365:11.

Cucciati, O., Zamorani, G., Lemaux, B.C., et al., 2014. Discovery of a rich proto-cluster at z = 2.9 and associated diffuse cold gas in the VIMOS Ultra-Deep Survey (VUDS). *A&A*, 570:A16.

da Cunha, E., Charlot, S., and Elbaz, D., 2008. A simple model to interpret the ultraviolet, optical and infrared emission from galaxies. *MNRAS*, 388:1595.

Daddi, E., Cimatti, A., Pozzetti, L., et al., 2000. Detection of strong clustering of extremely red objects: implications for the density of z$<$1 ellipticals. *A&A*, 361:535.

Daddi, E., Cimatti, A., Renzini, A., et al., 2004. A New Photometric Technique for the Joint Selection of Star-forming and Passive Galaxies at $1.4 < z < 2.5$. *ApJ*, 617:746.

Daddi, E., Dickinson, M., Chary, R., et al., 2005. The Population of BzK-selected ULIRGs at z ˜ 2. *ApJ*, 631:L13.

Daddi, E., Dickinson, M., Morrison, G., et al., 2007. Multiwavelength Study of Massive Galaxies at z$\sim$2. I. Star Formation and Galaxy Growth. *ApJ*, 670:156.

Dale, D.A., Helou, G., Magdis, G.E., et al., 2014. A Two-parameter Model for the Infrared/-Submillimeter/Radio Spectral Energy Distributions of Galaxies and Active Galactic Nuclei. *ApJ*, 784:83.

Damen, M., Labbé, I., Franx, M., et al., 2009. The Evolution of the Specific Star Formation Rate of Massive Galaxies to z ˜ 1.8 in the Extended Chandra Deep Field South. *ApJ*, 690:937.

Davé, R., Finlator, K., Oppenheimer, B.D., et al., 2010. The nature of submillimetre galaxies in cosmological hydrodynamic simulations. *MNRAS*, 404:1355.

Davis, M., Efstathiou, G., Frenk, C.S., et al., 1985. The evolution of large-scale structure in a universe dominated by cold dark matter. *ApJ*, 292:371.

de Barros, S., Schaerer, D., and Stark, D.P., 2014. Properties of z $\sim$ 3-6 Lyman break galaxies. II. Impact of nebular emission at high redshift. *A&A*, 563:A81.

De Breuck, C., Seymour, N., Stern, D., et al., 2010. The Spitzer High-redshift Radio Galaxy Survey. *ApJ*, 725:36.

De Breuck, C., van Breugel, W., Minniti, D., et al., 1999. VLT spectroscopy of the z=4.11 Radio Galaxy TN J1338-1942. *A&A*, 352:L51.

De Lucia, G. and Blaizot, J., 2007. The hierarchical formation of the brightest cluster galaxies. *MNRAS*, 375:2.

De Lucia, G., Springel, V., White, S.D.M., et al., 2006. The formation history of elliptical galaxies. *MNRAS*, 366:499.

Dekel, A. and Birnboim, Y., 2006. Galaxy bimodality due to cold flows and shock heating. *MNRAS*, 368:2.

Dekel, A., Sari, R., and Ceverino, D., 2009. Formation of Massive Galaxies at High Redshift: Cold Streams, Clumpy Disks, and Compact Spheroids. *ApJ*, 703:785.

Dempsey, J.T., Friberg, P., Jenness, T., et al., 2013. SCUBA-2: on-sky calibration using submillimetre standard sources. *MNRAS*, 430:2534.

Dey, A., Bian, C., Soifer, B.T., et al., 2005. Discovery of a Large ˜200 kpc Gaseous Nebula at z ˜ 2.7 with the Spitzer Space Telescope. *ApJ*, 629:654.

Dicke, R.H., Peebles, P.J.E., Roll, P.G., et al., 1965. Cosmic Black-Body Radiation. *ApJ*, 142:414.

Dijkstra, M., Haiman, Z., and Spaans, M., 2006a. Lyα Radiation from Collapsing Protogalaxies. I. Characteristics of the Emergent Spectrum. *ApJ*, 649:14.

Dijkstra, M., Haiman, Z., and Spaans, M., 2006b. Lyα Radiation from Collapsing Protogalaxies. II. Observational Evidence for Gas Infall. *ApJ*, 649:37.

Dijkstra, M. and Jeeson-Daniel, A., 2013. Empirical constraints on the star formation and redshift dependence of the Lyα 'effective' escape fraction. *MNRAS*, 435:3333.

Dijkstra, M. and Westra, E., 2010. Star formation indicators and line equivalent width in Lyα galaxies. *MNRAS*, 401:2343.

Djorgovski, S., Spinrad, H., McCarthy, P., et al., 1985. Discovery of a probable galaxy with a redshift of 3.218. *ApJ*, 299:L1.

Draine, B.T. and Li, A., 2007. Infrared Emission from Interstellar Dust. IV. The Silicate-Graphite-PAH Model in the Post-Spitzer Era. *ApJ*, 657:810.

Dubinski, J., 1998. The Origin of the Brightest Cluster Galaxies. *ApJ*, 502:141.

Ellis, R.S., McLure, R.J., Dunlop, J.S., et al., 2013. The Abundance of Star-forming Galaxies in the Redshift Range 8.5-12: New Results from the 2012 Hubble Ultra Deep Field Campaign. *ApJ*, 763:L7.

Erb, D.K., Bogosavljević, M., and Steidel, C.C., 2011. Filamentary Large-scale Structure Traced by Six Lyα Blobs at z = 2.3. *ApJ*, 740:L31.

Erb, D.K., Shapley, A.E., Pettini, M., et al., 2006. The Mass-Metallicity Relation at z¿ 2. *ApJ*, 644:813.

Erb, D.K., Steidel, C.C., Trainor, R.F., et al., 2014. The Lyα Properties of Faint Galaxies at z ˜ 2-3 with Systemic Redshifts and Velocity Dispersions from Keck-MOSFIRE. *ApJ*, 795:33.

Fakhouri, O. and Ma, C.P., 2009. Environmental dependence of dark matter halo growth - I. Halo merger rates. *MNRAS*, 394:1825.

Faucher-Giguère, C.A., Kereš, D., Dijkstra, M., et al., 2010. Lyα Cooling Emission from Galaxy Formation. *ApJ*, 725:633.

Ferrarese, L. and Merritt, D., 2000. A Fundamental Relation between Supermassive Black Holes and Their Host Galaxies. *ApJ*, 539:L9.

Finkelstein, K.D., Finkelstein, S.L., Tilvi, V., et al., 2015. Probing the Physical Properties of z = 4.5 Lyman Alpha Emitters with Spitzer. *ApJ*, 813:78.

Fitzpatrick, E.L., 1986. An average interstellar extinction curve for the Large Magellanic Cloud. *AJ*, 92:1068.

Francis, P.J., Woodgate, B.E., Warren, S.J., et al., 1996. A Group of Galaxies at Redshift 2.38. *ApJ*, 457:490.

Franx, M., Labbé, I., Rudnick, G., et al., 2003. A significant population of red, near-infrared-selected high-redshift galaxies. *ApJ*, 587(2):L79.

Gawiser, E., Francke, H., Lai, K., et al., 2007. Lyα-Emitting Galaxies at z = 3.1: L* Progenitors Experiencing Rapid Star Formation. *ApJ*, 671:278.

Geach, J.E., Alexander, D.M., Lehmer, B.D., et al., 2009. The Chandra Deep Protocluster Survey: Lyα Blobs are Powered by Heating, Not Cooling. *ApJ*, 700:1.

Geach, J.E., Bower, R.G., Alexander, D.M., et al., 2014. A Submillimeter Galaxy Illuminating its Circumgalactic Medium: Lyα Scattering in a Cold, Clumpy Outflow. *ApJ*, 793:22.

Geach, J.E., Chapin, E.L., Coppin, K.E.K., et al., 2013. The SCUBA-2 Cosmology Legacy Survey: blank-field number counts of 450-μm-selected galaxies and their contribution to the cosmic infrared background. *MNRAS*, 432:53.

Geach, J.E., Dunlop, J.S., Halpern, M., et al., 2017. The SCUBA-2 Cosmology Legacy Survey: 850 μm maps, catalogues and number counts. *MNRAS*, 465:1789.

Geach, J.E., Matsuda, Y., Smail, I., et al., 2005. A submillimetre survey of Lyman α haloes in the SA22 protocluster at z= 3.1. *MNRAS*, 363:1398.

Geach, J.E., Narayanan, D., Matsuda, Y., et al., 2016. ALMA Observations of Lyα Blob 1: Halo Substructure Illuminated from Within. *ApJ*, 832:37.

Geach, J.E., Smail, I., Best, P.N., et al., 2008. HiZELS: a high-redshift survey of Hα emitters - I. The cosmic star formation rate and clustering at z = 2.23. *MNRAS*, 388:1473.

Geach, J.E., Smail, I., Chapman, S.C., et al., 2007. Spitzer Identifications and Classifications of Submillimeter Galaxies in Giant, High-Redshift, Lyα-Emission-Line Nebulae. *ApJ*, 655:L9.

Gebhardt, K., Bender, R., Bower, G., et al., 2000. A Relationship between Nuclear Black Hole Mass and Galaxy Velocity Dispersion. *ApJ*, 539:L13.

Giavalisco, M., 2002. Lyman-Break Galaxies. *Annual Review of Astronomy and Astrophysics*, 40:579.

Goerdt, T. and Ceverino, D., 2015. Inflow velocities of cold flows streaming into massive galaxies at high redshifts. *ArXiv e-prints*.

Goerdt, T., Dekel, A., Sternberg, A., et al., 2010. Gravity-driven Lyα blobs from cold streams into galaxies. *MNRAS*, 407:613.

Gonçalves, T.S., Martin, D.C., Menéndez-Delmestre, K., et al., 2012. Quenching Star Formation at Intermediate Redshifts: Downsizing of the Mass Flux Density in the Green Valley. *ApJ*, 759:67.

González, V., Bouwens, R., Illingworth, G., et al., 2014. Slow Evolution of the Specific Star Formation Rate at z $\geq$ 2: The Impact of Dust, Emission Lines, and a Rising Star Formation History. *ApJ*, 781:34.

Gordon, K.D., Clayton, G.C., Misselt, K.A., et al., 2003. A Quantitative Comparison of the Small Magellanic Cloud, Large Magellanic Cloud, and Milky Way Ultraviolet to Near-Infrared Extinction Curves. *ApJ*, 594:279.

Gottlieb, D.M. and Upson, II, W.L., 1969. Local Interstellar Reddening. *ApJ*, 157:611.

Gottlöber, S., Klypin, A., and Kravtsov, A.V., 2001. Merging History as a Function of Halo Environment. *ApJ*, 546:223.

Governato, F., Baugh, C.M., Frenk, C.S., et al., 1998. The seeds of rich galaxy clusters in the Universe. *Nature*, 392:359.

Gunn, J.E. and Gott, III, J.R., 1972. On the Infall of Matter Into Clusters of Galaxies and Some Effects on Their Evolution. *ApJ*, 176:1.

Guo, Q., White, S., Angulo, R.E., et al., 2013. Galaxy formation in WMAP1 and WMAP7 cosmologies. *MNRAS*, 428:1351.

Haiman, Z. and Spaans, M., 1999. Models for Dusty Lyα Emitters at High Redshift. *ApJ*, 518:138.

Haiman, Z., Spaans, M., and Quataert, E., 2000. Lyα Cooling Radiation from High-Redshift Halos. *ApJ*, 537:L5.

Hainline, L.J., Blain, A.W., Smail, I., et al., 2009. A Mid-Infrared Imaging Survey of Submillimeter-Selected Galaxies with the Spitzer Space Telescope. *ApJ*, 699:1610.

Hainline, L.J., Blain, A.W., Smail, I., et al., 2011. The Stellar Mass Content of Submillimeter-selected Galaxies. *ApJ*, 740:96.

Hao, C.N., Kennicutt, R.C., Johnson, B.D., et al., 2011. Dust-corrected Star Formation Rates of Galaxies. II. Combinations of Ultraviolet and Infrared Tracers. *ApJ*, 741:124.

Hatch, N.A., Kurk, J.D., Pentericci, L., et al., 2011. Hα emitters in z$\sim$ 2 protoclusters: evidence for faster evolution in dense environments. *MNRAS*, 415:2993.

Hatch, N.A., Muldrew, S.I., Cooke, E.A., et al., 2016. The structure and evolution of a forming galaxy cluster at z = 1.62. *MNRAS*, 459:387.

Hatch, N.A., Overzier, R.A., Kurk, J.D., et al., 2009. The growth and assembly of a massive galaxy at z$\sim$2. *MNRAS*, 395:114.

Hayashino, T., Matsuda, Y., Tamura, H., et al., 2004. Large-scale structure of emission-line galaxies at z = 3.1. *AJ*, 128:2073.

Hayes, M., Scarlata, C., and Siana, B., 2011a. Central powering of the largest Lyman-α nebula is revealed by polarized radiation. *Nature*, 476:304.

Hayes, M., Schaerer, D., Östlin, G., et al., 2011b. On the Redshift Evolution of the Lyα Escape Fraction and the Dust Content of Galaxies. *ApJ*, 730:8.

Hayes, M., Schaerer, D., Östlin, G., et al., 2011c. On the Redshift Evolution of the LyαEscape Fraction and the Dust Content of Galaxies. *ApJ*, 730:8.

Hayward, C.C., Kereš, D., Jonsson, P., et al., 2011. What Does a Submillimeter Galaxy Selection Actually Select? The Dependence of Submillimeter Flux Density on Star Formation Rate and Dust Mass. *ApJ*, 743:159.

Hayward, C.C., Narayanan, D., Kereš, D., et al., 2013. Submillimetre galaxies in a hierarchical universe: number counts, redshift distribution and implications for the IMF. *MNRAS*, 428:2529.

Heckman, T.M., Smith, E.P., Baum, S.A., et al., 1986. Galaxy collisions and mergers - The genesis of very powerful radio sources? *ApJ*, 311:526.

Heinis, S., Buat, V., Béthermin, M., et al., 2013. HERMES: unveiling obscured star formation - the far-infrared luminosity function of ultraviolet-selected galaxies at z $\sim$ 1.5. *MNRAS*, 429:1113.

Hildebrand, R.H., 1983. The Determination of Cloud Masses and Dust Characteristics from Submillimetre Thermal Emission. *Quarterly Journal of the Royal Astronomical Society*, 24:267.

Hine, N.K., Geach, J.E., Alexander, D.M., et al., 2016. An enhanced merger fraction within the galaxy population of the SSA22 protocluster at z = 3.1. *MNRAS*, 455:2363.

Hinojosa-Goñi, R., Muñoz-Tuñón, C., and Méndez-Abreu, J., 2016. Starburst galaxies in the COSMOS field: clumpy star-formation at redshift $0 < z < 0.5$. *A&A*, 592:A122.

Hodge, J.A., Karim, A., Smail, I., et al., 2013. An ALMA Survey of Submillimeter Galaxies in the Extended Chandra Deep Field South: Source Catalog and Multiplicity. *ApJ*, 768:91.

Holland, W.S., Bintley, D., Chapin, E.L., et al., 2013. SCUBA-2: the 10 000 pixel bolometer camera on the James Clerk Maxwell Telescope. *MNRAS*, 430:2513.

Hopkins, P.F., Hernquist, L., Cox, T.J., et al., 2006. A Unified, Merger-driven Model of the Origin of Starbursts, Quasars, the Cosmic X-Ray Background, Supermassive Black Holes, and Galaxy Spheroids. *ApJ*, 163:1.

Hubble, E.P., 1926. Extragalactic nebulae. *ApJ*, 64.

Huertas-Company, M., Kaviraj, S., Mei, S., et al., 2014. Measuring galaxy morphology at $z > 1$. I - calibration of automated proxies. *ArXiv e-prints*.

Huertas-Company, M., Pérez-González, P.G., Mei, S., et al., 2015. The Morphologies of Massive Galaxies from z$\sim$ 3 - Witnessing the Two Channels of Bulge Growth. *ApJ*, 809:95.

Hughes, D.H., Serjeant, S., Dunlop, J., et al., 1998. High-redshift star formation in the Hubble Deep Field revealed by a submillimetre-wavelength survey. *Nature*, 394:241.

Hurley, P.D., Oliver, S., Betancourt, M., et al., 2017. HELP: XID+, the probabilistic de-blender for Herschel SPIRE maps. *MNRAS*, 464:885.

Ivison, R.J., Dunlop, J.S., Smail, I., et al., 2000. An Excess of Submillimeter Sources near 4C 41.17: A Candidate Protocluster at Z = 3.8? *ApJ*, 542:27.

Ivison, R.J., Smail, I., Le Borgne, J.F., et al., 1998. A hyperluminous galaxy at z=2.8 found in a deep submillimetre survey. *MNRAS*, 298:583.

Juneau, S., Glazebrook, K., Crampton, D., et al., 2005. Cosmic Star Formation History and Its Dependence on Galaxy Stellar Mass. *ApJ*, 619:L135.

Kaiser, N., 1987. Clustering in real space and in redshift space. *MNRAS*, 227:1.

Karim, A., Schinnerer, E., Martínez-Sansigre, A., et al., 2011. The Star Formation History of Mass-selected Galaxies in the COSMOS Field. *ApJ*, 730:61.

Karl, S.J., Naab, T., Johansson, P.H., et al., 2010. One Moment in Time - Modeling Star Formation in the Antennae. *ApJ*, 715:L88.

Kato, Y., Matsuda, Y., Smail, I., et al., 2016. Herschel protocluster survey: a search for dusty star-forming galaxies in protoclusters at z = 2-3. *MNRAS*, 460:3861.

Katz, N. and Gunn, J.E., 1991. Dissipational galaxy formation. I - Effects of gasdynamics. *ApJ*, 377:365.

Katz, N., Keres, D., Dave, R., et al., 2003. How Do Galaxies Get Their Gas? In J.L. Rosenberg and M.E. Putman, editors, *The IGM/Galaxy Connection. The Distribution of Baryons at z=0*, volume 281 of *Astrophysics and Space Science Library*, page 185.

Kauffmann, G., 1996. The age of elliptical galaxies and bulges in a merger model. *MNRAS*, 281:487.

Kauffmann, G., Colberg, J.M., Diaferio, A., et al., 1999. Clustering of galaxies in a hierarchical universe - II. Evolution to high redshift. *MNRAS*, 307:529.

Kauffmann, G., Heckman, T.M., White, S.D.M., et al., 2003. Stellar masses and star formation histories for 10^5 galaxies from the Sloan Digital Sky Survey. *MNRAS*, 341:33.

Kaviraj, S., 2014. The significant contribution of minor mergers to the cosmic star formation budget. *MNRAS*, 437:L41.

Kaviraj, S., Devriendt, J., Dubois, Y., et al., 2015. Galaxy merger histories and the role of merging in driving star formation at $z > 1$. *MNRAS*, 452:2845.

Kaviraj, S., Peirani, S., Khochfar, S., et al., 2009. The role of minor mergers in the recent star formation history of early-type galaxies. *MNRAS*, 394:1713.

Keel, W.C., Cohen, S.H., Windhorst, R.A., et al., 1999. Evidence for Large-Scale Structure at z ˜ 2.4 from Lyα Imaging. *AJ*, 118:2547.

Kennicutt, R.C. and Evans, N.J., 2012. Star Formation in the Milky Way and Nearby Galaxies. *Annual Review of Astronomy and Astrophysics*, 50:531.

Kennicutt, Jr., R.C., 1998. Star Formation in Galaxies Along the Hubble Sequence. *Annual Review of Astronomy and Astrophysics*, 36:189.

Keres, D., Katz, N., Fardal, M., et al., 2009. Galaxies in a simulated ΛCDM Universe - I. Cold mode and hot cores. *MNRAS*, 395:160.

Keres, D., Katz, N., Weinberg, D.H., et al., 2005. How do galaxies get their gas? *MNRAS*, 363:2.

Koprowski, M., Dunlop, J.S., Michalowski, M.J., et al., 2015. The SCUBA-2 Cosmology Legacy Survey: galaxies in the deep 850-micron survey, and the star-forming 'main sequence'. *ArXiv e-prints*.

Koprowski, M.P., Coppin, K.E.K., Geach, J.E., et al., 2016. A Resolved Map of the Infrared Excess in a Lyman Break Galaxy at z = 3. *ApJ*, 828:L21.

Kormendy, J. and Kennicutt, Jr., R.C., 2004. Secular Evolution and the Formation of Pseudobulges in Disk Galaxies. *Annual Review of Astronomy and Astrophysics*, 42:603.

Kornei, K.A., Shapley, A.E., Erb, D.K., et al., 2010. The Relationship between Stellar Populations and Lyα Emission in Lyman Break Galaxies. *ApJ*, 711:693.

Koyama, Y., Kodama, T., Tadaki, K.i., et al., 2013. Massive starburst galaxies in a z = 2.16 proto-cluster unveiled by panoramic Hα mapping. *MNRAS*, 428:1551.

Kroupa, P. and Weidner, C., 2003. Galactic-Field Initial Mass Functions of Massive Stars. *ApJ*, 598:1076.

Kubo, M., Uchimoto, Y.K., Yamada, T., et al., 2013. The Formation of the Massive Galaxies in the SSA22 z = 3.1 Protocluster. *ApJ*, 778:170.

Kubo, M., Yamada, T., Ichikawa, T., et al., 2015. NIR Spectroscopic Observation of Massive Galaxies in the Protocluster at z = 3.09. *ApJ*, 799:38.

Kubo, M., Yamada, T., Ichikawa, T., et al., 2016. An extremely dense group of massive galaxies at the centre of the protocluster at z = 3.09 in the SSA22 field. *MNRAS*, 455:3333.

Kuiper, E., Hatch, N.A., Röttgering, H.J.A., et al., 2010. A galaxy populations study of a radio-selected protocluster at z ˜ 3.1. *MNRAS*, 405:969.

Kurk, J.D., Röttgering, H.J.A., Pentericci, L., et al., 2000. A Search for clusters at high redshift. I. Candidate Lyalpha emitters near 1138-262 at z=2.2. *A&A*, 358:L1.

Laporte, N., Ellis, R.S., Boone, F., et al., 2017. Dust in the Reionization Era: ALMA Observations of a z=8.38 Gravitationally Lensed Galaxy. *ApJ*, 837:L21.

Larson, R.B., Tinsley, B.M., and Caldwell, C.N., 1980. The evolution of disk galaxies and the origin of S0 galaxies. *ApJ*, 237:692.

Lawrence, A., Warren, S.J., Almaini, O., et al., 2007. The UKIRT Infrared Deep Sky Survey (UKIDSS). *MNRAS*, 379:1599.

Le Fevre, O., Deltorn, J.M., Crampton, D., et al., 1996. Clustering around the Radio Galaxy MRC 0316-257 at Z = 3.14. *ApJ*, 471:L11.

Leger, A. and Puget, J.L., 1984. Identification of the 'unidentified' IR emission features of interstellar dust? *A&A*, 137:L5.

Lehmer, B.D., Alexander, D.M., Geach, J.E., et al., 2009. The Chandra Deep Protocluster Survey: Evidence for an Enhancement of AGN Activity in the SSA22 Protocluster at z = 3.09. *ApJ*, 691:687.

Lemaux, B.C., Cucciati, O., Tasca, L.A.M., et al., 2014. VIMOS Ultra-Deep Survey (VUDS): Witnessing the assembly of a massive cluster at z ˜ 3.3. *A&A*, 572:A41.

Liddle, A.R. and Lyth, D.H., 1993. The cold dark matter density perturbation. *Physics Reports*, 231:1.

Lilly, S.J., 1988. Discovery of a radio galaxy at a redshift of 3.395. *ApJ*, 333:161.

Lofthouse, E.K., Kaviraj, S., Conselice, C.J., et al., 2017. Major mergers are not significant drivers of star formation or morphological transformation around the epoch of peak cosmic star formation. *MNRAS*, 465:2895.

Lotz, J.M., Jonsson, P., Cox, T.J., et al., 2008. Galaxy merger morphologies and time-scales from simulations of equal-mass gas-rich disc mergers. *MNRAS*, 391:1137.

Lotz, J.M., Jonsson, P., Cox, T.J., et al., 2011. The Major and Minor Galaxy Merger Rates at z ¡ 1.5. *ApJ*, 742:103.

Lotz, J.M., Papovich, C., Faber, S.M., et al., 2013. Caught in the Act: The Assembly of Massive Cluster Galaxies at z = 1.62. *ApJ*, 773:154.

Lukić, Z., Heitmann, K., Habib, S., et al., 2007. The Halo Mass Function: High-Redshift Evolution and Universality. *ApJ*, 671:1160.

Lutz, D., Dunlop, J.S., Almaini, O., et al., 2001. The extended counterpart of submm source Lockman 850.1. *A&A*, 378:70.

Madau, P., 1995. Radiative transfer in a clumpy universe: The colors of high-redshift galaxies. *ApJ*, 441:18.

Madau, P. and Dickinson, M., 2014. Cosmic Star-Formation History. *Annual Review of Astronomy and Astrophysics*, 52:415.

Madau, P., Pozzetti, L., and Dickinson, M., 1998. The Star Formation History of Field Galaxies. *ApJ*, 498:106.

Magdis, G.E., Elbaz, D., Daddi, E., et al., 2010a. A Multi-wavelength View of the Star Formation Activity at $z \sim 3$. *ApJ*, 714:1740.

Magdis, G.E., Rigopoulou, D., Huang, J.S., et al., 2010b. On the stellar masses of IRAC detected Lyman Break Galaxies at $z \sim 3$. *MNRAS*, 401:1521.

Magnelli, B., Elbaz, D., Chary, R.R., et al., 2009. The $0.4 < z < 1.3$ star formation history of the Universe as viewed in the far-infrared. *A&A*, 496:57.

Magnelli, B., Elbaz, D., Chary, R.R., et al., 2011. Evolution of the dusty infrared luminosity function from $z = 0$ to $z = 2.3$ using observations from Spitzer. *A&A*, 528:A35.

Magnelli, B., Lutz, D., Santini, P., et al., 2012. A Herschel view of the far-infrared properties of submillimetre galaxies. *A&A*, 539:A155.

Magnelli, B., Popesso, P., Berta, S., et al., 2013. The deepest Herschel-PACS far-infrared survey: number counts and infrared luminosity functions from combined PEP/GOODS-H observations. *A&A*, 553:A132.

Man, A.W.S., Toft, S., Zirm, A.W., et al., 2012. The Pair Fraction of Massive Galaxies at $0 \leq z \leq 3$. *ApJ*, 744:85.

Man, A.W.S., Zirm, A.W., and Toft, S., 2016. Resolving the Discrepancy of Galaxy Merger Fraction Measurements at z $\sim$ 0-3. *ApJ*, 830:89.

Mannucci, F., Cresci, G., Maiolino, R., et al., 2009. LSD: Lyman-break galaxies Stellar populations and Dynamics - I. Mass, metallicity and gas at $z \sim$3.1. *MNRAS*, 398:1915.

Maraston, C., 1998. Evolutionary synthesis of stellar populations: a modular tool. *MNRAS*, 300:872.

Maraston, C., 2005. Evolutionary population synthesis: models, analysis of the ingredients and application to high-z galaxies. *MNRAS*, 362:799.

Maraston, C., Daddi, E., Renzini, A., et al., 2006. Evidence for TP-AGB Stars in High-Redshift Galaxies, and Their Effect on Deriving Stellar Population Parameters. *ApJ*, 652:85.

Marconi, A. and Hunt, L.K., 2003. The Relation between Black Hole Mass, Bulge Mass, and Near-Infrared Luminosity. *ApJ*, 589:L21.

Martin, D.C., Chang, D., Matuszewski, M., et al., 2014. Intergalactic Medium Emission Observations with the Cosmic Web Imager. I. The Circum-QSO Medium of QSO 1549+19, and Evidence for a Filamentary Gas Inflow. *ApJ*, 786:106.

Martin, D.C., Wyder, T.K., Schiminovich, D., et al., 2007. The UV-Optical Galaxy Color-Magnitude Diagram. III. Constraints on Evolution from the Blue to the Red Sequence. *ApJ*, 173:342.

Martinovic, N., 2015. Halo Statistics Analysis Within Medium Volume Cosmological N-Body Simulation. *Serbian Astronomical Journal*, 190:11.

Massa, D. and Savage, B., 1989. Measurements of Interstellar Extinction. In L.J. Allamandola and A.G.G.M. Tielens, editors, *Interstellar Dust*, volume 135 of *IAU Symposium*, page 3.

Matsuda, Y., Iono, D., Ohta, K., et al., 2007. High-Resolution Submillimeter Imaging of the Lyα Blob 1 in SSA 22. *ApJ*, 667:667.

Matsuda, Y., Nakamura, Y., Morimoto, N., et al., 2009. Lyα blobs like company: the discovery of a candidate 100kpc Lyα blob near to a radio galaxy with a giant Lyα halo B3J2330+3927 at z = 3.1. *MNRAS*, 400:L66.

Matsuda, Y., Richard, J., Smail, I., et al., 2010. A search for galaxies in and around an HI overdense region at z = 5. *MNRAS*, 403:L54.

Matsuda, Y., Tamura, T.Y.H., Yamauchi, R., et al., 2005. Large-scale filamentary structure around the protocluster at redshift z = 3.1. *AJ*, 634:L125 .

Matsuda, Y., Yamada, T., Hayashino, T., et al., 2004. A Subaru Search for Lyα Blobs in and around the Protocluster Region At Redshift z = 3.1. *AJ*, 128:569.

Matsuda, Y., Yamada, T., Hayashino, T., et al., 2011. The Subaru Lyα blob survey: a sample of 100-kpc Lyα blobs at z=3. *MNRAS*, 410:L13.

McCarthy, P.J., 1993. High redshift radio galaxies. *Annual Review of Astronomy and Astrophysics*, 31:639.

McCarthy, P.J., Le Borgne, D., Crampton, D., et al., 2004. Evolved Galaxies at z>1.5 from the Gemini Deep Deep Survey: The Formation Epoch of Massive Stellar Systems. *ApJ*, 614:L9.

McConnell, N.J. and Ma, C.P., 2013. Revisiting the Scaling Relations of Black Hole Masses and Host Galaxy Properties. *ApJ*, 764:184.

McLure, R.J., Dunlop, J.S., Bowler, R.A.A., et al., 2013. A new multifield determination of the galaxy luminosity function at z = 7-9 incorporating the 2012 Hubble Ultra-Deep Field imaging. *MNRAS*, 432:2696.

Merlin, E., Fontana, A., Ferguson, H.C., et al., 2015. T-PHOT: A new code for PSF-matched, prior-based, multiwavelength extragalactic deconfusion photometry. *A&A*, 582:A15.

Meurer, G.R., Heckman, T.M., and Calzetti, D., 1999. Dust Absorption and the Ultraviolet Luminosity Density at z ˜ 3 as Calibrated by Local Starburst Galaxies. *ApJ*, 521:64.

Michałowski, M.J., Dunlop, J.S., Cirasuolo, M., et al., 2012a. The stellar masses and specific star-formation rates of submillimetre galaxies. *A&A*, 541:A85.

Michałowski, M.J., Dunlop, J.S., Ivison, R.J., et al., 2012b. AzTEC half square degree survey of the SHADES fields - II. Identifications, redshifts and evidence for large-scale structure. *MNRAS*, 426:1845.

Mo, H.J. and White, S.D.M., 2002. The abundance and clustering of dark haloes in the standard ΛCDM cosmogony. *MNRAS*, 336:112.

Mori, M. and Umemura, M., 2006. The evolution of galaxies from primeval irregulars to present-day ellipticals. *Nature*, 440:644.

Mori, M., Umemura, M., and Ferrara, A., 2004. The Nature of Lyα Blobs: Supernova-dominated Primordial Galaxies. *ApJ*, 613:L97.

Muldrew, S.I., Hatch, N.A., and Cooke, E.A., 2015. What are protoclusters? - Defining high-redshift galaxy clusters and protoclusters. *MNRAS*, 452:2528.

Murphy, E.J., Condon, J.J., Schinnerer, E., et al., 2011. Calibrating Extinction-free Star Formation Rate Diagnostics with 33 GHz Free-free Emission in NGC 6946. *ApJ*, 737:67.

Nagamine, K., Fukugita, M., Cen, R., et al., 2001. Star Formation History and Stellar Metallicity Distribution in a Cold Dark Matter Universe. *ApJ*, 558:497.

Navarro, J.F., Frenk, C.S., and White, S.D.M., 1997. A Universal Density Profile from Hierarchical Clustering. *ApJ*, 490:493.

Nelson, D., Genel, S., Vogelsberger, M., et al., 2015. The impact of feedback on cosmological gas accretion. *MNRAS*, 448:59.

Nelson, D., Vogelsberger, M., Genel, S., et al., 2013. Moving mesh cosmology: tracing cosmological gas accretion. *MNRAS*, 429:3353.

Nesvadba, N.P.H., Lehnert, M.D., Davies, R.I., et al., 2008. Integral-field spectroscopy of a Lyman-break galaxy at z = 3.2: evidence for merging. *A&A*, 479:67.

Neufeld, D.A., 1990. The transfer of resonance-line radiation in static astrophysical media. *ApJ*, 350:216.

Nilsson, K.K., Fynbo, J.P.U., Møller, P., et al., 2006. A Lyman-α blob in the GOODS South field: evidence for cold accretion onto a dark matter halo. *Astronomy and Astrophysics*, 452:L23.

Nilsson, K.K., Møller, P., Möller, O., et al., 2007. A multi-wavelength study of z = 3.15 Lyman-α emitters in the GOODS South Field. *A&A*, 471:71.

Noeske, K.G., Weiner, B.J., Faber, S.M., et al., 2007. Star Formation in AEGIS Field Galaxies since z=1.1: The Dominance of Gradually Declining Star Formation, and the Main Sequence of Star-forming Galaxies. *ApJ*, 660:L43.

Noll, S., Burgarella, D., Giovannoli, E., et al., 2009. Analysis of galaxy spectral energy distributions from far-UV to far-IR with CIGALE: studying a SINGS test sample. *A&A*, 507:1793.

Norris, M.A., Van de Ven, G., Schinnerer, E., et al., 2016. Being WISE II: Reducing the Influence of Star formation History on the Mass-to-Light Ratio of Quiescent Galaxies. *ApJ*, 832:198.

Oesch, P.A., Bouwens, R.J., Illingworth, G.D., et al., 2013. Probing the Dawn of Galaxies at z ˜ 9-12: New Constraints from HUDF12/XDF and CANDELS data. *ApJ*, 773:75.

Oke, J.B., Cohen, J.G., Carr, M., et al., 1995. The Keck Low-Resolution Imaging Spectrometer. *PASP*, 107:375.

Oteo, I., Sobral, D., Ivison, R.J., et al., 2015. On the nature of Hα emitters at z $\sim$ 2 from the HiZELS survey: physical properties, Lyα escape fraction and main sequence. *MNRAS*, 452:2018.

Ouchi, M., Shimasaku, K., Akiyama, M., et al., 2005. The Discovery of Primeval Large-Scale Structures with Forming Clusters at Redshift 6. *ApJ*, 620:L1.

Ouchi, M., Shimasaku, K., Akiyama, M., et al., 2008. The Subaru/XMM-Newton Deep Survey (SXDS). IV. Evolution of Lyα Emitters from z = 3.1 to 5.7 in the 1 deg^2 Field: Luminosity Functions and AGN. *ApJ*, 176:301-330.

Overzier, R.A., 2016. The realm of the galaxy protoclusters. A review. *The Astronomy and Astrophysics Review*, 24:14.

Overzier, R.A., Bouwens, R.J., Cross, N.J.G., et al., 2008. Lyman Break Galaxies, Lyα Emitters, and a Radio Galaxy in a Protocluster at z = 4.1. *ApJ*, 673:143-162.

Overzier, R.A., Shu, X., Zheng, W., et al., 2009. Stellar Masses of Lyman Break Galaxies, Lyα Emitters, and Radio Galaxies in Overdense Regions at z = 4-6. *ApJ*, 704:548.

Papovich, C., Dickinson, M., and Feruson, H.C., 2001. The Stellar Populations and Evolution of Lyman Break Galaxies. *ApJ*, 559:620.

Peebles, P.J.E., 1968. Recombination of the Primeval Plasma. *ApJ*, 153:1.

Peebles, P.J.E., 1982. Large-scale background temperature and mass fluctuations due to scale-invariant primeval perturbations. *ApJ*, 263:L1.

Peebles, P.J.E. and Yu, J.T., 1970. Primeval Adiabatic Perturbation in an Expanding Universe. *ApJ*, 162:815.

Penzias, A.A. and Wilson, R.W., 1965. A Measurement of Excess Antenna Temperature at 4080 Mc/s. *ApJ*, 142:419.

Pettini, M., Rix, S.A., Steidel, C.C., et al., 2002. New Observations of the Interstellar Medium in the Lyman Break Galaxy MS 1512-cB58. *ApJ*, 569:742.

Pettini, M., Shapley, A.E., Steidel, C.C., et al., 2001. The Rest-Frame Optical Spectra of Lyman Break Galaxies: Star Formation, Extinction, Abundances, and Kinematics. *ApJ*, 554:981.

Pirzkal, N., Malhotra, S., Rhoads, J.E., et al., 2006. Lyman-alpha Emitters in the HUDF: A Population of Low Mass, Star Forming Galaxies. In *American Astronomical Society Meeting Abstracts*, volume 38 of *Bulletin of the American Astronomical Society*, page 1145.

Planck Collaboration, Adam, R., Ade, P.A.R., et al., 2016a. Planck 2015 results. I. Overview of products and scientific results. *A&A*, 594:A1.

Planck Collaboration, Ade, P.A.R., Aghanim, N., et al., 2016b. Planck 2015 results. XIII. Cosmological parameters. *A&A*, 594:A13.

Pope, A., Scott, D., Dickinson, M., et al., 2006. The Hubble Deep Field-North SCUBA Super-map - IV. Characterizing submillimetre galaxies using deep Spitzer imaging. *MNRAS*, 370:1185.

Prescott, M.K.M., Momcheva, I., Brammer, G.B., et al., 2015. Overturning the Case for Gravitational Powering in the Prototypical Cooling Lyα Nebula. *ApJ*, 802:32.

Primack, J.R. and Blumenthal, G.R., 1984. What is the dark matter? - Implications for galaxy formation and particle physics. In J. Audouze and J. Tran Thanh Van, editors, *NATO Advanced Science Institutes (ASI) Series C*, volume 117 of *NATO Advanced Science Institutes (ASI) Series C*, pages 163–183.

Quilis, V., Moore, B., and Bower, R., 2000. Gone with the Wind: The Origin of S0 Galaxies in Clusters. *Science*, 288:1617.

Rauch, M., Becker, G.D., Haehnelt, M.G., et al., 2011. Filamentary infall of cold gas and escape of Lyα and hydrogen ionizing radiation from an interacting high-redshift galaxy. *MNRAS*, 418:1115.

Rawlings, S., Lacy, M., Blundell, K.M., et al., 1996. A radio galaxy at redshift 4.41. *Nature*, 383:502.

Reddy, N.A. and Steidel, C.C., 2009. A Steep Faint-End Slope of the UV Luminosity Function at z ˜ 2-3: Implications for the Global Stellar Mass Density and Star Formation in Low-Mass Halos. *ApJ*, 692:778.

Renaud, F., Bournaud, F., Kraljic, K., et al., 2014. Starbursts triggered by intergalactic tides andinterstellar compressive turbulence. *MNRAS*, 442:L33.

Rigopoulou, D., Huang, J.S., Papovich, C., et al., 2006. Spitzer Observations of z ˜ 3 Lyman Break Galaxies: Stellar Masses and Mid-Infrared Properties. *ApJ*, 648:81.

Roberts, M.S., 1963. The Content of Galaxies: Stars and Gas. *Annual Review of Astronomy and Astrophysics*, 1:149.

Rodighiero, G., Daddi, E., Baronchelli, I., et al., 2011. The Lesser Role of Starbursts in Star Formation at z = 2. *ApJ*, 739:L40.

Romeo, A.B. and Fathi, K., 2016. What powers the starburst activity of NGC 1068? Star-driven gravitational instabilities caught in the act. *MNRAS*, 460:2360.

Rosdahl, J. and Blaizot, J., 2012. Extended Lyα emission from cold accretion streams. *MNRAS*, 423:344.

Salim, S., Rich, R.M., Charlot, S., et al., 2007. UV Star Formation Rates in the Local Universe. *ApJ*, 173:267.

Salimbeni, S., Fontana, A., Giallongo, E., et al., 2009. Uncertainties and Systematic Effects on the estimate of stellar masses in high z galaxies. In G. Giobbi, A. Tornambe, G. Raimondo, M. Limongi, L.A. Antonelli, N. Menci, and E. Brocato, editors, *American Institute of Physics Conference Series*, volume 1111 of *American Institute of Physics Conference Series*, pages 207–211.

Salpeter, E.E., 1955. The Luminosity Function and Stellar Evolution. *ApJ*, 121:161.

Sanders, D.B. and Mirabel, I.F., 1996. Luminous Infrared Galaxies. *Annual Review of Astronomy and Astrophysics*, 34:749.

Sargent, M.T., Béthermin, M., Daddi, E., et al., 2012. The Contribution of Starbursts and Normal Galaxies to Infrared Luminosity Functions at z $<$ 2. *ApJ*, 747:L31.

Saro, A., Borgani, S., Tornatore, L., et al., 2009. Simulating the formation of a protocluster at $z \sim 2$. *MNRAS*, 392:795.

Sawicki, M. and Yee, H.K.C., 1998. Optical-Infrared Spectral Energy Distributions of Z ¿ 2 Lyman Break Galaxies. *AJ*, 115:1329.

Schawinski, K., Urry, C.M., Simmons, B.D., et al., 2014. The green valley is a red herring: Galaxy Zoo reveals two evolutionary pathways towards quenching of star formation in early- and late-type galaxies. *MNRAS*, 440:889.

Schaye, J., Crain, R.A., Bower, R.G., et al., 2015. The EAGLE project: simulating the evolution and assembly of galaxies and their environments. *MNRAS*, 446:521.

Schiminovich, D., Ilbert, O., Arnouts, S., et al., 2005. The GALEX-VVDS Measurement of the Evolution of the Far-Ultraviolet Luminosity Density and the Cosmic Star Formation Rate. *ApJ*, 619:L47.

Shapley, A.E., Erb, D.K., Pettini, M., et al., 2004. Evidence for Solar Metallicities in Massive Star-forming Galaxies at z ¿ 2. *ApJ*, 612:108.

Shapley, A.E., Steidel, C.C., Adelberger, K.L., et al., 2001. The Rest-Frame Optical Properties of z˜=3 Galaxies. *ApJ*, 562:95.

Shapley, A.E., Steidel, C.C., Erb, D.K., et al., 2005. Ultraviolet to Mid-Infrared Observations of Star-forming Galaxies at z˜2: Stellar Masses and Stellar Populations. *ApJ*, 626:698.

Shapley, A.E., Steidel, C.C., Pettini, M., et al., 2003. Rest-Frame Ultraviolet Spectra of z˜3 Lyman Break Galaxies. *ApJ*, 588:65.

Siebenmorgen, R. and Krügel, E., 2007. Dust in starburst nuclei and ULIRGs. SED models for observers. *A&A*, 461:445.

Skelton, R.E., Whitaker, K.E., Momcheva, I.G., et al., 2014. 3D-HST WFC3-selected Photometric Catalogs in the Five CANDELS/3D-HST Fields: Photometry, Photometric Redshifts, and Stellar Masses. *ApJ*, 214:24.

Smail, I., Edge, A.C., Ellis, R.S., et al., 1998. A statistical analysis of the galaxy populations of distant luminous X-ray clusters. *MNRAS*, 293:124.

Smail, I., Ivison, R.J., and Blain, A.W., 1997. A Deep Sub-millimeter Survey of Lensing Clusters: A New Window on Galaxy Formation and Evolution. *ApJ*, 490:L5.

Smethurst, R.J., Lintott, C.J., Simmons, B.D., et al., 2015. Galaxy Zoo: evidence for diverse star formation histories through the green valley. *MNRAS*, 450:435.

Smith, D.J.B. and Jarvis, M.J., 2007. Evidence for cold accretion onto a massive galaxy at high redshift? *MNRAS*, 378:L49.

Smith, D.J.B., Jarvis, M.J., Lacy, M., et al., 2008. Infrared and millimetre-wavelength evidence for cold accretion within a z = 2.83 Lyman α blob. *MNRAS*, 389:799.

Springel, V., Matteo, T.D., and Hernquist, L., 2005. Modelling feedback from stars and black holes in galaxy mergers. *MNRAS*, 361:776 .

Springel, V., White, S.D.M., Jenkins, A., et al., 2005. Simulations of the formation, evolution and clustering of galaxies and quasars. *Nature*, 435:629.

Stark, D.P., Ellis, R.S., Bunker, A., et al., 2009. The Evolutionary History of Lyman Break Galaxies Between Redshift 4 and 6: Observing Successive Generations of Massive Galaxies in Formation. *ApJ*, 697:1493.

Stark, D.P., Schenker, M.A., Ellis, R., et al., 2013. Keck Spectroscopy of $3 < z < 7$ Faint Lyman Break Galaxies: The Importance of Nebular Emission in Understanding the Specific Star Formation Rate and Stellar Mass Density. *ApJ*, 763:129.

Steidel, C.C., Adelberger, K.L., Dickinson, M., et al., 1998. A large structure of galaxies at redshift z$\sim$3 and its cosmological implications. *ApJ*, 492:428.

Steidel, C.C., Adelberger, K.L., and Shapley, A.E., 2000. Lα imaging of a proto-cluster region at $< z >= 3.09$. *ApJ*, 532:170.

Steidel, C.C., Adelberger, K.L., Shapley, A.E., et al., 2003. Lyman Break Galaxies at Redshift $z \sim 3$: Survey Description and Full Data Set. *ApJ*, 592:728.

Steidel, C.C., Adelberger, K.L., Shapley, A.E., et al., 2005. Spectroscopic Identification of a Protocluster at z=2.300: Environmental Dependence of Galaxy Properties at High Redshift. *ApJ*, 626:44.

Steidel, C.C., Bogosavljević, M., Shapley, A.E., et al., 2011. Diffuse Lyα Emitting Halos: A Generic Property of High-redshift Star-forming Galaxies. *ApJ*, 736:160.

Steidel, C.C., Erb, D.K., Shapley, A.E., et al., 2010. The Structure and Kinematics of the Circumgalactic Medium from Far-ultraviolet Spectra of z $\approx$ 2-3 Galaxies. *ApJ*, 717:289.

Steidel, C.C., Giavalisco, M., Pettini, M., et al., 1996. Spectroscopic Confirmation of a Population of Normal Star-forming Galaxies at Redshifts $z \geq 3$. *ApJ*, 462:L17.

Steidel, C.C. and Hamilton, D., 1992. Deep imaging of high redshift QSO fields below the Lyman limit. I - The field of Q0000-263 and galaxies at z = 3.4. *AJ*, 104:941.

Steidel, C.C. and Hamilton, D., 1993. Deep imaging of high redshift QSO fields below the Lyman limit. II - Number counts and colors of field galaxies. *AJ*, 105:2017.

Stern, D., Eisenhardt, P., Gorjian, V., et al., 2005. Mid-Infrared Selection of Active Galaxies. *ApJ*, 631:163.

Stern, D., Holden, B., Stanford, S.A., et al., 2003. Confirmation of a Radio-selected Galaxy Overdensity at z=1.11. *AJ*, 125:2759.

Stott, J.P., Sobral, D., Smail, I., et al., 2013. The merger rates and sizes of galaxies across the peak epoch of star formation from the HiZELS survey. *MNRAS*, 430:1158.

Strateva, I., Ivezić, Ž., Knapp, G.R., et al., 2001. Color Separation of Galaxy Types in the Sloan Digital Sky Survey Imaging Data. *AJ*, 122:1861.

Suwa, T., Habe, A., and Yoshikawa, K., 2006. Protoclusters in the ΛCDM Universe. *ApJ*, 646:L5.

Tamburri, S., Saracco, P., Longhetti, M., et al., 2014. The population of early-type galaxies: how it evolves with time and how it differs from passive and late-type galaxies. *A&A*, 570:A102.

Tamura, Y., Kohno, K., Nakanishi, K., et al., 2009. Spatial correlation between submillimetre and Lyman-α galaxies in the SSA22 protocluster. *Nature*, 459:61.

Tamura, Y., Matsuda, Y., Ikarashi, S., et al., 2013. Obscured star formation in Lyα blobs at z = 3.1. *MNRAS*, 430:2768.

Taniguchi, Y. and Shioya, Y., 2000. Superwind Model of Extended Lyα Emitters at High Redshift. *ApJ*, 532:L13.

Targett, T.A., Dunlop, J.S., Cirasuolo, M., et al., 2013. The properties of (sub-)millimetre-selected galaxies as revealed by CANDELS HST WFC3/IR imaging in GOODS-South. *MNRAS*, 432:2012.

Taylor-Mager, V.A., Conselice, C.J., Windhorst, R.A., et al., 2007. Dependence of Galaxy Structure on Rest-Frame Wavelength and Galaxy Type. *ApJ*, 659:162.

Thilker, D.A., Bianchi, L., Schiminovich, D., et al., 2010. NGC 404: A Rejuvenated Lenticular Galaxy on a Merger-induced, Blueward Excursion Into the Green Valley. *ApJ*, 714:L171.

Tielens, A.G.G.M., 2008. Interstellar Polycyclic Aromatic Hydrocarbon Molecules. *Annual Review of Astronomy and Astrophysics*, 46:289.

Tombesi, F., Mushotzky, R.F., Reynolds, C.S., et al., 2017. Feeding and feedback in the powerful radio galaxy 3C 120. *ArXiv e-prints*.

Tomczak, A.R., Quadri, R.F., Tran, K.V.H., et al., 2014. Galaxy Stellar Mass Functions from ZFOURGE/CANDELS: An Excess of Low-mass Galaxies since z = 2 and the Rapid Buildup of Quiescent Galaxies. *ApJ*, 783:85.

Topping, M.W., Shapley, A.E., and Steidel, C.C., 2016. Substructure within the SSA22 Protocluster at $z \sim$3.09. *ApJ*, 824:L11.

Tormen, G., Bouchet, F.R., and White, S.D.M., 1997. The structure and dynamical evolution of dark matter haloes. *MNRAS*, 286:865.

Trainor, R.F., Steidel, C.C., Strom, A.L., et al., 2015. The Spectroscopic Properties of Lyα-Emitters at $z \sim 2.7$: Escaping Gas and Photons from Faint Galaxies. *ArXiv e-prints*.

Uchimoto, Y.K., Suzuki, R., Tokoku, C., et al., 2008. Subaru/MOIRCS Near-Infrared Imaging in the Proto-Cluster Region at $z = 3.1$. *PASJ*, 60:683.

Uchimoto, Y.K., Yamada, T., Kajisawa, M., et al., 2012. Assembly of Massive Galaxies in a High-z Protocluster. *ApJ*, 750:116.

Umehata, H., Tamura, Y., Kohno, K., et al., 2014. AzTEC/ASTE 1.1-mm survey of SSA22: Counterpart identification and photometric redshift survey of submillimetre galaxies. *MNRAS*, 440:3462.

Umehata, H., Tamura, Y., Kohno, K., et al., 2015. ALMA Deep Field in SSA22: A Concentration of Dusty Starbursts in a z = 3.09 Protocluster Core. *ApJ*, 815:L8.

Umehata, H., Tamura, Y., Kohno, K., et al., 2017. ALMA Deep Field in SSA22: Source Catalog and Number Counts. *ApJ*, 835:98.

Valencic, L.A., Clayton, G.C., and Gordon, K.D., 2004. Ultraviolet Extinction Properties in the Milky Way. *ApJ*, 616:912.

van Breugel, W., De Breuck, C., Stanford, S.A., et al., 1999. A Radio Galaxy at z = 5.19. *ApJ*, 518:L61.

van de Voort, F. and Schaye, J., 2012. Properties of gas in and around galaxy haloes. *MNRAS*, 423:2991.

van de Voort, F., Schaye, J., Booth, C.M., et al., 2011. The rates and modes of gas accretion on to galaxies and their gaseous haloes. *MNRAS*, 414:2458.

van Dokkum, P.G., 2005. The Recent and Continuing Assembly of Field Elliptical Galaxies by Red Mergers. *AJ*, 130:2647.

van Dokkum, P.G., Förster Schreiber, N.M., Franx, M., et al., 2003. Spectroscopic Confirmation of a Substantial Population of Luminous Red Galaxies at Redshifts z>2. *ApJ*, 587:L83.

Venemans, B.P., Kurk, J.D., Miley, G.K., et al., 2002. The Most Distant Structure of Galaxies Known: A Protocluster at z=4.1. *ApJ*, 569:L11.

Venemans, B.P., Kurk, J.D., Miley, G.K., et al., 2003. Large scale structures around high redshift radio galaxies. *New Astronomy Reviews*, 47:353.

Venemans, B.P., Röttgering, H.J.A., Miley, G.K., et al., 2005. Properties of Lyα emitters around the radio galaxy MRC 0316 257. *A&A*, 431:793.

Venemans, B.P., Röttgering, H.J.A., Miley, G.K., et al., 2007. Protoclusters associated with z $<$ 2 radio galaxies . I. Characteristics of high redshift protoclusters. *A&A*, 461:823.

Venemans, B.P., Röttgering, H.J.A., Overzier, R.A., et al., 2004. Discovery of six Lyα emitters near a radio galaxy at z$\sim$5.2. *A&A*, 424:L17.

Wang, W.H., Cowie, L.L., Barger, A.J., et al., 2011. SMA Observations of GOODS 850-11 and GOODS 850-13: First Examples of Multiple Submillimeter Sources Resolved by an Interferometer. *ApJ*, 726:L18.

Wardlow, J.L., Malhotra, S., Zheng, Z., et al., 2014. Constraining the Lyα Escape Fraction with Far-infrared Observations of Lyα Emitters. *ApJ*, 787:9.

Webb, T.M.A., Yamada, T., Huang, J.S., et al., 2009. Spitzer Observations of Extended Lyman-α Clouds in the SSA22 Field. *ApJ*, 692:1561.

White, S.D.M. and Frenk, C.S., 1991. Galaxy formation through hierarchical clustering. *ApJ*, 379:52.

White, S.D.M., Frenk, C.S., Davis, M., et al., 1987. Clusters, filaments, and voids in a universe dominated by cold dark matter. *ApJ*, 313:505.

White, S.D.M. and Rees, M.J., 1978. Core condensation in heavy halos - A two-stage theory for galaxy formation and clustering. *MNRAS*, 183:341.

Wilman, R.J., Gerssen, J., Bower, R.G., et al., 2005. The discovery of a galaxy-wide superwind from a young massive galaxy at redshift z ˜ 3. *Nature*, 436:227.

Y., M., Yamada, T., Hayashino, T., et al., 2004. Large-scale structure of emission-line galaxies at z = 3.1. *AJ*, 128:2073.

Yamada, T., Nakamura, Y., Matsuda, Y., et al., 2012. Panoramic Survey of Lyα Emitters at z = 3.1. *AJ*, 143:79.

Yang, Y., Zabludoff, A., Tremonti, C., et al., 2009. Extended Ly *alpha* Nebulae at z $\sim$ 2.3: An Extremely Rare and Strongly Clustered Population? *ApJ*, 693:1579.

Zhao, D., Conselice, C.J., Aragón-Salamanca, A., et al., 2017. Exploring the progenitors of brightest cluster galaxies at z $\sim$ 2. *MNRAS*, 464:1393.

Zheng, W., Postman, M., Zitrin, A., et al., 2012. A magnified young galaxy from about 500 million years after the Big Bang. *Nature*, 489:406.

Zheng, Z., Cen, R., Trac, H., et al., 2010. Radiative Transfer Modeling of Lyα Emitters. I. Statistics of Spectra and Luminosity. *ApJ*, 716:574.

Zheng, Z., Cen, R., Weinberg, D., et al., 2011. Extended Lyα Emission around Star-forming Galaxies. *ApJ*, 739:62.

Zibetti, S., Charlot, S., and Rix, H.W., 2009. Resolved stellar mass maps of galaxies - I. Method and implications for global mass estimates. *MNRAS*, 400:1181.

Zirm, A.W., Stanford, S.A., Postman, M., et al., 2008. The Nascent Red Sequence at z ˜ 2. *ApJ*, 680:224-231.